Power Balance in a Helicon Plasma Source for Space Propulsion

by

Daniel B. White Jr.

B.S. Electrical Engineering (2004)
Texas A&M University, College Station, TX

Submitted to the Department of Aeronautics and Astronautics
in partial fulfillment of the requirements for the degree of

MASTER OF SCIENCE IN AERONAUTICS AND ASTRONAUTICS

at the

MASSACHUSETTS INSTITUTE OF TECHNOLOGY
[June 2008]
May 2008

Author .....
Department of Aeronautics and Astronautics
May, 2008

Certified by .....
Manuel Martinez-Sanchez
Professor of Aeronautics and Astronautics
Thesis Supervisor

Certified by .....
Oleg V. Batishchev
Principal Research Scientist, Department of Aeronautics and Astronautics
Thesis Supervisor

Accepted by .....
Prof. David L. Darmofal
Associate Department Head
Chair, Committee on Graduate Students

Power Balance in a Helicon Plasma Source for Space Propulsion

by

Daniel B. White Jr.

Submitted to the Department of Aeronautics and Astronautics
on May 23, 2008, in partial fulfillment of the
requirements for the degree of
MASTER OF SCIENCE IN AERONAUTICS AND ASTRONAUTICS

Abstract

Electric propulsion systems provide an attractive option for various spacecraft propulsion applications due to their high specific impulse. The power balance of an electric thruster based on a helicon plasma source is presented. The power balance is shown to be comprised of several variables, including the RF power supplied to the system, dissipative losses in transmission hardware, losses in the neutral confinement tube, uncoupled RF radiation, ionization power, and plume output power.

A thermal model for the neutral confinement tube is presented whereby heat flux may be derived from thermal response data. Numerical simulation and experimental benchmarking are employed to validate this thermal model.

A mapping of power consumption is presented. Comparison with experimental parameters indicates that 97% of the power supplied to the system is accounted for, suggesting that primary loss mechanisms have been identified. Avenues for improving the performance of the thruster, based on these data, are presented.

Thesis Supervisor: Manuel Martinez-Sanchez
Title: Professor of Aeronautics and Astronautics

Acknowledgements

The author would like to thank Professor Manuel Martinez-Sanchez for his guidance, valuable insights, and encouragement, both in this work and apart from it. The author is also grateful to Dr. Oleg Batishchev for his leadership on this project. Finally, the author would like to thank Dr. Arthur Gelb for his generous financial support during this study. This work was supported by MIT-AFRL/ERC/Edwards Contract # RS060213 "Experimental Study of the Mini-Helicon Thruster."

Contents

List of Figures

List of Tables

Chapter 1

Introduction

The helicon plasma source has several advantages over competing technologies for producing high density, accelerated plasma flows suitable for application to spacecraft propulsion. The power balance associated with the mini-Helicon Thruster Experiment (mHTX) at MIT is evaluated herein, with the goal of evaluating overall thrust efficiency and mapping avenues for improving performance.

1.1 Historical Context

The utility of ionized gases for space propulsion has been recognized since the time of Tsiolkovsky [1]. Robert H. Goddard informally outlined many of the principles and physical concepts in the 1900s [2]. In the late 1920s, Oberth, building on these principles, included a section about electric propulsion in his classic book *Wege zur Raumschiffahrt* [3]. The first peer-reviewed study on the viability of electric propulsion (EP) appeared in 1948 [4], following the development of lightweight nuclear power systems. In the United States, Ernst Stulinger did much to develop the field of electric propulsion during the 1950s [5-7].

The first successful spaceflight of an electric thruster occurred in July 1964, when the SERT I gridded ion engine completed a pre-programmed thrust profile during a 25 minute suborbital flight [8]. In 1998, Deep Space 1 (DS1) was the first spacecraft to use an electric thruster for primary propulsion [9]. The DS1, Hayabusa [10], Smart 1 [11], and Dawn [12] spacecraft all illustrate the utility of electric propulsion for high-energy missions that might not otherwise be possible using more conventional chemical propulsion. Table 1-1 lists the required velocity increments for typical space missions.

Mission	Delta-V [km/s]
Earth Surface to LEO	~9.3
Earth Surface to C3	11.2
LEO to GEO	4.2
LEO to C3	3.2
LEO to LLO	3.9
LEO to Mercury Orbit & Return	31.0
LEO to Venus Orbit & Return	16.0
LEO to Mars Orbit	5.7
LEO to Mars Orbit & Return	14.0
LEO to Mars Surface and Return	34.0
LEO to Jupiter Orbit and Return	64.0
LEO to Saturn Orbit and Return	110.0
LEO to Solar Escape	8.7
LEO to 1000 AU (50 yr)	142.0
LEO to Alpha Centauri (50 yr)	~30,000

Table 1-1: Typical velocity increments for interplanetary and interstellar missions [13-14].

The strength of electric propulsion lies in its very high specific impulse relative to chemical solutions. Table 1-2 compares the specific impulses of various chemical propellants. Table 1-3 gives typical operational characteristics for several electric propulsion systems.

Oxidizer	Fuel	I_{SP} (SL)	I_{SP} (Vac)
LOX	H_2	389.4	455.3
	H_2-Be (49/51)	459.0	540.0
	CH_4	309.6	368.9
	C_2H_6	306.7	365.7
	C_2H_4	311.5	370.9
	RP-1	300.1	358.2
	N_2H_4	312.8	353.1
	B_5H_9	318.8	383.5
	B_2H_6	341.9	409.8
	CH_4 - H_2 (92.6/7/4)	319.0	379.5
GOX	GH2	407.9	457.7
F_2	H_2	411.8	479.3
	H_2-Li (65.2/34.8)	434.3	515.3
	CH_4	348.4	415.8
	C_2H_6	340.3	406.8
	MMH	348.3	415.4
	N_2H_4	365.3	430.1
	NH_3	360.3	422.8
	B_5H_9	357.3	427.7
OF_2	H_2	409.6	477.4
	CH_4	355.6	421.5
	C_2H_6	358.3	422.1
	RP-1	349.4	410.3
	MMH	349.7	415.0
	N_2H_4	345.0	409.0
	MMH - N_2H_4 - H_2O (50.5/29.8/19.7)	353.3	398.8
	B_2H_6	372.8	445.6
	B_5H_9	361.1	432.5
FLOX (30/70)	H_2	395.0	461.2
FLOX (30/70)	RP-1	316.6	377.2
FLOX (70/30)	RP-1	344.6	403.6
FLOX (87.5/12.2)	MMH	359.7	423.3
N_2F_4	CH_4	319.1	376.7
	C_2H_4	309.7	368.6
	MMH	322.8	380.6
	N_2H_4	335.0	390.5
	NH_3	326.9	379.9
	B_5H_9	332.5	397.8
ClF_5	MMH	302.2	355.9
	N_2H_4	313.2	365.3
	MMH - N_2H_4 (86/14)	303.2	356.9
	MMH - N_2H_4 - $N_2H_5NO_3$ (55/26/19)	305.0	357.1
ClF_3	MMH	284.6	334.1
	N_2H_4	294.4	342.4
N_2O_4	MMH	288.5	341.5
	MMH - Be (76.6/23.4)	316.9	379.6
	MMH - Al (63/37)	295.0	353.1
	N_2H_4	292.0	343.8
	N_2H_4 - UDMH (50/50)	288.9	341.7
	N_2H_4 - Be (80/20)	327.4	392.8
	B_5H_9	298.7	358.5
N_2O_4 - NO (75/25)	MMH	289.7	342.9
	N_2H_4	293.1	345.0
IRFNA (III-A)	UDMH-DETA (60/40)	269.2	318.7
	MMH	274.5	324.3
	UDMH	272.2	322.1
RFNA (IV, HAD)	UDMH-DETA (60/40)	274.4	325.2
	MMH	279.8	330.8
	UDMH	277.4	328.6
H_2O_2	MMH	284.7	336.8
	N_2H_4	286.7	337.6
	N_2H_4 - Be (74.5/25.5)	335.6	403.5
	B_5H_9	307.8	371.6
N_2H_4	B_2H_6	341.0	403.4
	B_5H_9	326.9	389.7

Table 1-2: Theoretical performance of various chemical rocket propellant combinations; P_C = 1000 psia; Expansion to sea level is 14.7 psia. Vacuum expansion implies $A_e/A_t = 40$ (prepared by Rocketdyne Chemical and Material Technology) [15].

Thruster	Power [kW]	I_{SP} [s]	Efficiency	Propellants
Resistojet	0.5 - 1.5	300	80%	N_2H_4, NH_3, Inert Gas, Stable Liquid
Arcjet	0.3 - 100	500 - 1000	30% - 40%	N_2H_4, NH_3, H_2
Gridded Ion Thruster	0.2 - 4	2800	65%	Xe
Hall Effect Thruster	0.3 - 6	1600	50%	Xe
Applied Field MPD	1 - 100	2000 - 5000	50%	NH_3, H_2, Ar
Self Field MPD	200 - 4000	2000 - 5000	30%	NH_3, H_2, Ar
Pulsed Plasma Thruster	0.001 - 0.2	1000	7%	Solid Teflon

Table 1-3: Typical operating features for selected electric thrusters [16].

While electric propulsion certainly provides distinct advantages over traditional chemical schemes for high energy, long-duration space missions, different EP systems themselves have their own sets of advantages and disadvantages. A discussion of the relative merits and drawbacks associated with various systems is given in the sections that follow [13, 16].

Resistojet

The resistojet is certainly the simplest form of electric propulsion available. In a resistojet, electrical energy is simply used to heat a propellant by convection or conduction, which is subsequently exhausted from a conventional rocket nozzle. While this type of thruster is conceptually, operationally, and mechanically quite simple, it is a fundamentally temperature limited device. The very high values of specific impulse that characterize other EP concepts are, therefore, inaccessible to this simple configuration, barring development of advanced higher temperature materials.

Arcjets

A second electrothermal thruster is the arcjet. In this device, high temperature material limitations are circumvented by use of a high-temperature plasma arc to heat propellant gases.

Because of the uneven heating profile associated with this type of machine, typical efficiencies are lower than those available with other devices, which can be seen in Table 1-3. Electrode erosion is a potentially lifetime limiting factor due to the very high temperature of the central arc. Finally, the power processing unit in an arcjet device must provide protection against arc "run away," in which the arc resistance drops and the arc current increases disastrously, vaporizing the electrodes and destroying the device [17].

Gridded Ion Thrusters

Gridded ion thrusters have more in-flight experience for primary propulsion than other EP systems [8,9,10,12]. In a gridded ion system, propellant gas is ionized inside a chamber. A negatively biased grid extracts ions and accelerates them through the grid potential to produce thrust. This ion beam is neutralized by an external cathode, producing quasi-neutral plasma downstream. These systems provide high specific impulse with very high efficiency, as given in Table 1-3. The use of grid arrays with tight dimensional tolerances, however, as well of potentially life-limiting cathodes for beam neutralization, can impact the reliability of these devices.

Hall Effect Thrusters

Hall Effect thrusters have also been used for primary propulsion for spacecraft [11]. These devices offer many of the same advantages as the gridded ion engines discussed above. Notably, they forgo use of material grids for accelerating ions. Hall Effect thrusters use a radial magnetic field near the exit plane of the thruster to confine electrons and promote propellant ionization. As in the gridded ion design, when the positive ions leave the thruster they are neutralized by an

external cathode, yielding a quasi-neutral plume. This external cathode is, again, a potentially lifetime limiting device. Furthermore, the ions in a Hall thruster tend to be hotter than those in gridded machines, resulting in higher plume divergence and in chamber erosion due to ion impingement.

Colloidal Thrusters

A device closely related to the gridded ion thruster is the colloidal thruster. In these devices, propellant droplets with very high mass-per-unit-charge are extracted electrostatically from a propellant dispensing capillary and accelerated through the extraction grid potential to produce thrust. These devices are attractive in that they require no gas phase ionization, and therefore circumvent the accompanying electrical and thermal power losses. Colloidal systems are capable of providing very small thrust levels for very precise maneuvering. However, because of their low thrust per dispenser, colloidal systems require very large arrays to achieve appreciable thrust levels.

Magnetoplasmadynamic (MPD) Thrusters

An MPD is an electromagnetic thruster which uses the Lorentz force to accelerate plasma to provide thrust. In its simplest form, it consists of a coaxial arrangement of an inner cathode and an outer anode. The presence of conducting plasma within the channel establishes a radial current. The azimuthal magnetic field may be applied (applied-field MPD) or, if the radial currents are sufficiently large, self induced (self-field MPD). Because the propellant plasma is quasi-neutral throughout, there is no need for a neutralizing external cathode. These devices are capable of very high power densities and very high thrust density. However, the efficiency is

typically low, as can be seen in Table 1-3, and the very high powers at which these devices optimize (10^6 - 10^7 W) are not readily achievable without nuclear power or perhaps beamed power scenarios. Additionally, the electrodes are a potentially lifetime limiting component, particularly due to anode starvation and the asymmetry of the discharge current.

Pulsed and Unsteady Electromagnetic Concepts

Several concepts exist for unsteady or pulse-mode electromagnetic systems, including the pulsed plasma thruster (PPT) and the pulsed inductive thruster (PIT). Because these devices are inherently unsteady and potentially have very high instantaneous power levels, they are prone to high dissipative losses. In the case of the PIT, the emphasis on very short magnetic rise time tends to drive up the conducting mass of the device, as well as the mass of the power processing unit. PPT devices using solid propellant (usually Teflon) are very simple and robust, in spite of their poor efficiency. The PIT has no electrodes, which are susceptible to erosion, and its average power can be scaled up by increasing the pulse frequency.

1.2 Helicon Plasma Source

In 1970 a simple plasma source was discovered [18] for producing dense plasmas by exciting helicon waves. The utility of this plasma source for space propulsion was not exploited until over thirty years later [19]. Since that time, researchers throughout the world have experimentally verified the viability of the helicon plasma source for spacecraft propulsion.

1.2.1 Source Properties

The helicon plasma source has several advantages as a source of laboratory plasma that may potentially translate into utility as a thruster for space propulsion. First, a helicon plasma source can operate with a wide variety of feed gases. The current experimental configuration has been run using monatomic gases like xenon and argon, as well as molecular gases like nitrogen. Mixed molecular species, such as air, have also been run successfully. This is advantageous for space propulsion because it gives some flexibility in propellant selection.

Next, a helicon plasma source can produce plasmas with very high densities, approaching 10^{20} particles/m^3. For application to spacecraft propulsion, this means that a helicon thruster may achieve very high thrust densities with good volumetric efficiency for the thruster as a whole.

Finally, a helicon is an electrode-less plasma source. This eliminates the risk of contamination of the plume with cathode material, and consequently there is a smaller risk of contamination of the spacecraft by the plume.

1.2.2 Acceleration Mechanism

It is well established that bulk plasma acceleration is accomplished when the helicon wave couples to the electron population, establishing an ambipolar electric field. Ions are in turn accelerated by this electric field, accelerating the plasma bulk. The means by which wave energy is transferred to the electron population with such high efficiency is still an active area of research. It has been shown that in order for purely collisional damping to account for the observed deposition of RF energy, the plasma must have a collision frequency at least 1000 times greater than the theoretical value [20]. A second coupling mechanism that has been suggested is Landau damping [21]. Experiments indicate, however, that there are an insufficient number of phased fast electrons in the helicon discharge for Landau damping to account for the majority of directional coupling [22]. Finally, Trivelpiece-Gould (TG) mode conversion has been suggested as an alternative means of coupling helicon wave energy to the plasma [23]. However, analysis shows that if TG mode conversion is a dominant energy absorption mechanism in the high-B_0 plasma, such mode conversion must be occurring on the outer plasma surface only [24]. This is in contrast to the observed high-temperature core associated with the helicon discharge. A final theory created to explain the efficient absorption of helicon wave energy posits that during operation in the helicon mode, a radial plasma density gradient forms a potential well, trapping the helicon wave, and allowing electromagnetic energy to be absorbed over the course of repeated reflections [25]. This theoretical framework predicts radial variation in the hot electron population density, and data consistent with this prediction have been presented [26].

Despite the lack of a clear, mechanistic understanding of helicon wave damping, the elegance of wave-coupled acceleration of plasma for space propulsion begs its exploitation. The synergistic coupling of the ionization, heating and acceleration mechanism associated uniquely

with the helicon plasma source is advantageous in assuring a robust, reliable solution for future space propulsion applications.

1.3 Helicon Plasma Thruster Design

1.3.1 Evolution of mHTX Design

The antecedents of the mHTX study at MIT lie in earlier experimental work on the first stage of the VASIMR engine [27]. Experimental investigation of the helicon thruster at MIT was begun in January 2004. Since that time, several revisions of the experimental apparatus have been implemented. Most notably, a change in the construction of the helicon antenna from braided shielding to copper tubing has been made, and several revisions in the construction and number of electromagnets have been effected. After preliminary implementation [28], spectrographic emission data were taken for the helicon plasma source operating with argon in the helicon and inductively coupled mode [29]. Concurrently, preliminary work was begun in characterizing the power balance for the helicon plasma source [30]. Most recently, preliminary performance metrics were gathered for the helicon plasma source, operating in its current configuration [31]. A more detailed description of the systems associated with the mHTX is given in the sections that follow.

1.3.2 RF Circuit

Power is transferred from the RF power supply to the impedance matching network over standard RG-218 coaxial cable with a characteristic impedance of 75 Ω. The matching network is used to manually match the dynamic load impedance associated with the helicon discharge. It is comprised of a series and shunt variable capacitor, Z_1 and Z_2, which can be seen in Figure 1-1

below. Test points for measuring voltage and current are implemented with series capacitors, C_1 and C_2, and current sensing transformer, T_1, respectively.

The RF feed through into the vacuum chamber is constructed from ¼ in. copper rod and ¾ in. K-type copper tubing. The feed through is arranged so that the smaller ¼ in. center line fits coaxially inside the larger ¾ in. return line. The complete feed through assembly has a computed mass of approximately 0.75 kg, based on the linear weight of the two materials.

The antenna used in the current configuration is a right-hand polarized, half-helical antenna, which has been shown to preferentially excite the m = +1 mode. Antenna length is one-half the axial wavelength, and is constructed from 1 in. copper tubing.

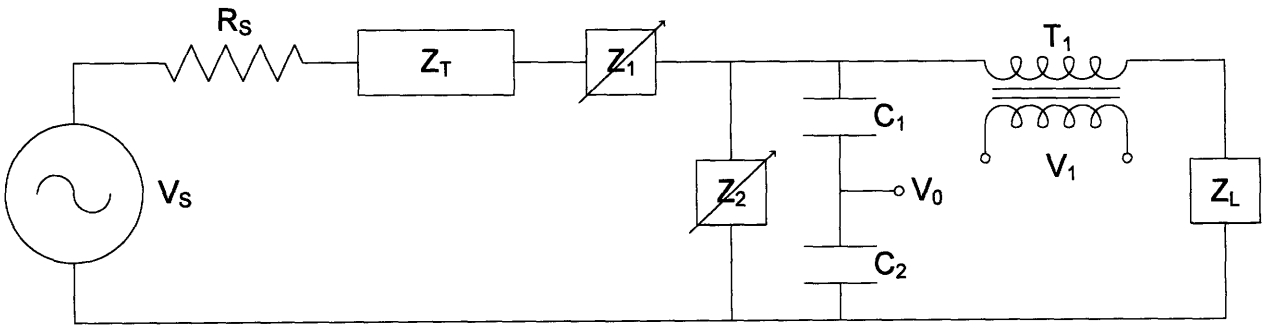

Figure 1-1: RF Circuit for the Helicon Experiment in the MIT SPL. The transmission line is represented with characteristic impedence ZT. The impedance matching network is formed by Z1 & Z2. C1 & C2 form a voltage-sensing network. T1 is used for current sensing. Load impedance is dynamic, and related to the character of the plasma discharge.

1.3.3 Magnetic Structure

The helicon plasma source has been shown to exhibit three unique modes of operation [32]. When an RF signal is applied to the system in the absence of the axial magnetic field, two modes may be excited: the capacitively-coupled plasma mode (CCP) and the inductively-coupled plasma mode (ICP). In non-propagating discharges, energy penetration is limited to the plasma skin depth, given by:

$$\lambda = \frac{c}{\omega_{p_e}}. \tag{1-1}$$

This expression for the skin depth is valid for $\omega << \omega_{p_e}$, which is easily satisfied for the conditions under consideration.

Alternatively, in the wave-coupled mode of operation in which an imposed axial magnetic field is present, RF energy can penetrate to the center of the plasma, resulting in energy deposition far from the plasma edge and offering the potential for much higher density. In the experimental apparatus under consideration, this axial magnetic field is produced with a single electromagnetic solenoid comprised of 162 turns of 66 mm square cross-section copper conductor. The coil is wound on a single aluminum bobbin and has length 12 cm, outer radius of 9.5 cm, and inner radius 3.5 cm. The polyurethane insulation is rated to 200 °C, ultimately limiting the full-field run time for the assembly. The total resistance of the wound copper conductor is 0.03 Ω. The maximum current delivered to the assembly is 180 A, resulting in a total power consumption of approximately 970 W at maximum field. Experimental measurements using a Hall-effect sensor show that the axial magnetic field strength scales at 11 Gauss per Ampere on axis.

Future plans for the thruster magnetic assembly include the removal of the electromagnets in favor of a high field rare-earth permanent magnet assembly.

1.3.4 Confinement Structure

The neutral confinement structure in this experimental study was a thin-wall fused silica quartz tube. The inner diameter of the confinement tube is 2 cm. The wall thickness is 1.5 mm, giving an outer diameter of 2.3 cm.

Future plans for the experiment include replacement of the transparent quartz confinement tube with an opaque alumina tube to limit radiative heating of the surrounding structure. In a fully integrated thruster, heating of the surrounding permanent magnet assembly must be carefully controlled in order to avoid exceeding the Curie point of the magnets, and the consequent field degradation. This is especially problematic in very high field neodymium-iron-boron magnets, whose Curie temperatures may be as low as 353 K. Material properties for quartz and alumina are given in Tables 1-4 and 1-5 below.

Physical Properties for Fused Silica at 20°C		
Density	2203	kg/m^3
Hardness	5.5 - 7.0	Mohs Scale
Specific Heat	740	J/(kg·K)
Thermal Diffusivity	0.00848	cm^2/s
Thermal Conductivity	1.3	W/(m·K)
Electrical Resistivity	$>10^{18}$	Ω·m
Softening Point	1650	°C

Table 1-4: Properties of fused silica used in current neutral particle confinement tube on mHTX.

Physical Properties for Alumina at 20°C		
Density	3984	kg/m^3
Hardness	9.0	Mohs Scale
Specific Heat	755	J/(kg·K)
Thermal Diffusivity	0.111	cm^2/s
Thermal Conductivity	33.0	W/(m·K)
Electrical Resistivity	10^{12}	Ω·m
Melting Point	2054	°C

Table 1-5: Properties of alumina to be used in future revision of neutral particle confinement tube on mHTX.

1.3.5 Propellant Feed System

Primary components associated with the propellant feed system are shown in Figure 1-2. Propellant gases are stored in high-pressure gas cylinders at up to 4500 psi. The pressure regulator reduces this pressure to the 20 – 25 psi level required by the flow controller. The isolator shown in the schematic below is necessary to prevent the induction of spurious signals onto the flow control electronics contained in the flow controller. The flow controller is comprised of a "hot-wire" mass flow sensor that provides feedback to drive an electrically actuated solenoid valve. This provides precise control of propellant flow rate between 0 – 100 sccm.

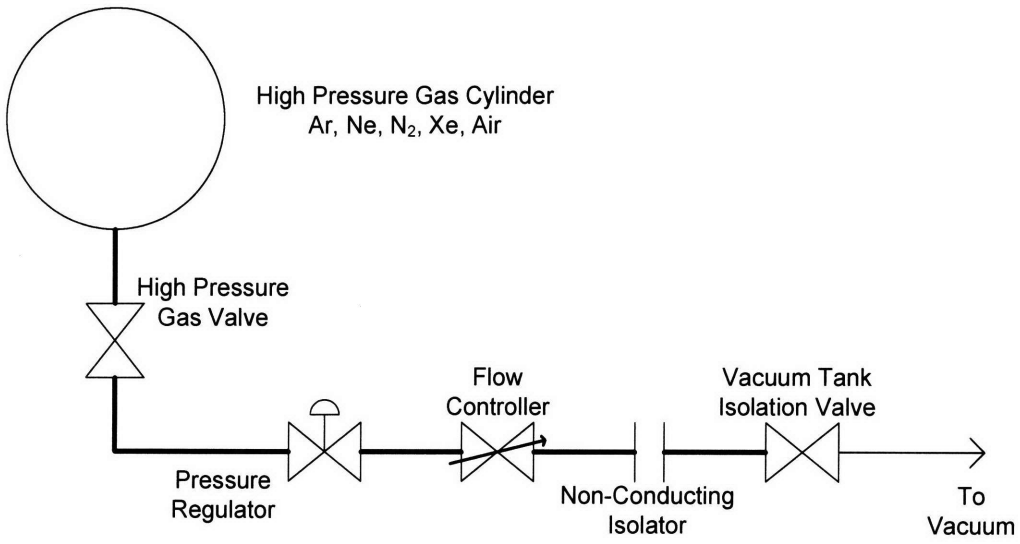

Figure 1-2: SPL Propellant Feed System for mHTX. Current experimental work uses argon propellant.

Chapter 2

Power Balance

In considering the overall power balance of a helicon plasma source as a thruster, there are several small-scale effects which contribute to inefficiency and tend to increase the propellant plasma cost-per-ion. Microscopic effects are considered. These microscopic effects are grouped into lumped loss terms which are used to define the power balance.

2.1 Microscopic Loss Effects

2.1.1 Transmission Losses

First, power is dissipated in ohmic losses in the transmission line and antenna structure and some power is reflected due to impedance mismatch. The RF power measured in the helicon experiment in the SPL includes the ohmic losses in the transmission hardware. Losses in the coaxial cable connecting the RF power supply to the impedance matching network can be estimated. The cable is standard RG-213/U with loss –4.9 dB/100 m.

It is well known that for RF currents flowing in conductive media, current density increases toward the surface of the conductor. In a plane conductor, the decay of current density with increasing distance from the surface is exponential and has the form:

$$J(d) = J_S \exp(-d/\delta). \tag{2-1}$$

This is called the skin effect [33]. The constant δ is the skin depth. From the form of Equation 2-1, the skin depth is the distance from the conductor surface at which current density has been reduced by a factor of e^{-1}. For a good conductor, the skin depth is approximately given by

$$\delta = \frac{1}{\sqrt{\pi f \mu_o \mu_r \sigma}}. \tag{2-2}$$

Here σ is the electrical conductivity of the material and μ_r the relative permeability. This causes the effective resistance of any solid conductor to increase with increasing frequency. For the case of copper ($\sigma = 5.96 \times 10^7$ S/m, $\mu_r = 1$) operating at 13.56 MHz, we obtain a skin depth $\delta \approx 17.7$ μm.

Clearly, transmission losses can be reduced somewhat by reducing operating frequency, thereby increasing the skin depth and decreasing the resistance per unit length. Figure 2-1 below shows the dependence of skin depth (and thus resistance) on frequency in copper.

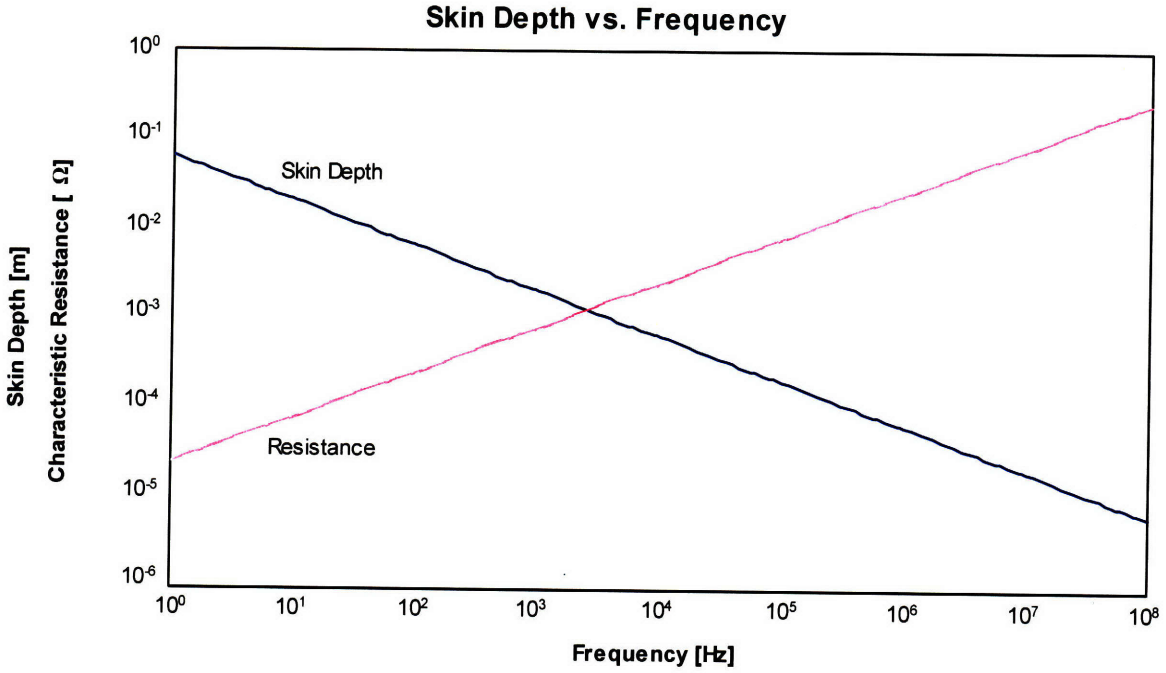

Figure 2-1: Log-log plot of skin depth and characteristic resistance as a function of operating frequency. Note that the characteristic resistance has units [$\Omega \cdot m^2 / m^2$].

Physical Properties for Copper		
Density	8960	kg/m^3
Hardness	3.0	Mohs Scale
Specific Heat	385	$J/(kg \cdot K)$
Thermal Diffusivity	1.116	cm^2/s
Thermal Conductivity	385	$W/(m \cdot K)$
Electrical Resistivity	1.7×10^{-6}	$\Omega \cdot m$
Melting Point	1083	°C

Table 2-1: Property data for copper.

Additional losses associated with the matching network are neglected in this analysis. This circuit is comprised of reactive elements whose dissipative losses are assumed to be small compared to the ohmic losses associated with the balance of the transmission hardware.

2.1.2 Ionization and Excitation

In order to make use of electromagnetic body forces to accelerate the propellant gas, particles must first be ionized. The RF power supplied to the propellant gas must therefore provide the energy required for ionization.

If we assume that the neutral gas is fully ionized, and given the ionization energy for the species under consideration, we can compute the power required for ionization:

$$P_{ION} = \frac{e\varepsilon_i F \rho N_A}{60 M_M}. \tag{2-3}$$

Here, F is volumetric flow rate in standard cubic centimeters per minute (sccm), N_A is Avogadro's number, M_M is the molar mass of the species, and ρ is the density of the species at STP. Substituting the appropriate values for argon given in Table 2-2, we can express the power required for ionization more simply $P_{ION} \cong 1.13F$.

Physical Properties for Argon		
Density (STP)	1.633	kg/m^3
Molar Mass	39.948	g/mol
First Ionization Energy	15.76	eV
Second Ionization Energy	27.63	eV
Heat Capacity (298.15K)	20.786	J/(mol·K)
Melting Point	-189.35	°C
Boiling Point	-185.85	°C

Table 2-2: Property data for argon.

As might be expected, the power consumed in propellant ionization is linear in ionization energy, and inversely proportional to the molar mass of the species. This simple linear relation is plotted over the range of flows of interest in Figure 2-2 below.

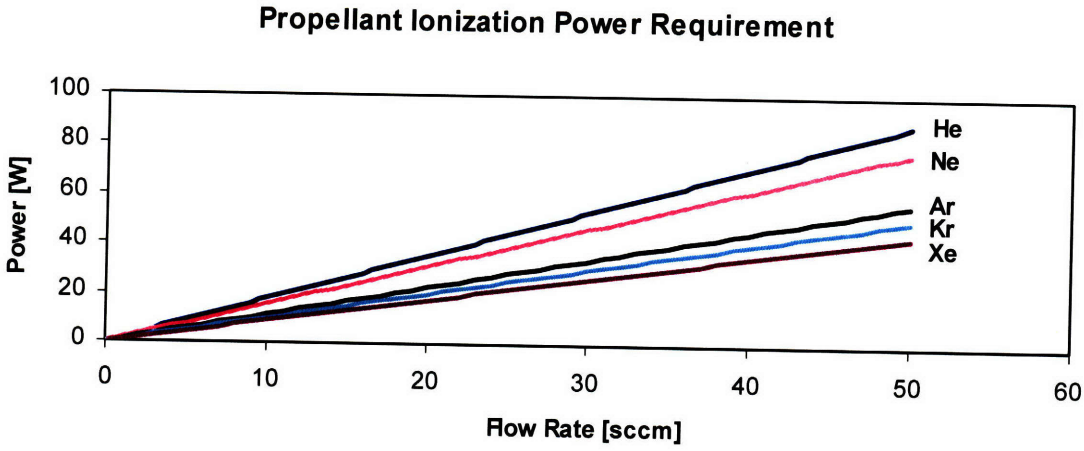

Figure 2-2: Ideal power required for full ionization of several noble gas propellants. Power required for ionization is governed by ε_i, the ionization energy for the species.

Ionization cross section of argon neutrals is a function of the incident electron energy. There is a great wealth of empirical data available for electron-atom collision cross sections in argon [34]. Using these data, it is possible to construct a semi-empirical expression for the total ionization cross section [35]. This expression has the form:

$$Q_i = \left[\frac{L}{M+x} + \frac{N}{x}\right]\left[\frac{y-1}{x-1}\right]^{1.5}\left[1+\frac{2}{3}\left(1-\frac{1}{2x}\right)\ln\left(2.7+(x-1)^{0.5}\right)\right]. \qquad (2\text{-}4)$$

Here ε is the incident electron energy in keV. The constants L, M, N, and P are chosen to fit empirical data sets [36, 37] for the experimentally verified cross sections. These constants are given in Table 2-3. The parameter y is $\varepsilon/\varepsilon_i$, and the parameter x is ε/P.

In addition to ionization, electron collisions excite neutrals. The energy absorbed by neutrals in excitation can be lost in de-excitation or can form metastable states. When this de-excitation occurs, the energy absorbed by the atom during collision is lost as radiation. We can

model the excitation cross section for argon in a similar way as above. The expression for the excitation cross section is given by:

$$Q_{EX} = \frac{1}{F(G+\varepsilon)} \ln \frac{\varepsilon}{\varepsilon_{EX}}. \tag{2-5}$$

F and G are two adjustable parameters and ε_{EX} is the excitation threshold energy. Again, an empirical data set [37] is used to compute numerical values for these parameters. Their values are given in Table 2-3 and the resultant plot of these cross sections as a function of incident electron energy in argon is given in Figure 2-3 below.

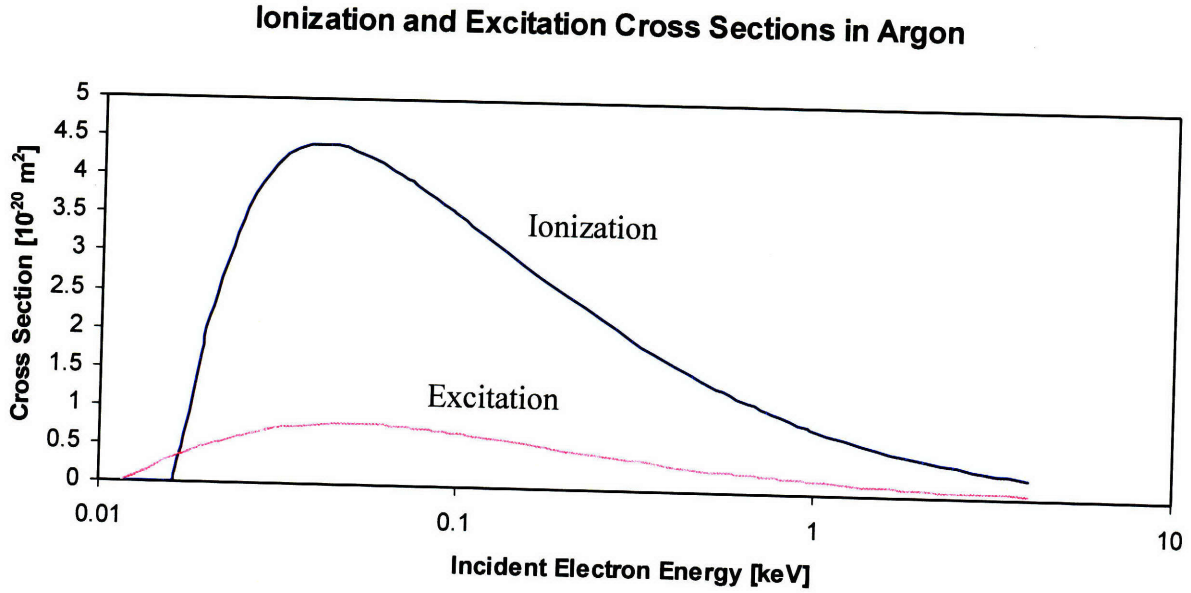

Figure 2-3: Brusa model for the total ionization and total excitation cross-sections in argon as a function of incident electron energy. The ionization cross section reaches a maximum value of $Q_i \approx 4.4 \times 10^{-20}$ m^2 at $\varepsilon \approx 40$ eV. The excitation cross section reaches a maximum value of $Q_{EX} = 7.927 \times 10^{-21}$ m^2 at $\varepsilon \approx 50$ eV.

Brusa Model Parameters for Argon		
ε_{EX}	11.5	(eV)
F	25.19	$keV^{-1}\ 10^{-20}\ m^2$
G	2.36E-02	keV
L	78.76	$10^{-20}\ m^2$
M	18.62	
N	25.66	$10^{-20}\ m^2$
P	0.00842	keV

Table 2-3: Parameters for computing the total ionization and total excitation cross-sections in argon. Computed cross section is expressed as a function of electron energy.

By comparing the relative magnitude of the ionization and excitation cross sections, we can see that, in the range of electron energies of interest (20 – 100 eV), ionizing collisions are likely to dominate exciting collisions. We can therefore expect that losses due to neutral excitation will be small, and can subsequently be neglected.

2.1.3 Hot Neutral Flux

Once the RF power has been deposited in the feed gas, there are further losses due to the flux of hot neutrals to the wall of the source tube. Because of the high degree of ionization [38] (approximately 99%) present in the vicinity of the helicon antenna and in the downstream plasma, it is reasonable to assume that thermal losses associated with neutrals will be low.

2.1.4 Radial Plasma Diffusion

The axial magnetic field necessary to excite the helicon wave-mode also aids in plasma confinement. However, plasma can diffuse across magnetic field lines to intercept the tube, where the ions surrender their ionization energy during recombination. Because the magnetic field is not strictly uniform down the length of the tube, there is the possibility of ions streaming

freely along the field lines until they intercept the walls of the source tube due to curvature in the field.

2.1.5 Non-Ideal Utilization

Hot neutrals that escape into the plume do not experience electromagnetic body forces and essentially leave the tube with their thermal speed, in which case, the RF energy used to heat them is wasted. As discussed previously, the high degree of ionization associated with the helicon plasma source largely precludes this loss mechanism from playing a major role in the overall power balance.

2.1.6 RF Irradiance

Some fraction of RF power is lost in non-ideal coupling of RF radiation from the antenna to the plasma. Transmitted RF will be scattered and dissipated through interactions with the walls of the vacuum chamber. The operating frequency of 13.56 MHz corresponds to a wavelength of 22.1 meters. Because the non-conducting windows of the vacuum tank are much smaller than the vacuum electromagnetic wavelength, propagating electromagnetic radiation will remain effectively shielded inside the tank. In order to measure the losses due to RF irradiance, measurements must be taken from inside the vacuum chamber.

2.1.7 Transmitted Radiation

We can gauge the relative importance of losses due to transmitted plasma radiation by studying the radiation characteristics typical of argon, given in Table 2-4, and comparing these against the transmission characteristics of fused silica, given in Figure 2-4.

Persistent Strong Argon Spectral Lines		
Intensity	Wavelength (nm)	Spectrum
150	66.186900	Ar II
300	67.094550	Ar II
1000	67.185130	Ar II
1000	72.336060	Ar II
180	86.679997	Ar I
150	86.975411	Ar I
180	87.605767	Ar I
180	87.994656	Ar I
150	89.431013	Ar I
300	91.978100	Ar II
300	93.205370	Ar II
1000	104.821987	Ar I
500	106.665980	Ar I

Table 2-4: Vacuum wavelength of high-intensity persistent argon spectral lines. Wavelengths are uniformly below the transparency cutoff for quartz and will therefore contribute to confinement tube heating [39-41].

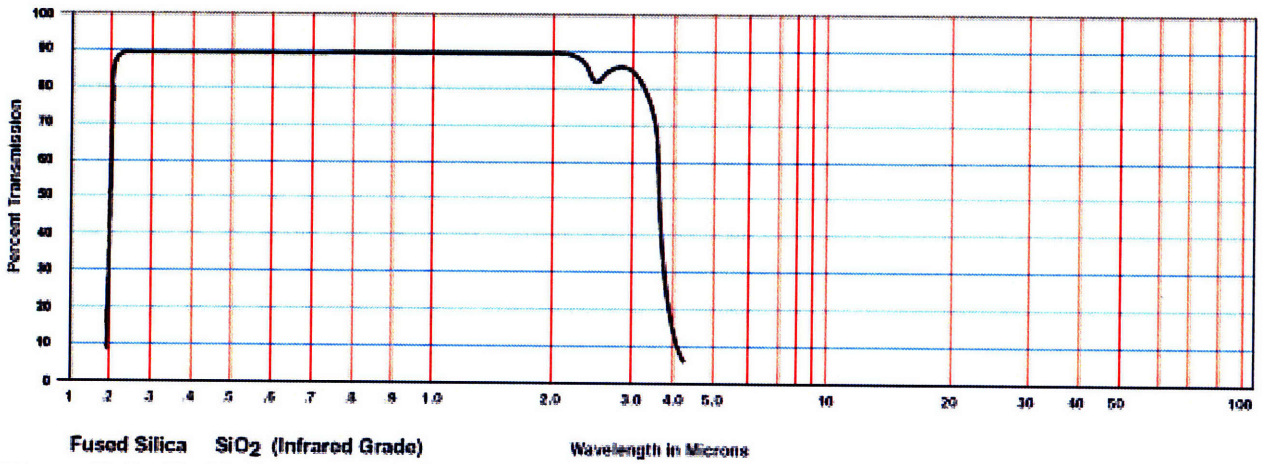

Figure 2-4: Radiation transmission characteristics of fused silica. Transparency increases very sharply at approximately 200 nm, and declines sharply above 3000 nm [42].

Based on the number and relative intensity of persistent spectral lines whose wavelength fall below the lower cutoff transmission wavelength of 200 nm in fused silica, it is reasonable to assume that the fraction of power lost from the system in the form of transmitted radiation is small compared to that which is captured. Nonetheless, there are many blue Ar II lines, and the

radiative contribution by these will contribute to the power balance of the system. In the absence of experimental data, however, these losses are not quantified in this analysis. Future work on this problem might characterize these losses rigorously using bolometry.

2.1.8 Plume Power

The plume power associated with any rocket device can be expressed most simply as the jet kinetic power:

$$P_{PLUME} = \frac{1}{2}\dot{m}c^2. \tag{2-6}$$

Here $\dot{m}$ is the mass flow rate in kg/s, c is the exhaust velocity and P_{PLUME} is given in Watts. Unfortunately, the exhaust velocity associated with the helicon thruster is non-uniform and the plume is slightly divergent. We know that the thrust is the product of mass flow rate and exit velocity. We can recast the plume power in terms of the thrust:

$$P_{PLUME} = \frac{F^2}{2\dot{m}}. \tag{2-7}$$

The effect of the non-uniform, radially integrated exhaust velocity is captured in the direct measurement of the thrust force. Figure 2.5 shows such a direct thrust measurement for the mHTX as a function of mass flow rate.

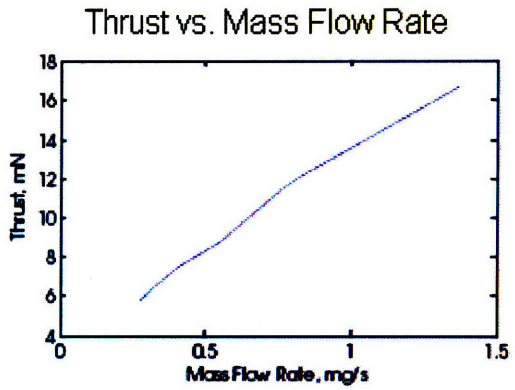

Figure 2-5: Thrust versus mass flow rate measurement for P_{RF} = 635W, B_0 = 1540G as a function of mass flow rates of argon. This Figure adapted from Reference 31.

Using existing data we can compute an approximate power output in the plume. The standard volumetric flow rate of 20 sccm used in this study corresponds to a mass flow rate of approximately 0.55 mg/s.

2.2 Macroscopic Effects

2.2.1 Transmission Hardware Heating

In order to estimate the ohmic losses associated with the transmission hardware, especially the RF feed through into the vacuum tank, we can measure the heating rate of the vacuum feed through and from this determine the amount of power lost to ohmic heating.

2.2.2 Confinement Tube Heating

Several of the microscopic heating mechanisms discussed in the previous section contribute to the effect of heating the walls of the neutral confinement tube. Specifically, plasma diffusion, radiation by plasma in wavelengths absorbed by fused silica, and the diffusion of hot neutrals all

result in confinement tube heating. Derivation of heat flux based on temperature evolution on the outer wall of the confinement tube will be discussed in the following chapter.

2.2.3 Plume Power

Plume output power measurements can be obtained from previous research [31], as described in Section 2.1.8 and given in Figure 2-5. In this study the plume power is particular to the operating conditions of the experiment. Without scaling laws describing the variation of plume power with input power, these results cannot be directly generalized to other experimental conditions. In particular no information about the input power variation of efficiency can be extracted.

2.2.4 RF Flux Measurements

Uncoupled electromagnetic radiation which leaves the system can be measured directly using an RF Flux meter. For this analysis, RF flux will be assumed to be isotropic, based on the reflective nature of the vacuum chamber walls, so that the total radiated power is given by

$$P_{RF_{OUT}} = \int_S \phi_{RF}\, ds\,. \tag{2-8}$$

2.3 Power Balance

Using the measured variables discussed in Section 2.2 above, we can define the power balance in terms of measureable variables as follows:

$$P_{RF_{IN}} - P_{TRANS} - P_{ION} - P_{TUBE} - P_{PLUME} - P_{RF_{OUT}} = 0. \quad (2\text{-}9)$$

In the expression above, $P_{RF_{IN}}$ is the RF power input to the system from the power supply, P_{TRANS} the power dissipated in transmission hardware, P_{ION} the power required to ionize the propellant gas, P_{TUBE} the power lost to the walls of the neutral confinement tube, P_{PLUME} the plume power computed directly from thrust measurements, and $P_{RF_{OUT}}$ the uncoupled electromagnetic radiation that is reflected and dissipated along the walls of the vacuum chamber. As discussed previously, contributions due to neutral excitation, transmitted radiation, and non-ideal utilization are expected to be small. These effects will be neglected in the analysis of the sections that follow.

Having defined the power balance of the system we can now characterize the efficiency. This is the ratio of the useful power output of the system, in this case the plume power, to the total input power:

$$\eta = \frac{P_{PLUME}}{P_{RF_{IN}}}. \quad (2\text{-}10)$$

By performing a global characterization of the loss mechanisms in the system, this work will establish a path toward reducing losses and improving overall system efficiency.

Chapter 3

Benchmarking

A methodology and apparatus for obtaining heat flux data from temperature data is outlined in the sections that follow. Numerical simulation of the confinement tube thermal response is performed and compared against experimental data to validate the approximated governing equation for heating rate. A baseline experiment using this approach is discussed. Results of this baseline experiment are presented. The baseline experiment indicates that measurements taken at low temperatures can be used to determine incident heat flux to 10% accuracy.

3.1 Analytic Approach

The thermal response of the neutral confinement tube to heat input at the inner boundary is governed by the heat equation. For a temperature-invariant thermal conductivity, we can express the heat equation in cylindrical coordinates:

$$\rho c_p \frac{\partial T}{\partial t} = k\left(\frac{1}{r}\frac{\partial}{\partial r}\left(r\frac{\partial T}{\partial r}\right)+\frac{1}{r^2}\frac{\partial^2 T}{\partial \theta^2}+\frac{\partial^2 T}{\partial z^2}\right). \tag{3-1}$$

The governing equation is subject to boundary constraints on the inner and outer surfaces of the neutral confinement tube:

$$\begin{cases} q(r = R_i) \equiv -k\nabla T = \phi_r \\ q(r = R_0) \equiv \alpha\sigma T_o^4 \end{cases}. \tag{3-2}$$

We can use some relevant insights to reduce the dimension of the problem. First, we assume that the thermal deposition on the inner boundary is azimuthally symmetric, so that the temperature T has no angular dependence.

Axial gradients in temperature are driven by the axial gradient of radial heat flux. Radial temperature gradients, on the other hand, are driven by the local heat flux, according to Fourier's law of conduction. Thus, for a scalar conductivity, the ratio of the axial-to-radial temperature gradients varies in the following way:

$$\frac{\nabla_z T}{\nabla_r T} \propto \frac{\nabla_z \phi_r(z)}{\phi_r(z)}. \tag{3-3}$$

If we assume that the local radial heat flux is much greater than the axial variation, then it is clear that the effects due to axial gradients in temperature can be neglected. This is borne out experimentally, as typical axial gradients, $\nabla_z T \cong 40\,\mathrm{K/cm}$, compared to typical radial gradients, $\nabla_r T \cong 200\,\mathrm{K/cm}$.

Finally, because the thickness of the neutral confinement tube is small compared to the outer radius, $d/R_0 \cong 0.13$, we can neglect radial effects, including the effect of the radial geometry on the steady-state thermal gradient. Approximating the tube as a flat surface, the steady state distribution becomes linear and can be written:

$$\left|\frac{\Delta T}{\Delta x}\right| = \frac{\phi_r(z)}{k}. \tag{3-4}$$

Substituting the thermal conductivities for quartz given in Table 1-4, as well as the relevant dimensions for the neutral confinement tube and the range of heat fluxes of interest (1 W/cm^2 $\leq$ $\phi_r(z)$ $\leq$ 3 W/cm^2), we obtain a the resultant temperature drop (10.9 K $\leq \Delta T \leq$ 32.6 K). Even when compared only to standard temperature, this gradient is negligibly small.

Using these simplifications, we can now integrate the heat equation between the inner and outer radius of the neutral confinement tube to obtain the ordinary differential equation:

$$\rho c_p \frac{dT}{dt}(R_O - R_I) = \rho dc_p \frac{dT}{dt} = \int_{R_O}^{R_I} (-k\nabla T)dr = \phi(r = R_I) - \phi(r = R_O) = \phi_r - \alpha\sigma T^4. \tag{3-5}$$

In the steady state, it is clear that the input heat flux, ϕ_r, is balanced by the radiated power:

$$\phi_r = \alpha\sigma T_{EQ}{}^4. \tag{3-6}$$

The parameter α is the gray-body parameter. For real processes this parameter takes a value $\alpha < 1$. This parameter captures the non-ideal nature of the radiative heat transfer, and has the effect of driving up the required equilibration temperature. For the heat flux ranges of interest, we can compute a conservative equilibration temperature by assuming the neutral confinement tube radiates as a blackbody. The heating range 1 W/cm^2 $\leq \phi_r(z) \leq$ 3 W/cm^2 corresponds to a final equilibrium temperature of 648 K $\leq T_{EQ} \leq$ 853 K. While $T_O << T_{EQ}$, corresponding roughly to $T_O \leq 0.6T_{EQ}$, the radiation term can be neglected, and the heat equation reduces to the simple form:

$$\rho dc_p \frac{dT}{dt} = \phi_r(t). \tag{3-7}$$

We can integrate to obtain:

$$T = T_0 + \frac{1}{\rho dc_p}\int_0^t \phi_r(s)\,ds = T_0 + \frac{\langle \phi_r \rangle(t)}{\rho dc_p}. \tag{3-8}$$

This solution is clearly linear in time. In this way, by measuring the slope of the linear portion of the temperature growth on the outer surface, we can find the associated heat flux, $\langle \phi_r \rangle$. By integrating the measured heat flux down the length of the quartz tube, it is then possible to evaluate the power lost.

In order to assess the validity of the quasi-static, zero-dimensional analysis, described above, as a means of computing the heat flux to the confinement tube walls, it is helpful to first obtain a thermal response baseline, wherein the total input power is known. By evaluating the energy balance using temperature measurements, we can compare the resulting computed power

to the known input power. This will yield a measure of the error that we can associate with this approach.

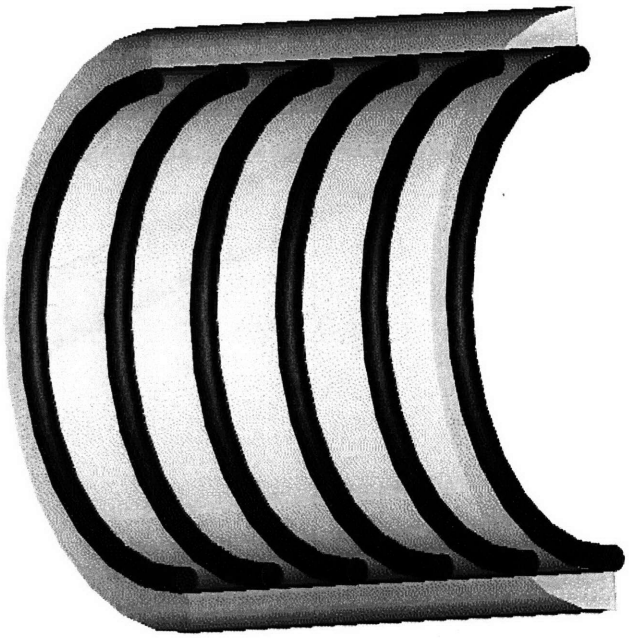

Figure 3-1: Cutaway of particle confinement tube outfitted with helical resistive element. Resistor is wound from 22 AWG Nichrome-A stock. Total wound length is 23 cm without compression. Resistance is $R_C \approx 7.4\ \Omega$.

The diagram above illustrates the apparatus for performing the baseline experiment. The source tube is fitted with a wound resistor in thermal contact with the inner wall of the source tube. The tube measures 40 cm in length by 2 cm inner diameter. Wall thickness is 1.5 mm.

By simultaneously measuring the temperature of the resistive element and the outer wall of the confinement tube, we can evaluate the total change in the internal energy of the system over a given interval of time. This change in energy per unit time is the power we wish to quantify.

Temperature data will be taken with laminated K-type thermocouples on the surfaces of interest, as shown in Figure 3-2.

Figure 3-2: Thermocouple placement along confinement tube. Five K-type thermocouples are bonded at equal intervals along the 40 cm length.

3.2 Numerical Simulation

We can create a numerical model for the system based on the simplifying assumptions presented in the previous section. We have assumed that the system can be modeled using Equation 3-5. We can create a simple finite difference model of this ordinary differential equation to further test the validity of this assumption. The time-rate-of-change in temperature can be approximated:

$$\frac{dT}{dt} \cong \frac{T_{i+1} - T_i}{\Delta t}. \tag{3-9}$$

Similarly, the temperature, which is a function of time, can be approximated:

$$T(t) \cong \frac{T_{i+1} + T_i}{2}. \tag{3-10}$$

Using these finite difference approximations, for constant heat flux, ϕ_r, Equation 3-5 can be written:

$$\rho d c_P \left(\frac{T_{i+1} - T_i}{\Delta t} \right) = \phi_r - \alpha\sigma \left(\frac{T_{i+1} + T_i}{2} \right)^4. \tag{3-11}$$

The gray-body parameter, α, can be varied to provide the best fit to empirical data. In this way, numerical modeling of the system can better quantify any deviation from the ideal blackbody case. There are two methods by which we can simulate the behavior of the system. The first is

to factor Equation 3-11 completely and solve the resulting fourth-order polynomial directly for the roots in δT. The second method involves linearizing Equation 3-11 by assuming that the temperature increase during each time step is approximately linear. Each of these are discussed in the sections that follow. Each simulation will be compared against the experimental data shown in Figures 3-3 and 3-5, using the heat flux derived from the linearized curves in Figures 3-4 and 3-6.

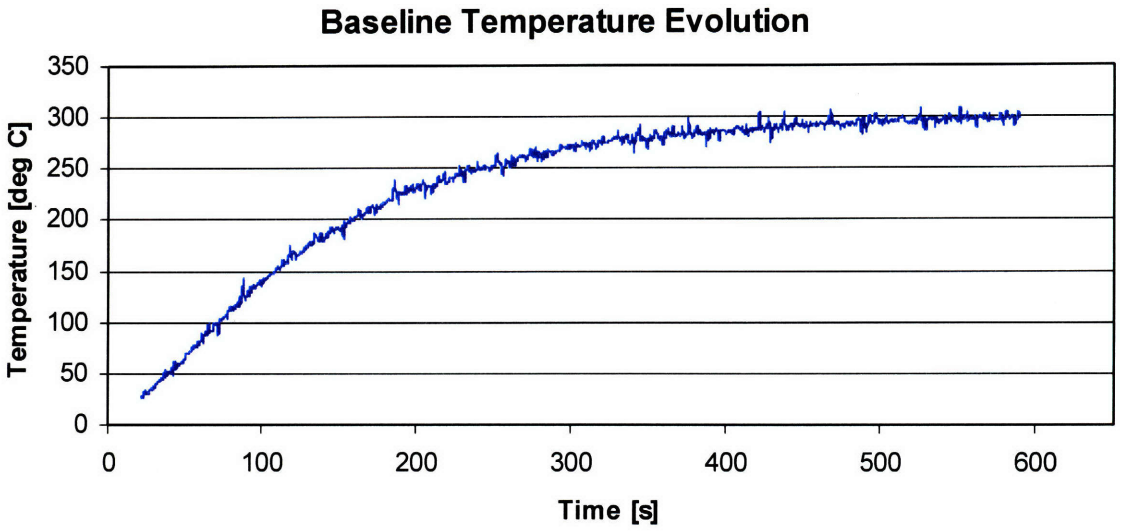

Figure 3-3: Temperature growth and saturation for baseline thermal response test. In this experimental run, temperature is taken from TC2, which is partially occluded by centering clamp (see Figure C-2 for detailed experimental setup).

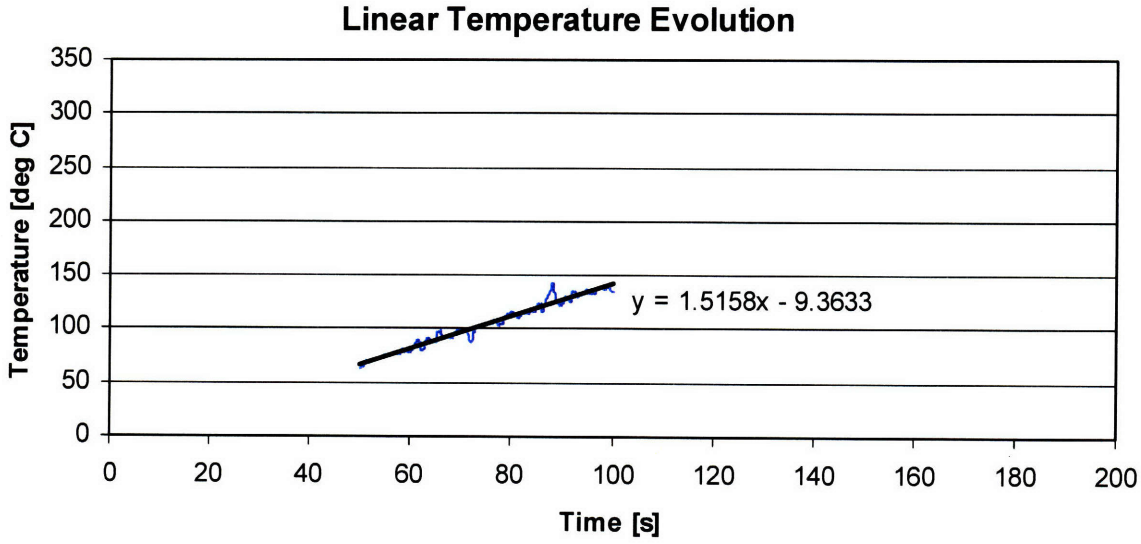

Figure 3-4: Linearized temperature growth for baseline thermal response test. The heating rate of 1.5158 K/s corresponds to a thermal energy flux of 0.3460 W/cm^2.

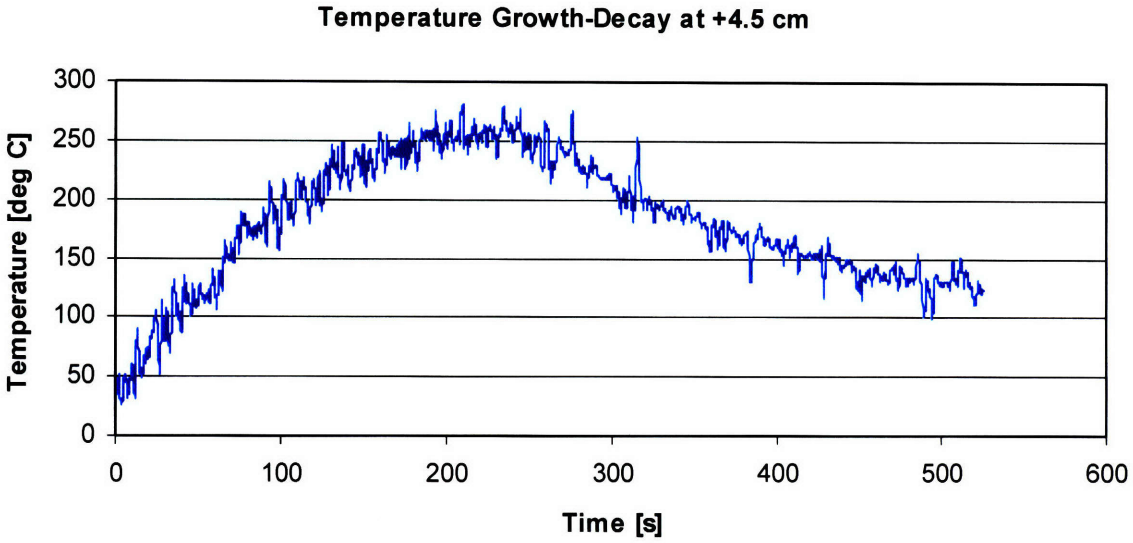

Figure 3-5: Temperature growth saturation and decay for 20 sccm Ar, B = 0.165 T, P_{RF} = 1kw. In this experimental run, tube lip is placed +6 cm forward of plume-side magnet face. Data are for +4.5 cm forward of plume-side magnet face. No appreciable occlusion is present in this configuration.

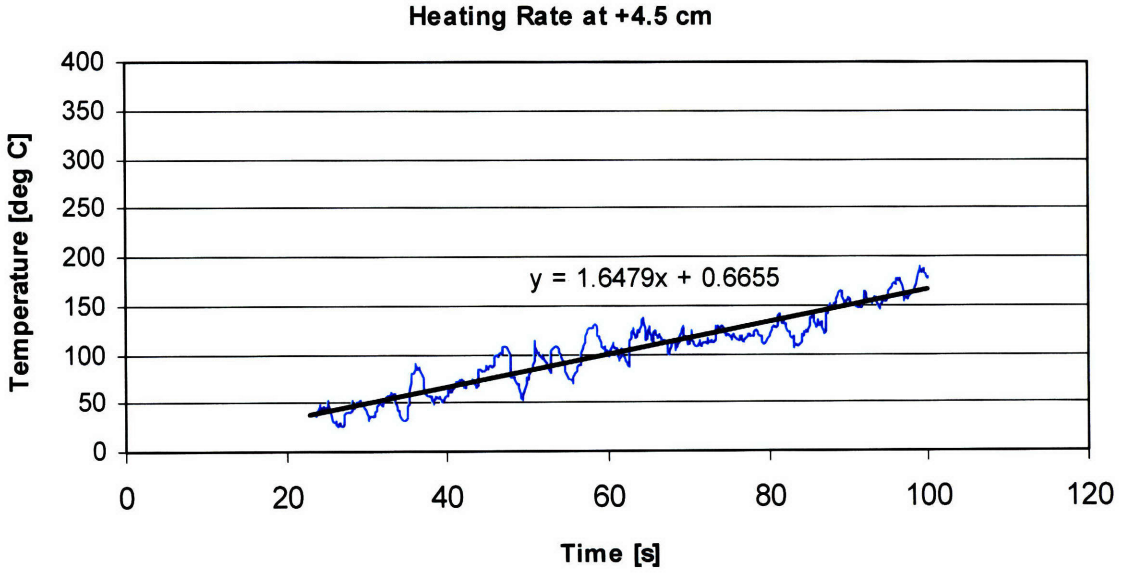

Figure 3-6: Linearized temperature growth for 20 sccm Ar, B = 0.165 T, P_{RF} = 1kw. The heating rate of 1.6479 K/s corresponds to a thermal energy flux of 0.376 W/cm^2.

We will see that modeling of temperature decay properties, as given in Figure 3-5, is complicated somewhat by the presence of axial gradients due to uneven cooling in the tube.

MATLAB code for both the exact and linearized methods are given in Appendix B.

3.2.1 Exact Solution

Expanding Equation 3-11 yields a fourth order polynomial in T_{i+1}. Carrying out the expansion, Equation 3-11 can be expressed:

$$T_{i+1}{}^4 + 4T_i T_{i+1}{}^3 + 6T_i{}^2 T_{i+1}{}^2 + \left(4T_i{}^3 + \frac{16\rho c_p d}{\alpha\sigma\Delta t}\right)T_{i+1} + \left(-\frac{16\phi_r}{\alpha\sigma} + T_i{}^4 - \frac{16\rho c_p d}{\alpha\sigma\Delta t}T_i\right) = 0 . \quad (3\text{-}12)$$

The solution for T_{i+1} is the contained in the roots of this polynomial expression. We require that the solution for the new temperature must be a positive, real-valued, and that $T_{i+1} > T_i$ for $\phi_r > 0$. A quartic polynomial with real coefficients, as in this case, may have four real roots, two real roots and one pair of complex roots, or two pairs of complex roots.

By implementing this expression in MATLAB, we can compare the simulated result with experimental data. This method consistently returns two real-valued roots, one positive and one negative, and two complex roots forming a conjugate pair. Valid temperature data is thus limited to only one root.

The simulated baseline and growth-decay curves computed using this method are presented in Figures 3-7 and 3-8.

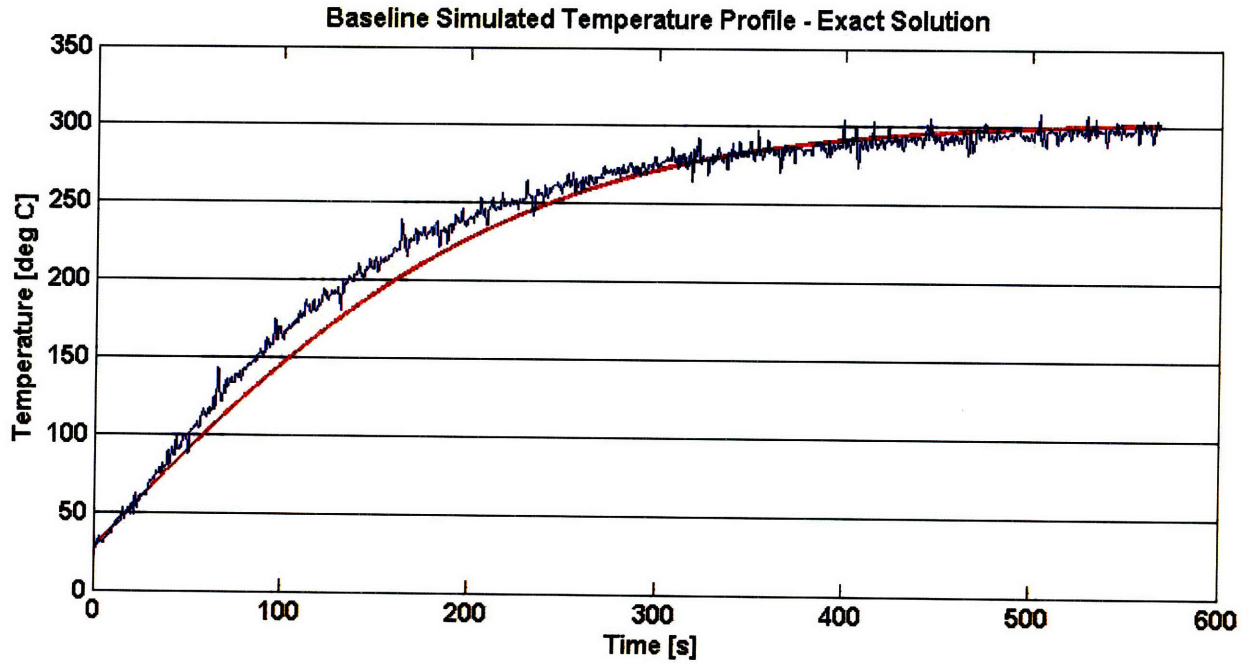

Figure 3-7: Real and simulated thermal response of the neutral confinement tube during the baseline experimental run. Simulated curve is given for $P_{IN} = 3460$ W/m^2 and $\alpha = 0.55$.

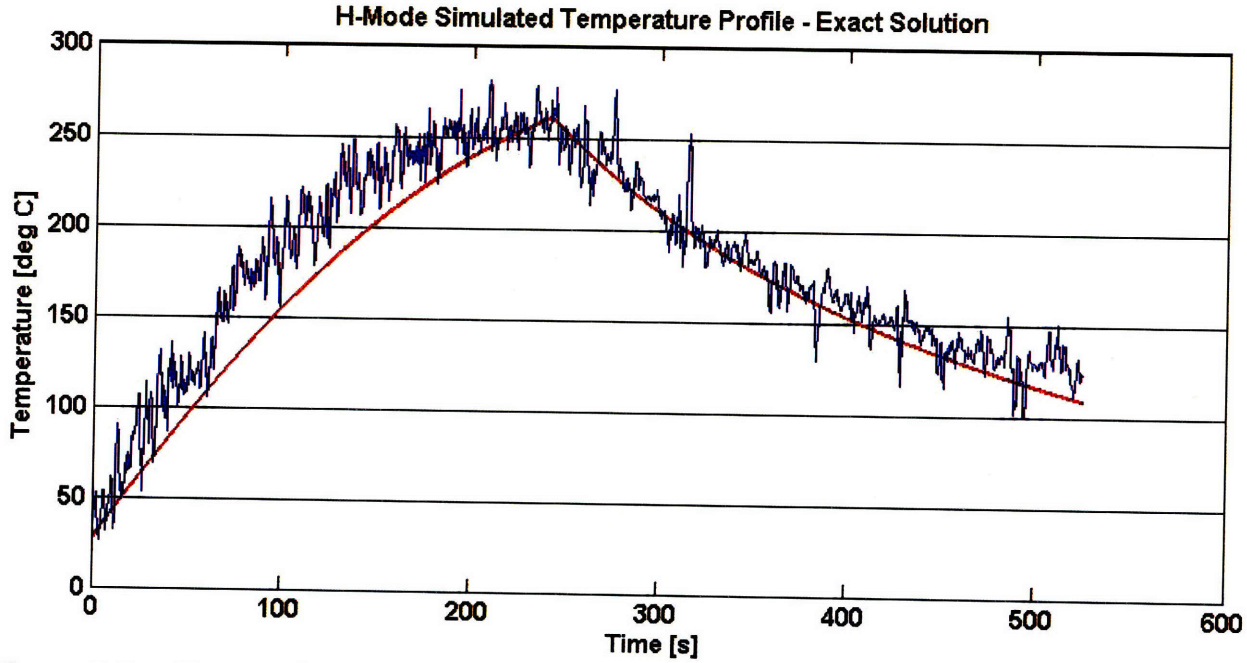

Figure 3-8: Exact solution for finite-difference simulated temperature growth and decay. Simulated curve uses $P_{IN} = 3762$ W/m^2, with blackbody parameter $\alpha = 0.58$.

3.2.2 Linearization

As an alternative to iteratively computing the solution for updated temperature directly as in Section 3.2.1 above, we can also use linearization of Equation 3-11 to obtain an approximate temperature increment per time-step. We assume that the updated temperature value is incrementally greater than the previous value, so that:

$$T_{i+1} = T_i + \delta T . \tag{3-13}$$

We require that the time-step, Δt, be sufficiently small that $\delta T / T_i << 1$. Plugging into Equation 3-11, and discarding all higher order terms in δT, we obtain:

$$\rho c_p d \frac{\delta T}{\Delta t} = \phi_r - \frac{\alpha\sigma}{16}\left(16T^4 + 32T^3\delta T\right). \tag{3-14}$$

We can solve Equation 3-14 for the temperature increment:

$$\delta T = \frac{\phi_r \Delta t - \alpha\sigma\Delta t T^4}{\rho c_p d + 2\alpha\sigma\Delta t T^3}. \tag{3-15}$$

This expression gives a simple means of updating temperature at each time step to approximate the thermal response of the system. Implementing this expression into MATLAB we can compare the result to the experimentally obtained growth characteristics. The simulated baseline and growth-decay curves computed using this method are presented in Figures 3-9 and 3-10.

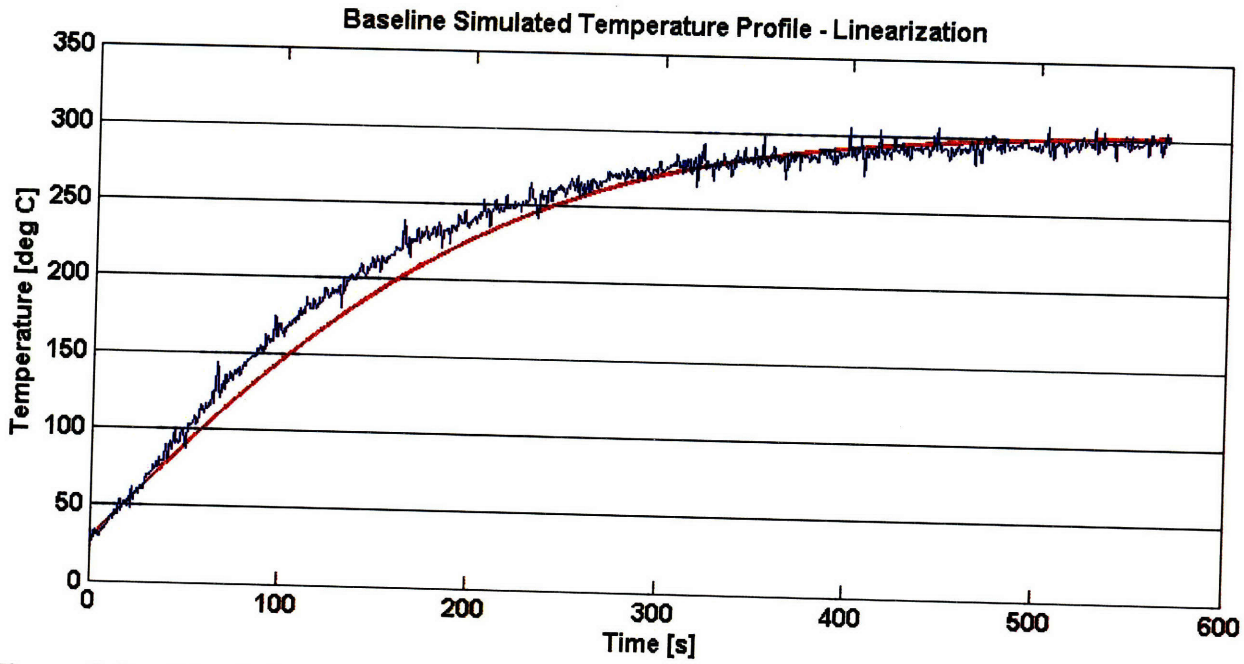

Figure 3-9: Simulation of a baseline thermal response curve using a linearization scheme. Coverage of the thermocouple area by retaining clamp in this experiment drives down the gray body parameter. This plot corresponds to $P_{IN} = 3460$ W/m^2, and $\alpha = 0.55$.

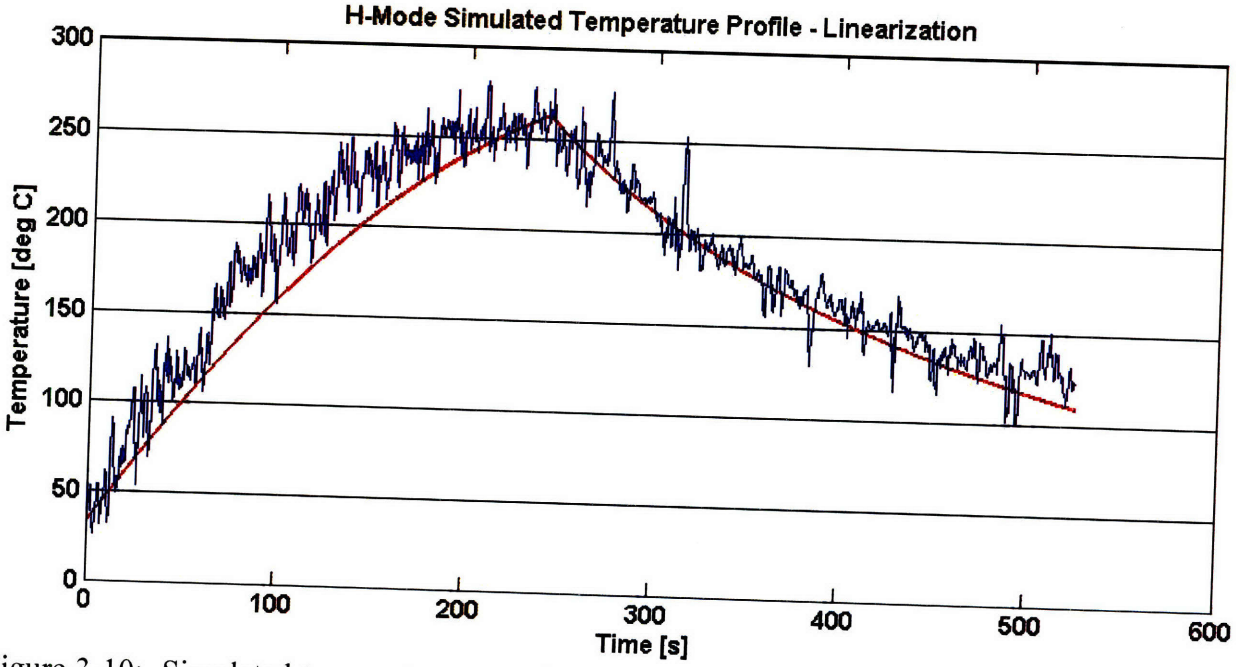

Figure 3-10: Simulated temperature growth and decay using a linearization scheme. Simulated curve uses $P_{IN} = 3762$ W/m^2, with blackbody parameter $\alpha = 0.58$.

It is clear that both methods under predict experimentally obtained results for the choice of parameters shown. This deviation reaches a maximum in the time range between 100 – 150 seconds for both simulations. In the case of the baseline simulated temperature profile, for the choice of gray body parameter and the measured heating rate, maximum deviation is approximately 10%. For the H-Mode heating data, deviation from the centrally averaged temperature is somewhat greater, approximately 15%. One potential explanation for this deviation is the inverse variation in specific heat with increasing temperature, which is not captured in the model. This would explain the temperature variation in heating rate, while admitting the same steady state behavior observed both in the model and experimentally.

3.3 Measurements

The temperature evolution of the particle confinement tube and resistive element were measured as described in section 3.1 above. The resulting temperature profiles are given in Figure 3-11 below.

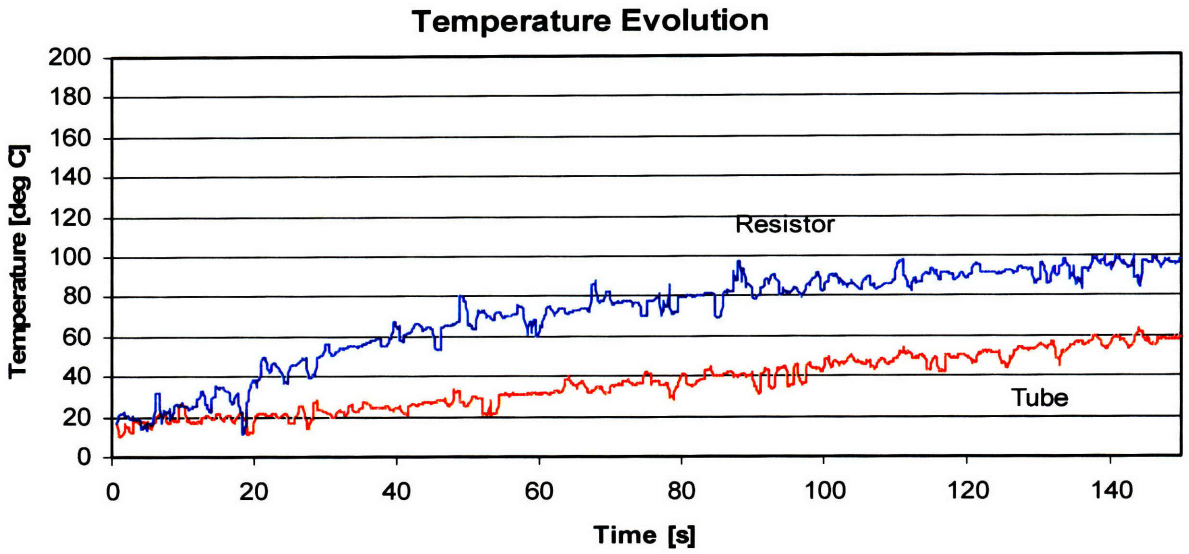

Figure 3-11: Temperature evolution of the resistive element and confinement tube. Power applied to the system is 16.45 W. At this heating rate, thermal response of the outer surface of the source tube requires approximately 25 s.

It is important that we select a region on the curve for which the temperature is low so that we can neglect power losses due to radiation. We must also be sure that sufficient time has passed that the outer surface of the tube has begun to respond to the heat flux. We can see that the data between 30 - 60 seconds roughly satisfies these two requirements. The linearized portion of these two curves is presented in Figure 3-12.

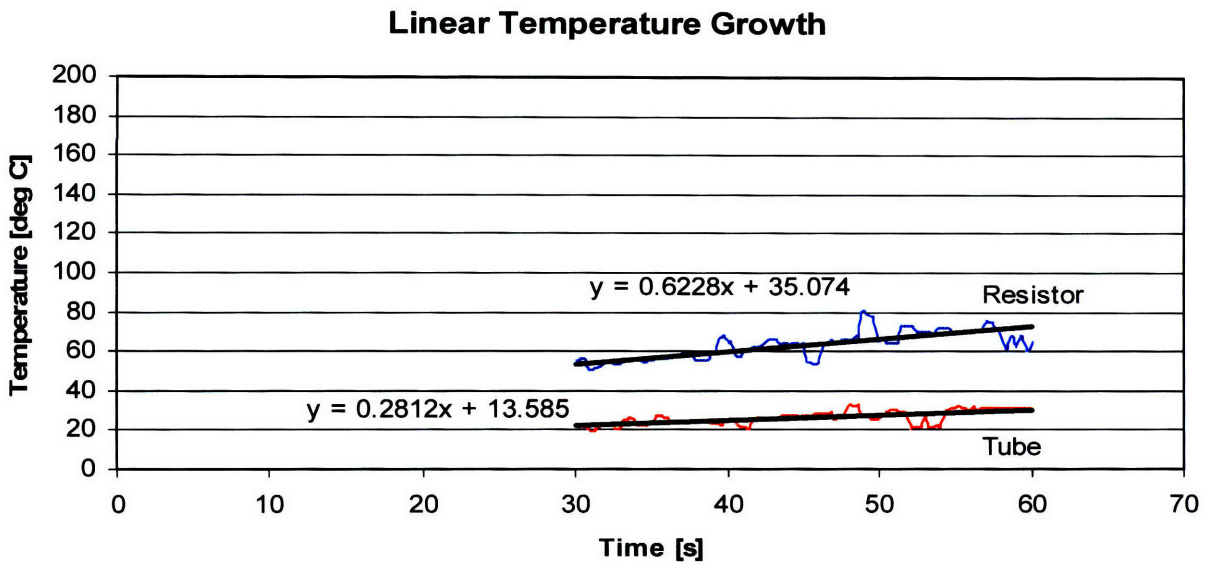

Figure 3-12: Linear fit of temperature data. The data subset is taken immediately following the onset of thermal response on the confinement tube outer surface. Operation below 80 °C ensures that radiative effects can be neglected.

Using the linear fit to these data, we can directly ascertain the variation of temperature with time. The rate of change in the internal energy of the system is given by:

$$\frac{\Delta U}{\Delta t} = m_T c_{P,T} \frac{\Delta T_T}{\Delta t} + m_R c_{P,R} \frac{\Delta T_R}{\Delta t}. \tag{3-16}$$

The subscripts "T" and "R" are included to distinguish between the tube and resistor. The mass of the resistor is measured directly, and we find that $m_R = 0.015$ kg.

We can compute the fraction of the mass of the quartz tube in which we are interested. The resistor is in thermal contact with only 23 cm of the entire tube length. Inputting the properties for the quartz source tube given in Table 1-4, and appropriate dimensional values, we obtain a mass of $m_R = 0.051\,\text{kg}$.

We are now in a position to compute the total change in internal energy per unit time. We can recognize immediately that the $\frac{\Delta T_j}{\Delta t}$ terms are precisely the slopes of the two linear trend lines in Figure 3-12, above. Plugging into Equation 3-12, we find that $P_{COMP} = 14.8\,\text{W}$. We can compare this with the DC power input to the system by the power supply, $P_{IN} = 16.45\,\text{W}$. Thus the error associated with this approach is given by:

$$\varepsilon = \frac{P_{IN} - P_{COMP}}{P_{IN}}. \tag{3-17}$$

This corresponds to an error $\varepsilon = 10\%$.

Chapter 4

mHTX Power Measurements

Measurement of the heating rate for the RF transmission hardware and neutral confinement tube is carried out. From these measurements, power losses are derived. Additional losses are computed for coaxial RF transmission cable, vacuum feed through center conductor, propellant ionization, and plume power.

4.1 Transmission Hardware Heating

Because of the much higher thermal conductivity of copper compared to fused silica, we can assume that axial temperature gradients in copper are relatively small and that equilibration times are short. In considering the losses associated with the transmission hardware as a whole, it is useful to consider the effects of the coaxial cable, the vacuum feed through, and the antenna separately, so that the transmission factor in the power balance becomes:

$$P_{TRANS} = P_{COAX} + P_{ANT} + P_{FT} . \tag{4-1}$$

4.1.1 Coaxial Transmission Cable

As discussed in section 2.1.1, the RF transmission cable that carries the RF signal from the RF power supply to the impedance matching network is a standard RG-213/U coaxial cable with a characteristic loss of -4.9 dB/100m. It should be noted that this rating, in which loss is linear in distance, is only accurate if losses are small. Otherwise, line losses will exhibit logarithmic behavior. This loss is related to the input-to-output power ratio according to the expression:

$$G = 10\log\left(\frac{P_{OUT}}{P_{IN}}\right). \tag{4-2}$$

Converting this to a power ratio, we find that:

$$\frac{P_{OUT}}{P_{IN}} = 10^{\left(\frac{-0.049L}{10}\right)}. \tag{4-3}$$

In this expression, L is the length of the cable in meters. The coaxial transmission cable used in the mHTX has a length of 8 m. Substituting into Equation 4-3, we find that the output power from the coax is approximately 91.3% of the input power. This means that 8.7% of the input power is dissipated in the line itself. This loss fraction is sufficiently small that we may take the linear loss rating associated with the cable as approximately correct. For an input power of 590 W, therefore, we obtain the coaxial transmission loss, P_{COAX} = 51.33 W.

4.1.2 Antenna

Direct measurement of the antenna heating rate is somewhat problematic due to the excessive degree of RF coupling between the antenna and the thermocouple. It is clear that these signals are an induced artifact due to the proximity of the radiant element to the thermocouple junction, and do not represent actual thermal measurements. Cessation of RF signal results in an instantaneous drop in the reported temperature, as given in Figure 4-1 below.

In order to circumvent these difficulties, temperature measurements may be taken at intervals, before and following application of an RF pulse. This is precisely the approach taken to obtain the measurements shown in Figure 4-2.

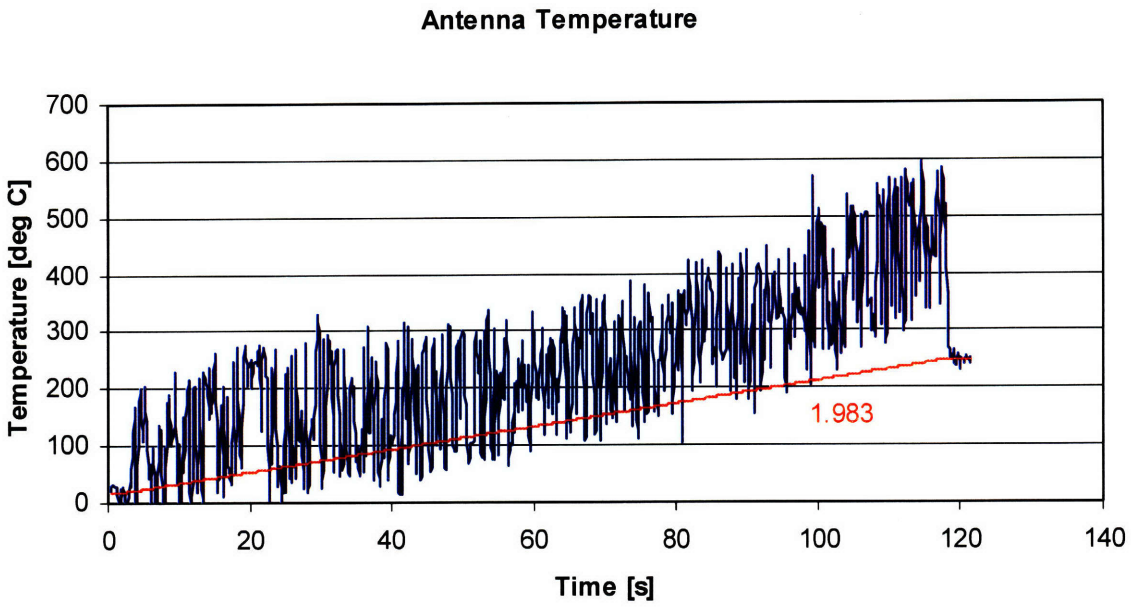

Figure 4-1: Helicon antenna temperature evolution over a two-minute run. Thermocouple is bonded directly to antenna in this experimental run. Excessive noise in the temperature signal is presumably caused by RF coupling to the thermocouple. Projected heating rate is presented in red.

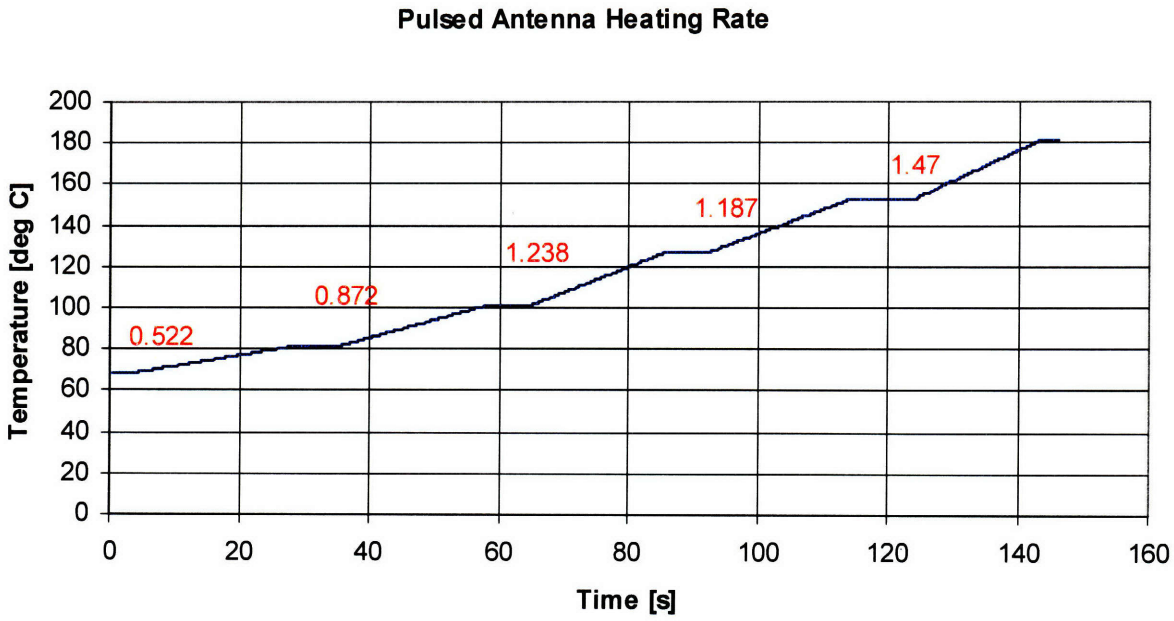

Figure 4-2: Antenna heating rate extracted from a series of points following application of an RF pulse with duration approximately 20 s. Hold times following pulses are typically less than 10 seconds. Heating rates are shown in red.

From the trend of the heating rate data gathered during this experimental run, it is clear that as the antenna becomes hotter the heating rate increases. This follows naturally from the increase in the bulk resistivity of copper with temperature. This has the unfortunate effect of complicating the direct measurement of ohmic dissipation in the antenna in particular and the RF transmission structure in general.

Based on the pulsed heating behavior shown in Figure 4-2, and the longer duration heating shown in Figure 4-1, it is reasonable to assign an average dissipation corresponding to $dT/dt \approx 2$. It is clear in the above figures that the system has not reached a steady state in which the ohmic dissipation is balanced by radiated power. Because this dissipation will increase with increasing temperature, an average heating rate of 2 K/s is thought to be reasonable, if conservative. For an antenna mass of 97 g, we obtain the power dissipation associated with the antenna, $P_{ANT} = 74.69$ W.

2.1.3 Vacuum Feed Through

Several aspects of the RF feed through design complicate direct determination of its associated heating rate. Close proximity to RF currents tend to induce a great deal of noise on the low-voltage thermal signals. The length of the feed through, approximately 0.75 m, makes measurement resolution problematic. Furthermore, the high specific heat of copper makes estimation of dissipated power strongly susceptible to minor variations in heating rate.

In order to obtain trends with any degree of confidence, therefore, it is necessary to take thermal data over much longer time scales than those typical of confinement tube or antenna heating. The data given in Figure 4-3 represents a 2-minute experimental run.

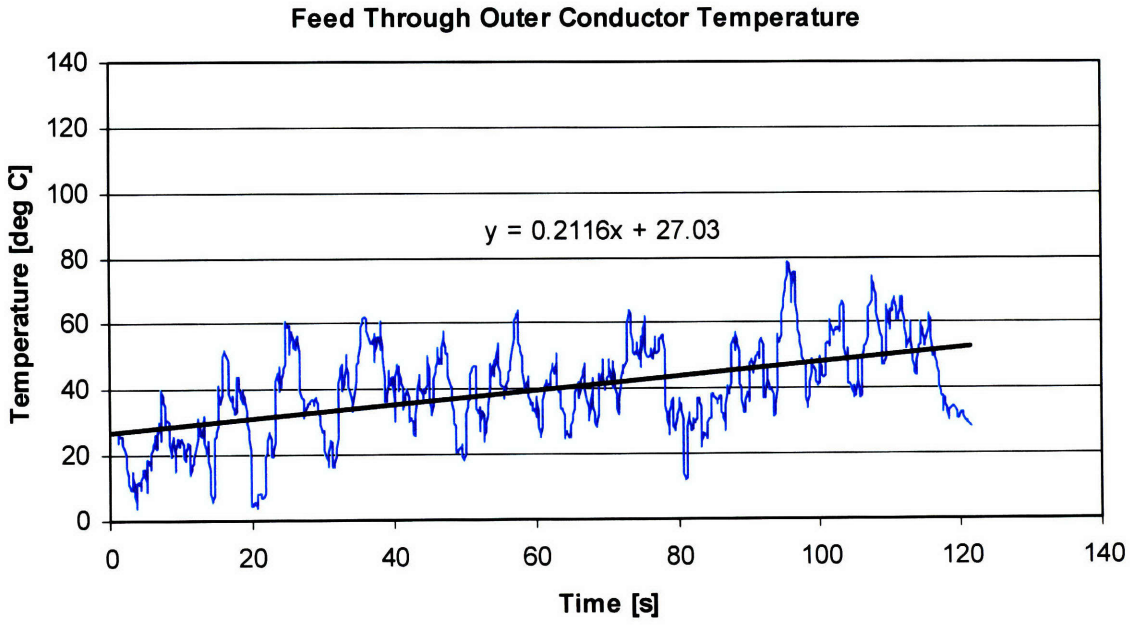

Figure 4-3: Temperature growth associated with the feed though outer conductor. These data are taken 0.5 m from the vacuum chamber RF feed through flange.

A complete analysis of the dissipation in the feed through is complicated by the presence of brazed joints and discontinuities in conductor diameter and thickness. A simplified analysis

follows, in which the feed through is assumed to be comprised of two elements, an inner conductor ¼ in. in diameter and an outer conductor ¾ in. in diameter.

We assume that the thermal conductivity of copper is sufficiently high and dissipative effects sufficiently uniform that temperature gradients along the feed through may be neglected. Using a feed through length of 0.75 m and a linear mass of 0.955 kg/m, we can compute the power dissipated in the outer conductor based on the measurements given in Figure 4-3, P_{OC} = 55.13 W.

In the absence of experimental data for the heating rate of the inner conductor, dissipative losses can be estimated by considering the difference in resistances of the inner and outer conductor in conjunction with the known dissipation on the outer conductor. For a skin depth of δ = 17.7 μm, we can use the data for copper in Table 2-1 to compute the resistance associated with a copper conductor carrying an RF signal of 13.56 MHz. For a conductor outer diameter of 1.9 cm, we find the resistance is approximately R_{OC} = 0.805 Ω/m. For an outer diameter of 0.64 cm, on the other hand, this resistance becomes R_{IC} = 2.41 Ω/m. Neglecting temperature variations in conductivity, we can therefore roughly estimate that the dissipative loss on the inner conductor will be three times that on the outer conductor.

Using this simplified analysis we obtain P_{FT} = 220.52 W.

4.2 Ionization Power

The power consumed in ionizing the propellant gas is proportional to the propellant flow rate and inversely proportional to the molar mass of the species, as discussed in Section 2.1.2. For argon, the ionization power requirement is given by P_{ION} = 1.13*F, where F is the flow rate in sccm. For our reference condition of 20 sccm Ar, the power requirement is P_{ION} = 22.6 W.

4.3 Confinement Tube Heating

As described above, the heat flux to the walls of the confinement tube was determined by measuring temperature response at various locations with respect to the magnet and antenna structure. We apply a linear fit to data taken while $T << T_{EQ}$, so that radiative effects can be neglected. This approach is illustrated in Figure 4-4, which shows temperature plots and linear fits for a typical experimental run.

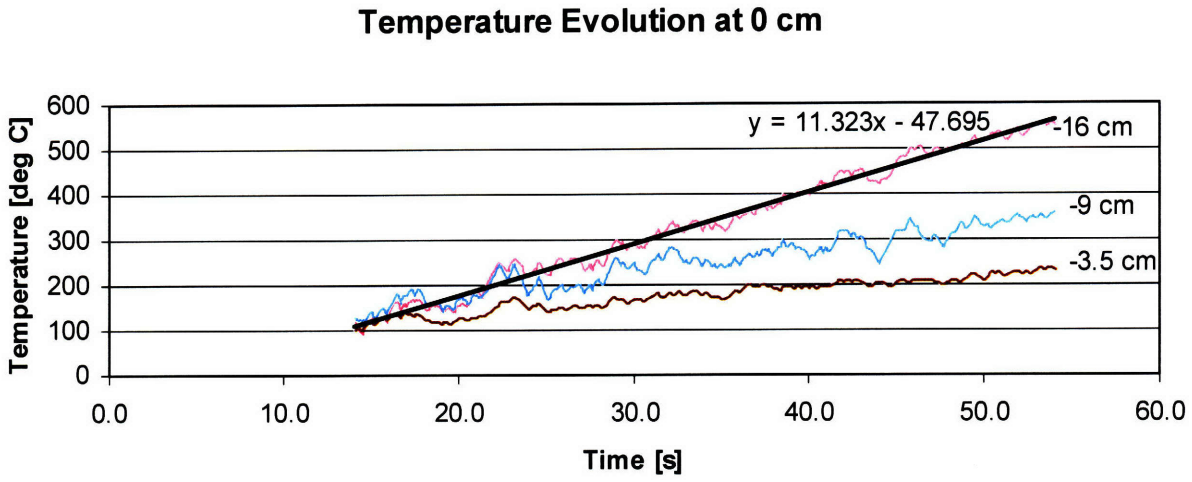

Figure 4-4: Temperature response of the neutral particle confinement tube. Operating conditions during this run are P_{FOR} = 1.19 kW in argon at 10 sccm, with field strength B = 0.2T. The slope indicated for the -16 cm position corresponds to a heat flux of 2.58 W/cm^2.

Using this methodology, it is possible to obtain the heating rate and thereby the incident heat flux along the walls of the neutral confinement tube for a variety of experimental conditions. Due to the limited number of thermocouple channels available during any given run, flux measurements at a large number of positions relative to the antenna and electromagnet can be taken by varying the position of the neutral confinement tube between runs. In this way, the location of the thermocouples, which are fixed to the neutral confinement tube, might also be varied. Figures 4-

5 through 4-8 give the heating rata data which are used to derive the flux profiles given in Figures 4-9 and 4-10.

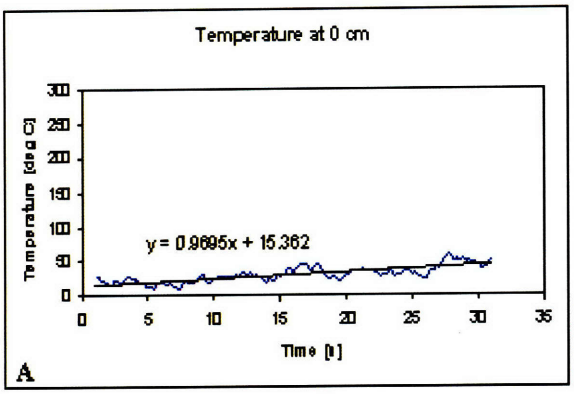
Temperature at 0 cm
Temperature [deg C]
y = 0.9695x + 15.362
Time [t]
A

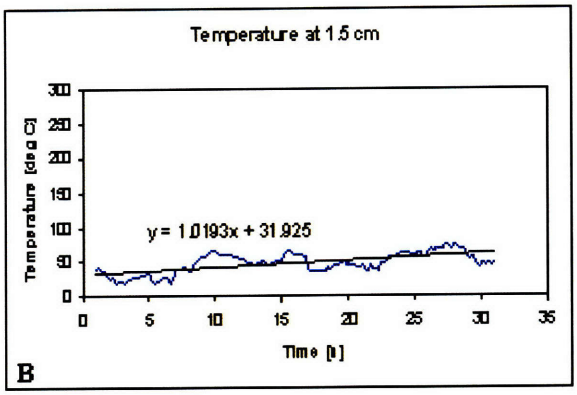
Temperature at 1.5 cm
Temperature [deg C]
y = 1.0193x + 31.925
Time [t]
B

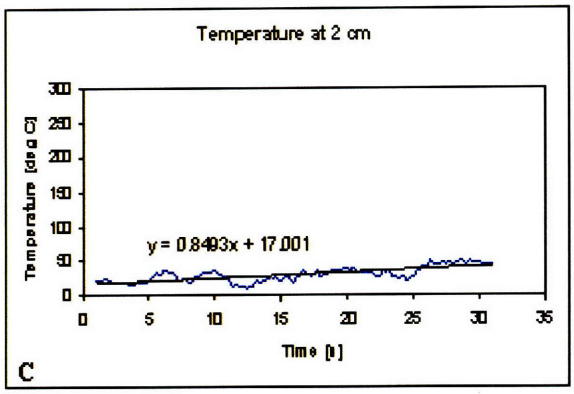
Temperature at 2 cm
Temperature [deg C]
y = 0.8493x + 17.001
Time [t]
C

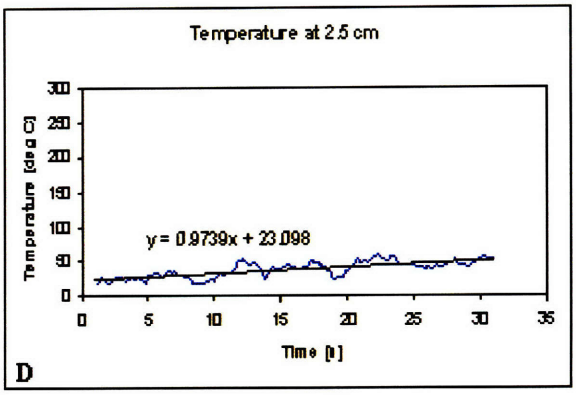
Temperature at 2.5 cm
Temperature [deg C]
y = 0.9739x + 23.098
Time [t]
D

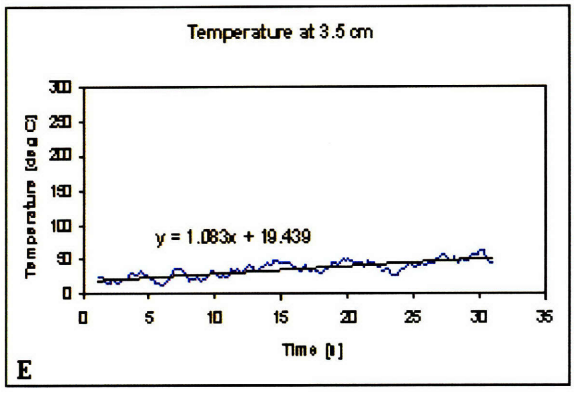
Temperature at 3.5 cm
Temperature [deg C]
y = 1.083x + 19.439
Time [t]
E

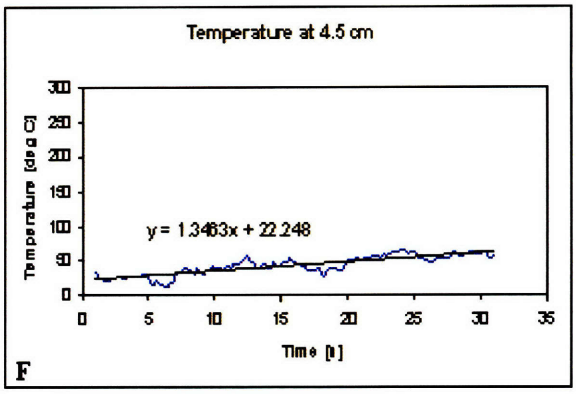
Temperature at 4.5 cm
Temperature [deg C]
y = 1.3463x + 22.248
Time [t]
F

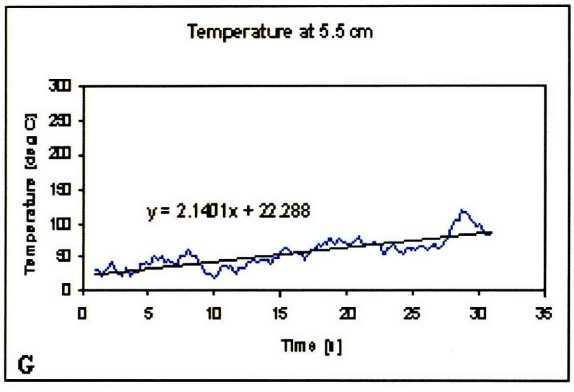
Temperature at 5.5 cm
Temperature [deg C]
y = 2.1401x + 22.288
Time [t]
G

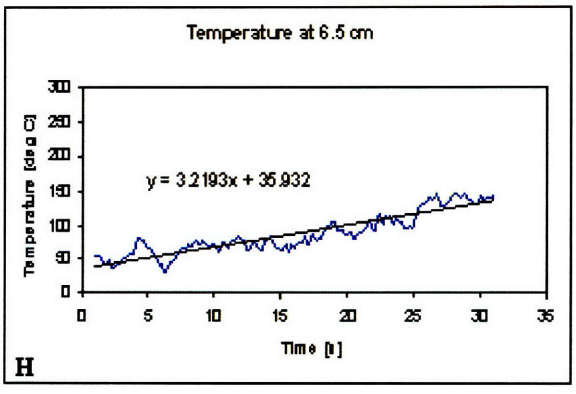
Temperature at 6.5 cm
Temperature [deg C]
y = 3.2193x + 35.932
Time [t]
H

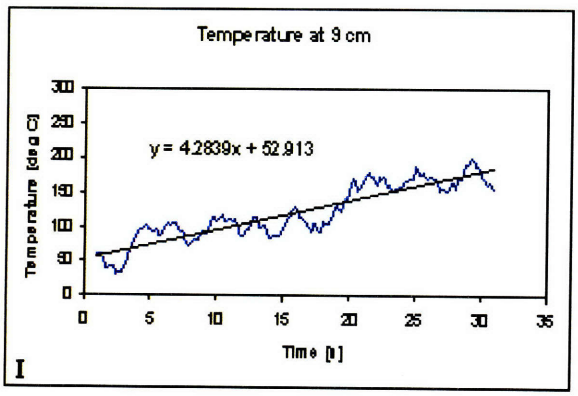
Temperature at 9 cm
y = 4.2839x + 52.913
Temperature [deg C]
Time [t]
I

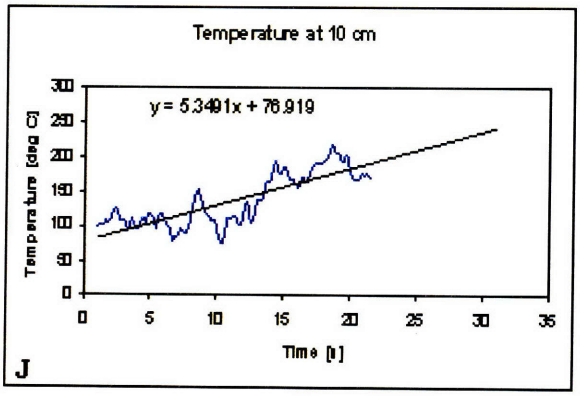
Temperature at 10 cm
y = 5.3491x + 76.919
Temperature [deg C]
Time [t]
J

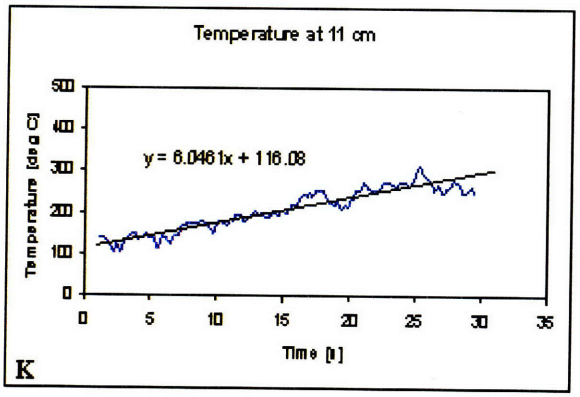
Temperature at 11 cm
y = 6.0461x + 116.08
Temperature [deg C]
Time [t]
K

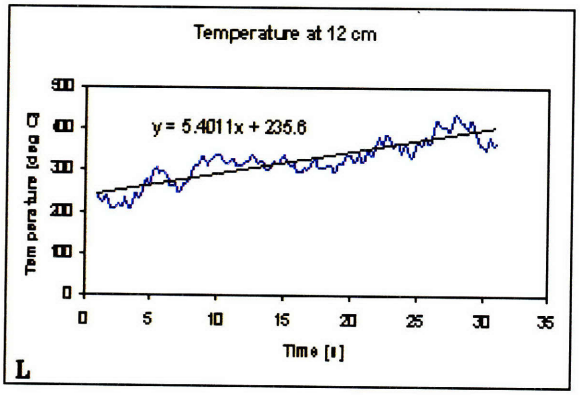
Temperature at 12 cm
y = 5.4011x + 235.6
Temperature [deg C]
Time [t]
L

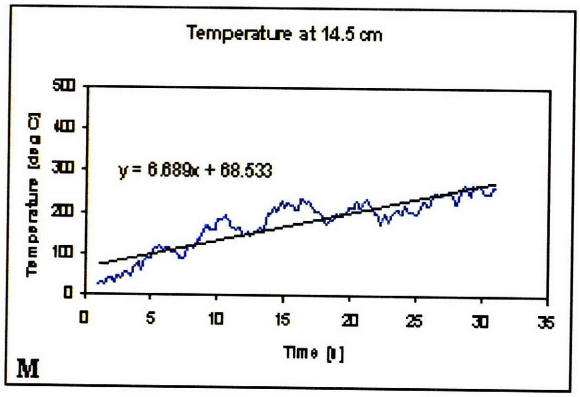
Temperature at 14.5 cm
y = 6.689x + 68.533
Temperature [deg C]
Time [t]
M

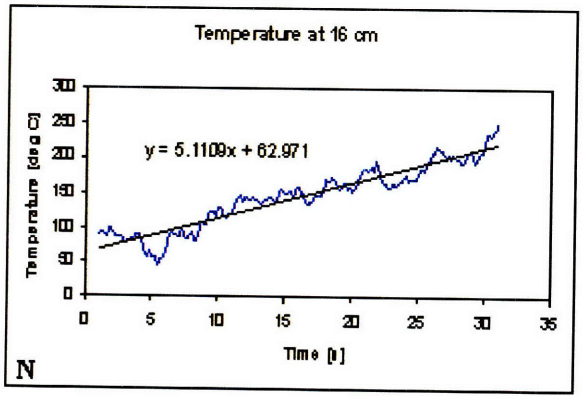
Temperature at 16 cm
y = 5.1109x + 62.971
Temperature [deg C]
Time [t]
N

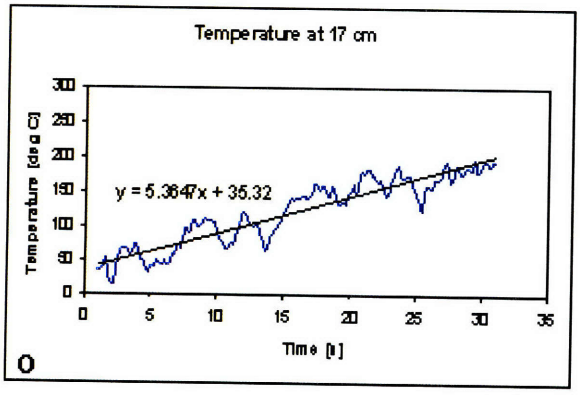
Temperature at 17 cm
y = 5.3647x + 35.32
Temperature [deg C]
Time [t]
O

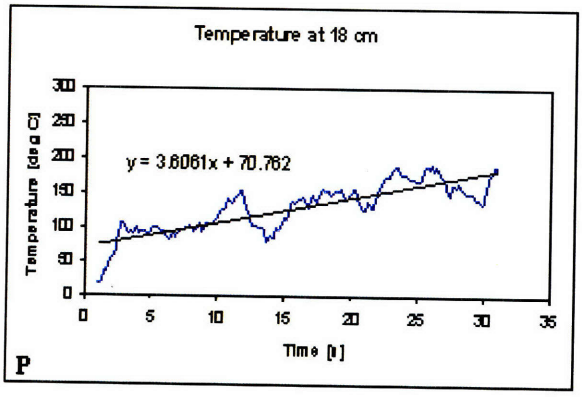
Temperature at 18 cm
y = 3.6061x + 70.762
Temperature [deg C]
Time [t]
P

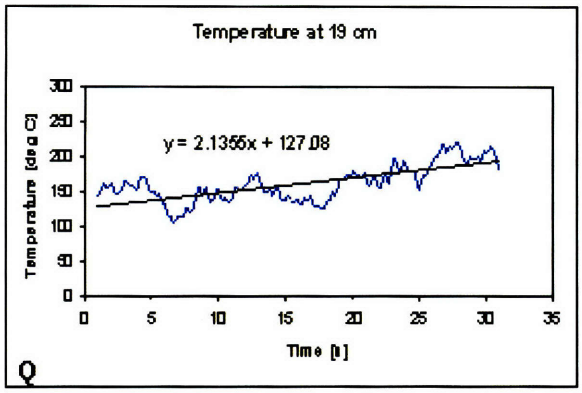

Figure 4-5: Linearized temperature plots along the length of the neutral confinement tube. All plots correspond to input power P_{RF} = 590 W, B = 0.2 T, and a flow rate of 10 sccm.

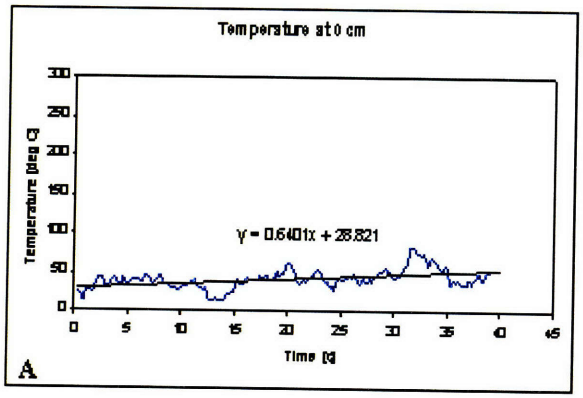
Temperature at 0 cm
Temperature [deg C]
y = 0.6401x + 28.821
Time [s]
A

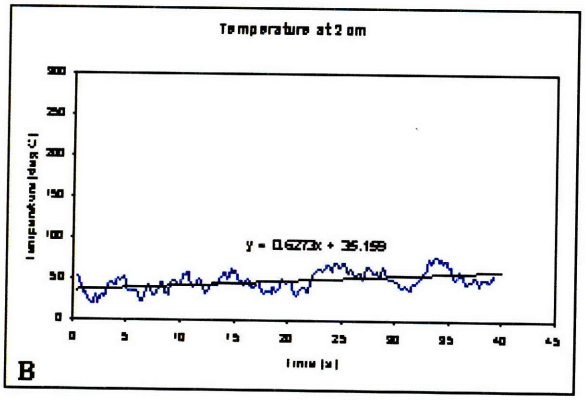
Temperature at 2 cm
y = 0.6273x + 35.159
B

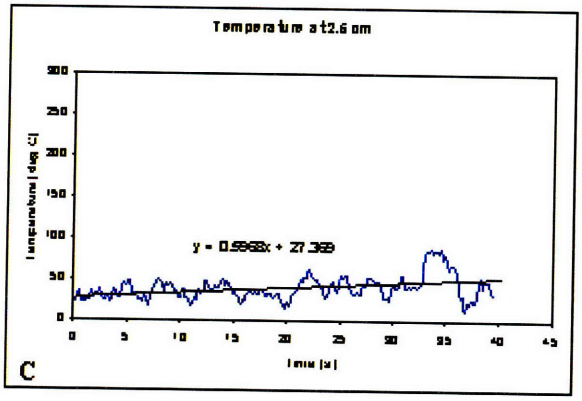
Temperature at 2.6 cm
y = 0.5968x + 27.369
C

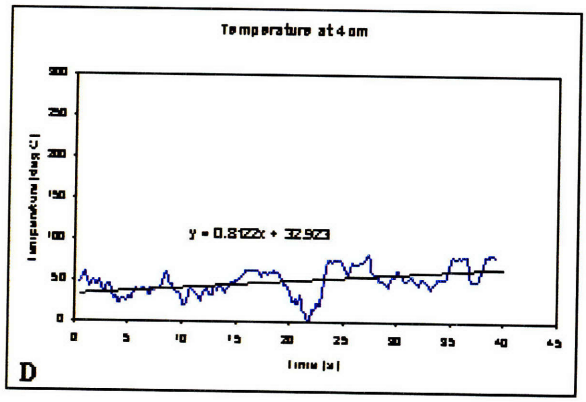
Temperature at 4 cm
y = 0.8122x + 32.923
D

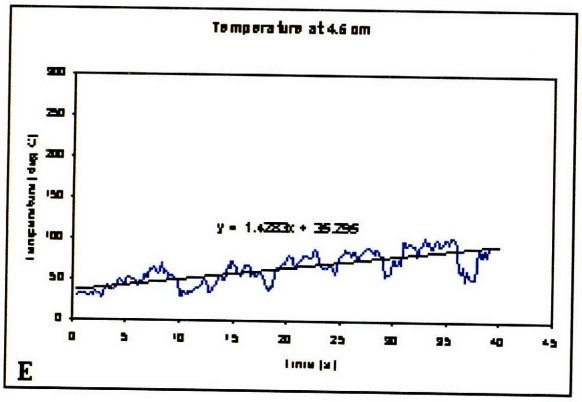
Temperature at 4.6 cm
y = 1.4283x + 35.296
E

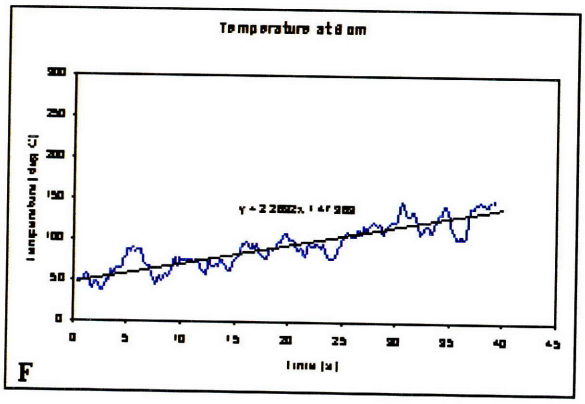
Temperature at 8 cm
F

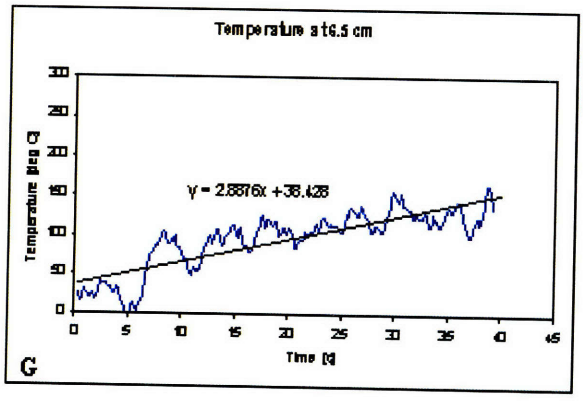
Temperature at 6.5 cm
Temperature [deg C]
y = 2.8876x + 38.428
Time [s]
G

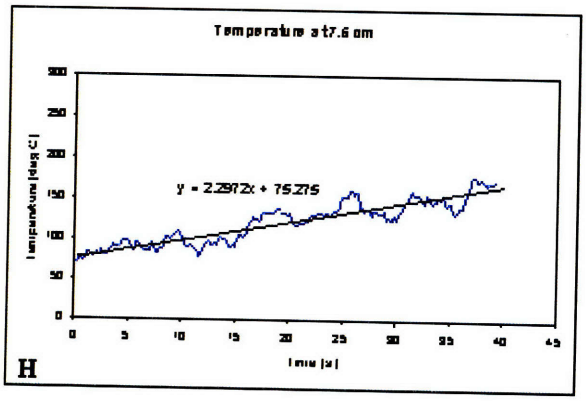
Temperature at 7.6 cm
y = 2.2972x + 75.275
H

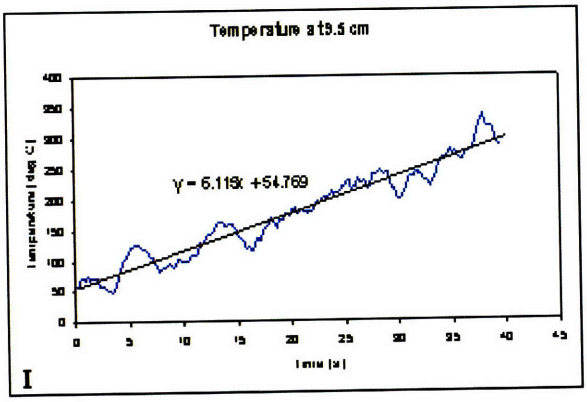
Temperature at 9.5 cm
y = 6.119x + 54.769
I

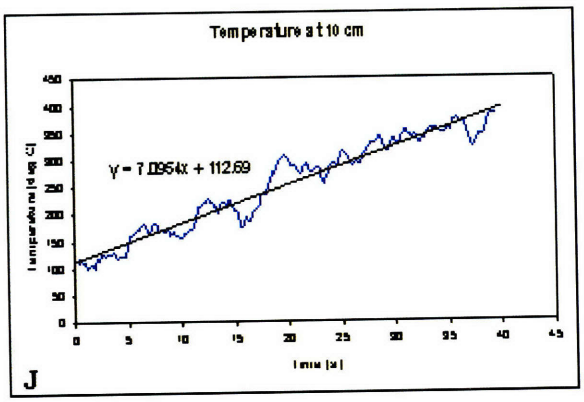
Temperature at 10 cm
y = 7.0954x + 112.69
J

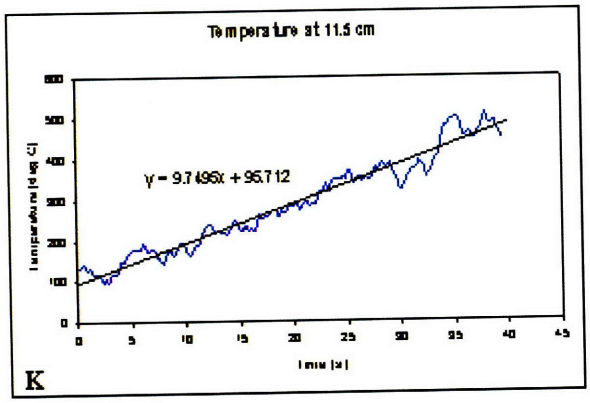
Temperature at 11.5 cm
y = 9.7496x + 95.712
K

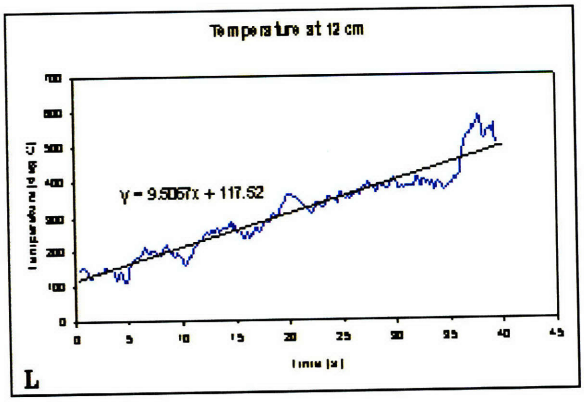
Temperature at 12 cm
y = 9.5057x + 117.52
L

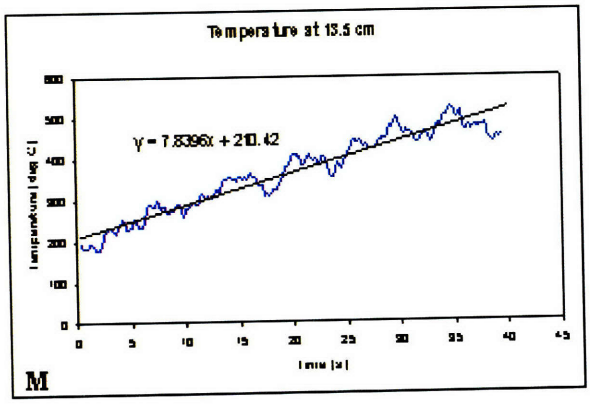
Temperature at 13.5 cm
y = 7.8396x + 210.42
M

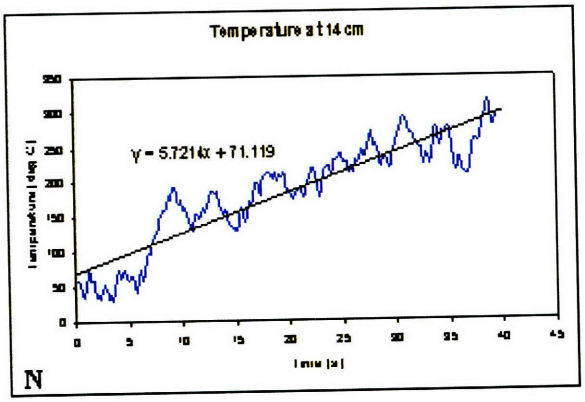
Temperature at 14 cm
y = 5.7214x + 71.119
N

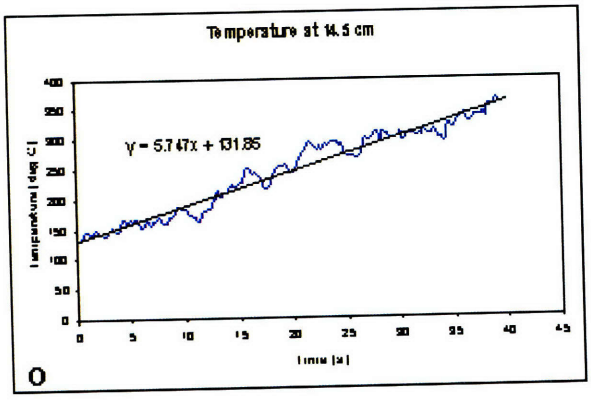
Temperature at 14.5 cm
y = 5.747x + 131.85
O

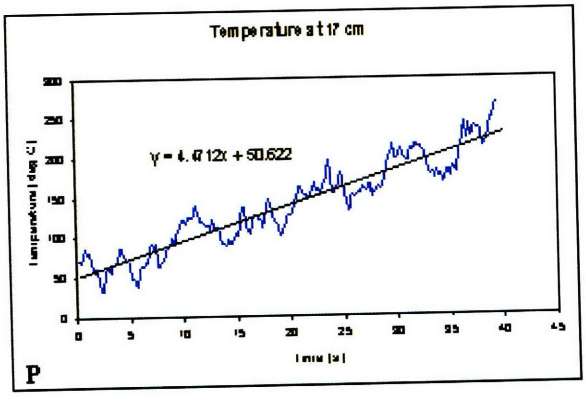
Temperature at 17 cm
y = 4.4712x + 50.622
P

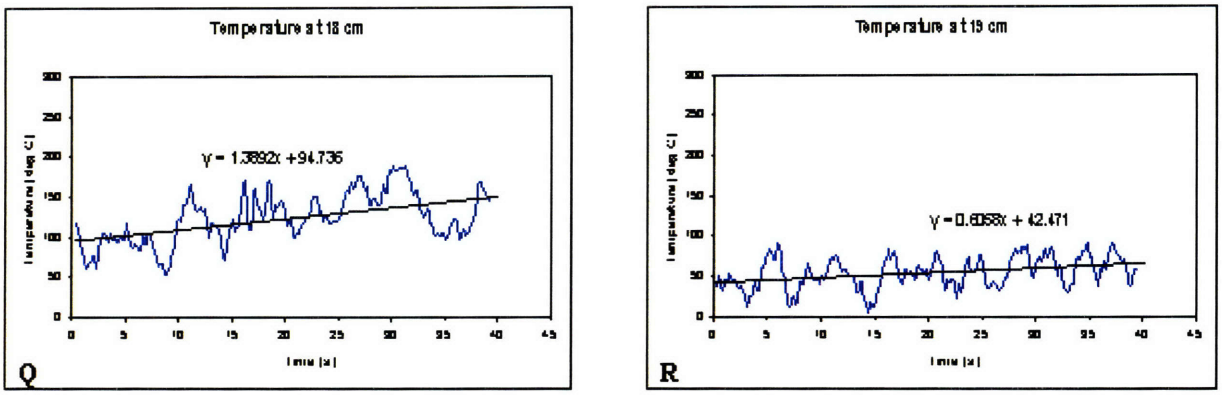

Figure 4-6: Linearized temperature plots along the length of the neutral confinement tube. All plots correspond to an input power P_{RF} = 590 W, B = 0.2 T, and a flow rate of 20 sccm.

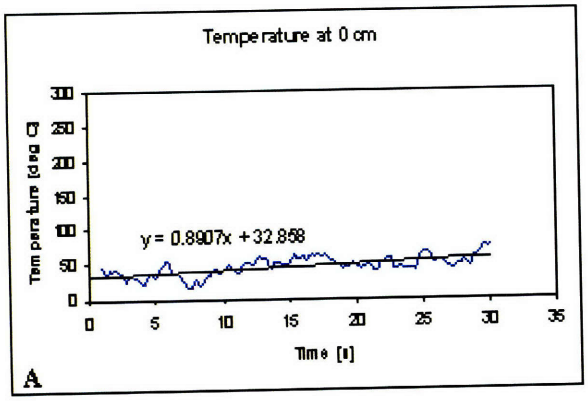
Temperature at 0 cm
y = 0.8907x + 32.858
Tem perature [deg C]
Time [t]
A

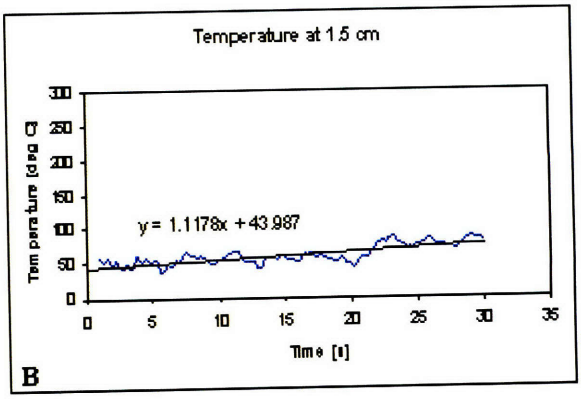
Temperature at 1.5 cm
y = 1.1178x + 43.987
Tem perature [deg C]
Time [t]
B

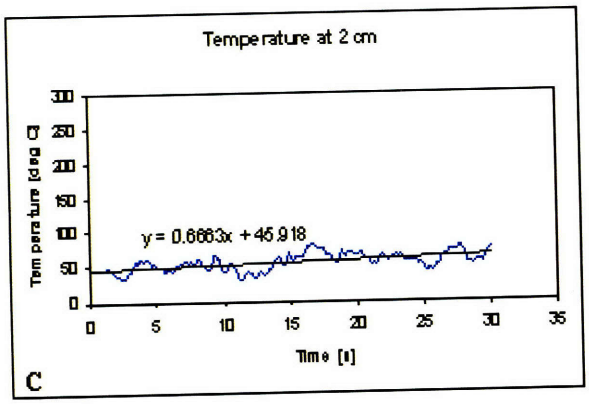
Temperature at 2 cm
y = 0.6663x + 45.918
Tem perature [deg C]
Time [t]
C

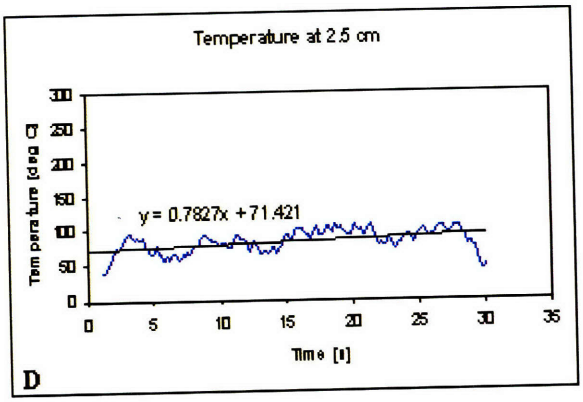
Temperature at 2.5 cm
y = 0.7827x + 71.421
Tem perature [deg C]
Time [t]
D

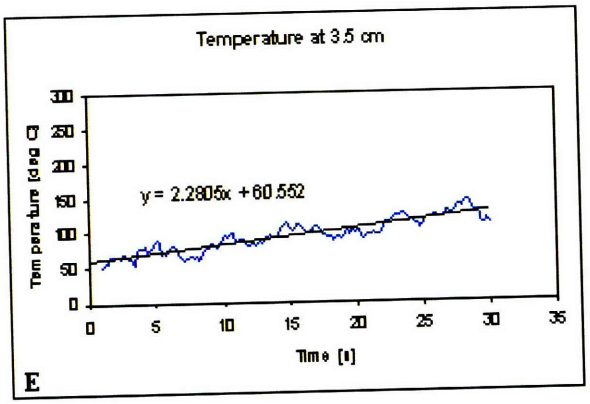
Temperature at 3.5 cm
y = 2.2805x + 60.552
Tem perature [deg C]
Time [t]
E

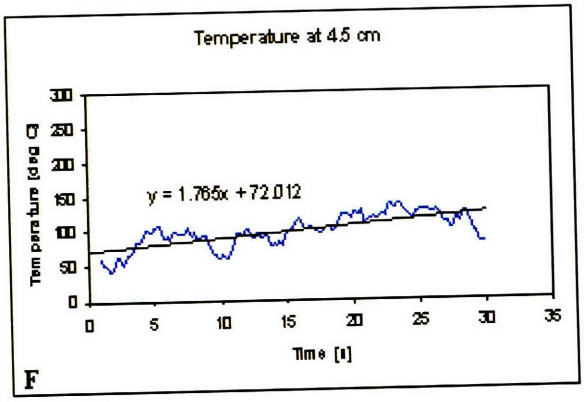
Temperature at 4.5 cm
y = 1.765x + 72.012
Tem perature [deg C]
Time [t]
F

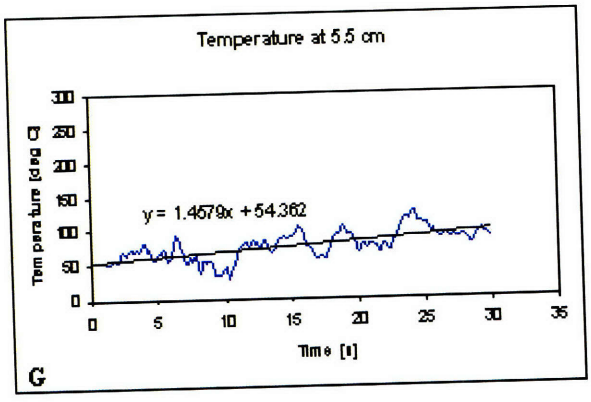
Temperature at 5.5 cm
y = 1.4579x + 54.362
Tem perature [deg C]
Time [t]
G

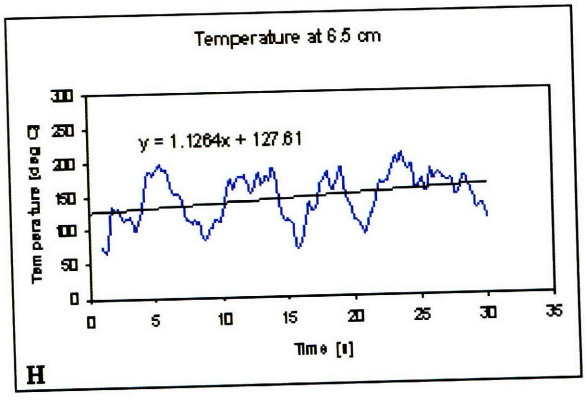
Temperature at 6.5 cm
y = 1.1264x + 127.61
Tem perature [deg C]
Time [t]
H

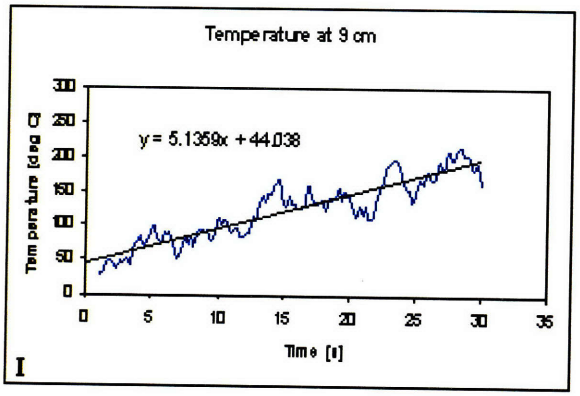
Temperature at 9 cm
y = 5.1359x + 44.038
Temperature [deg C]
Time [s]
I

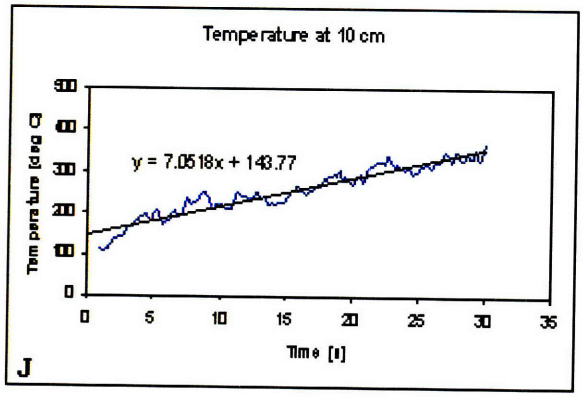
Temperature at 10 cm
y = 7.0518x + 143.77
Temperature [deg C]
Time [s]
J

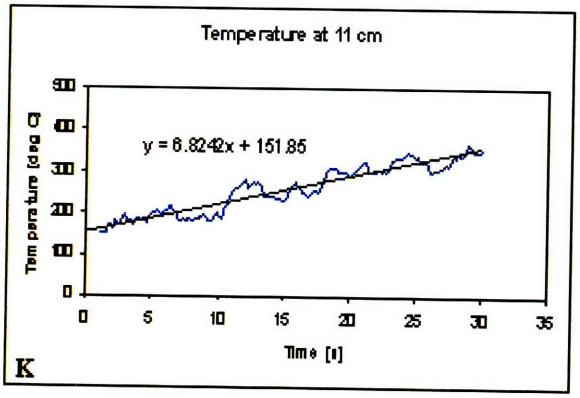
Temperature at 11 cm
y = 6.8242x + 151.85
Temperature [deg C]
Time [s]
K

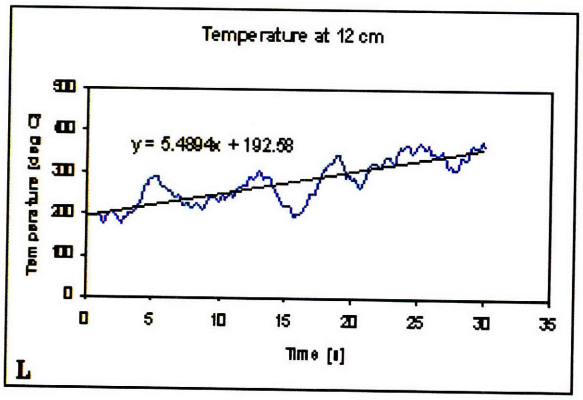
Temperature at 12 cm
y = 5.4894x + 192.58
Temperature [deg C]
Time [s]
L

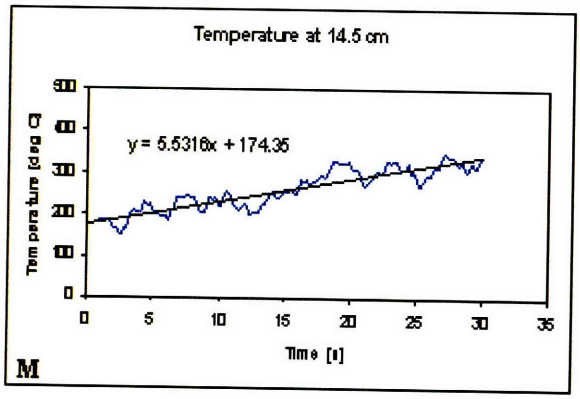
Temperature at 14.5 cm
y = 5.5316x + 174.35
Temperature [deg C]
Time [s]
M

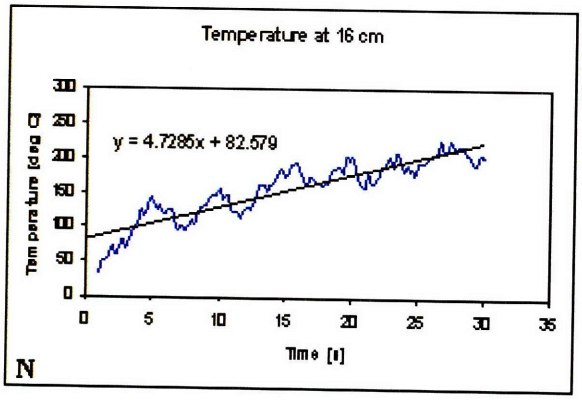
Temperature at 16 cm
y = 4.7285x + 82.579
Temperature [deg C]
Time [s]
N

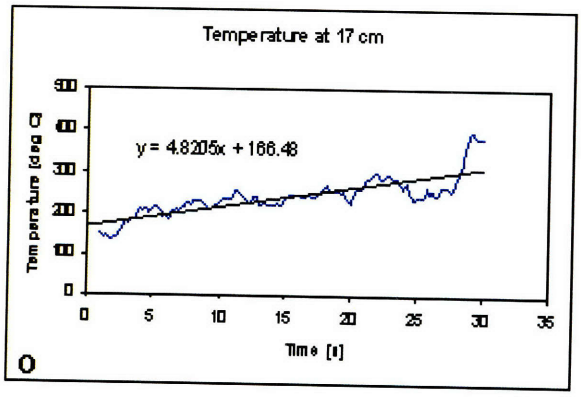
Temperature at 17 cm
y = 4.8205x + 166.48
Temperature [deg C]
Time [s]
O

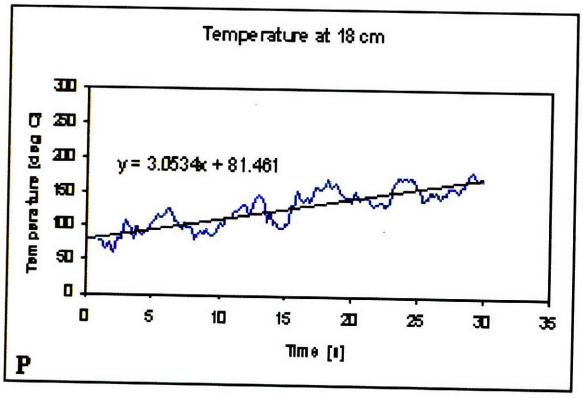
Temperature at 18 cm
y = 3.0534x + 81.461
Temperature [deg C]
Time [s]
P

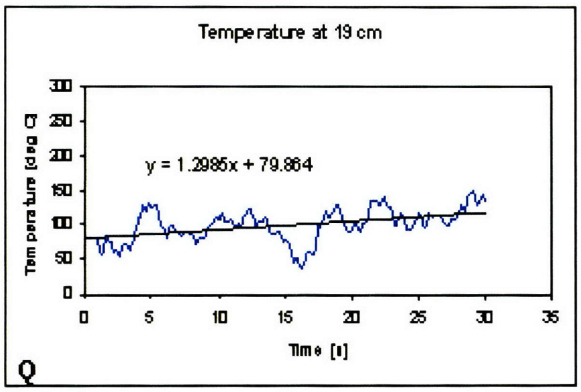

Figure 4-7: Linearized temperature plots along the length of the neutral confinement tube. All plots correspond to an input power P_{RF} = 590 W, B = 0.2 T, and a flow rate of 40 sccm.

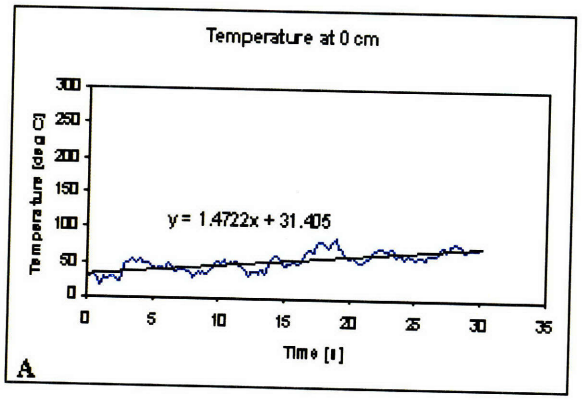
Temperature at 0 cm
Temperature [deg C]
y = 1.4722x + 31.405
Time [t]
A

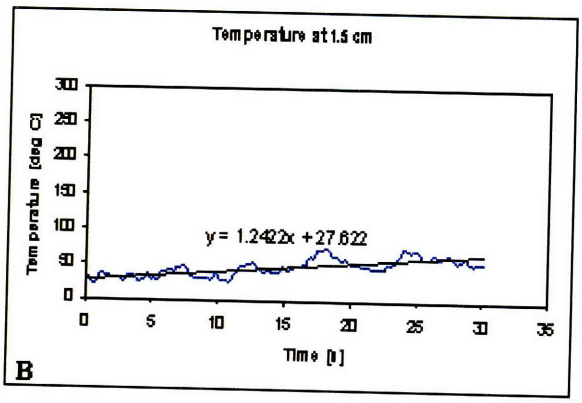
Temperature at 1.5 cm
Temperature [deg C]
y = 1.2422x + 27.622
Time [t]
B

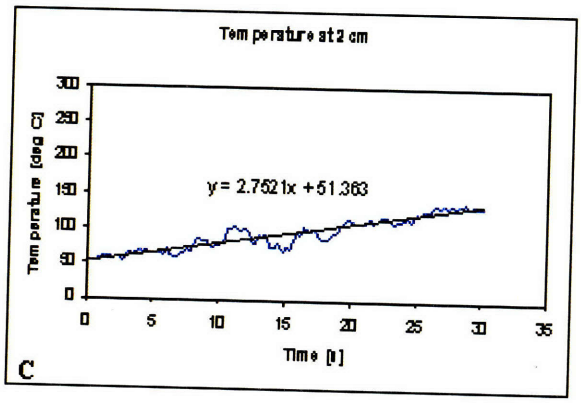
Temperature at 2 cm
Temperature [deg C]
y = 2.7521x + 51.363
Time [t]
C

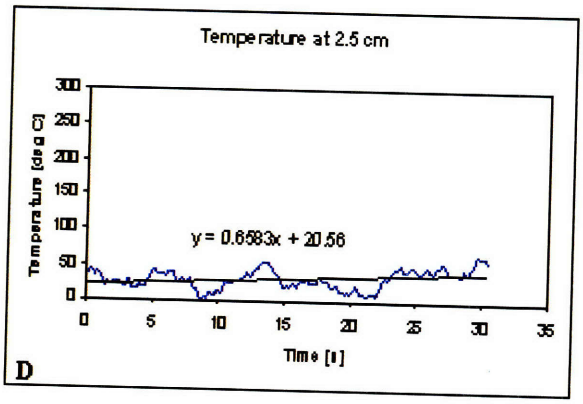
Temperature at 2.5 cm
Temperature [deg C]
y = 0.6583x + 20.56
Time [t]
D

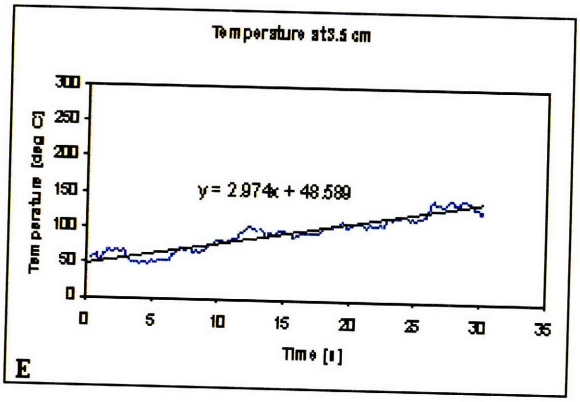
Temperature at 3.5 cm
Temperature [deg C]
y = 2.974x + 48.589
Time [t]
E

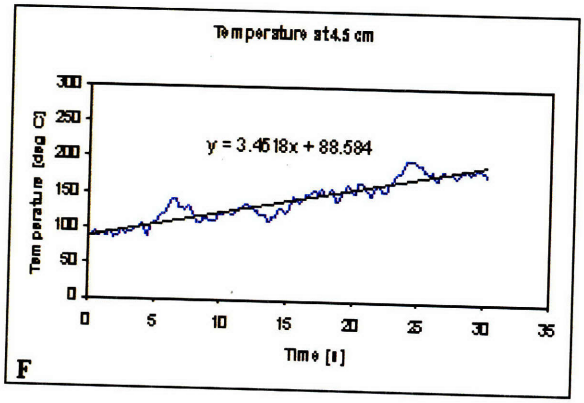
Temperature at 4.5 cm
Temperature [deg C]
y = 3.4518x + 88.584
Time [t]
F

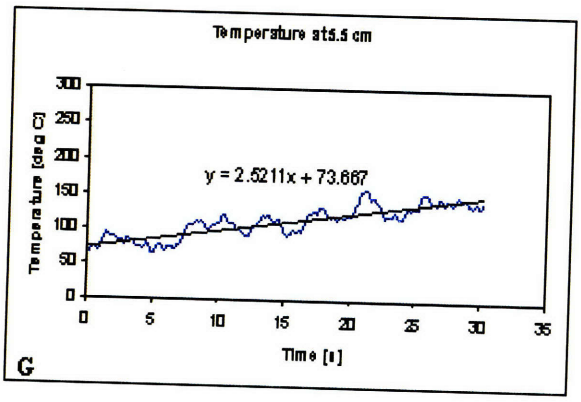
Temperature at 5.5 cm
Temperature [deg C]
y = 2.5211x + 73.667
Time [t]
G

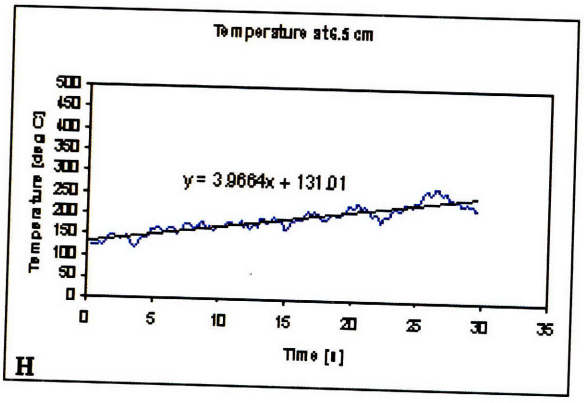
Temperature at 6.5 cm
Temperature [deg C]
y = 3.9664x + 131.01
Time [t]
H

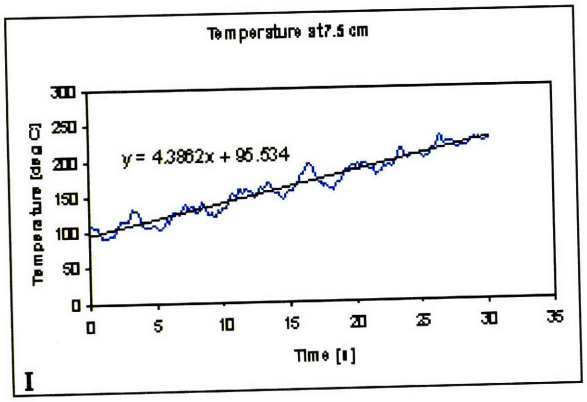
Temperature at7.5 cm
y = 4.3862x + 95.534
Temperature [deg C]
Time [t]
I

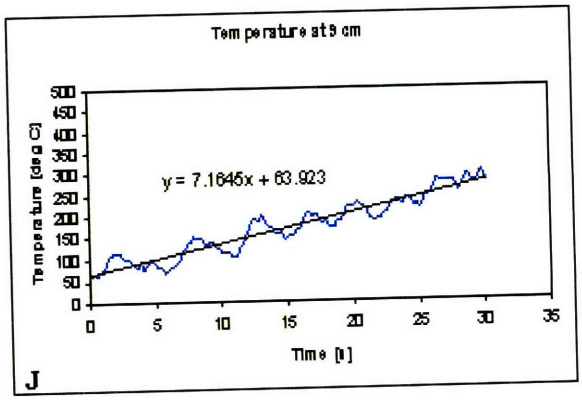
Temperature at9 cm
y = 7.1645x + 63.923
Temperature [deg C]
Time [t]
J

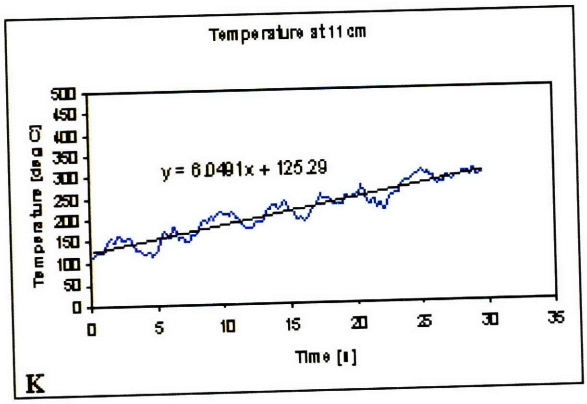
Temperature at11 cm
y = 6.0491x + 125.29
Temperature [deg C]
Time [t]
K

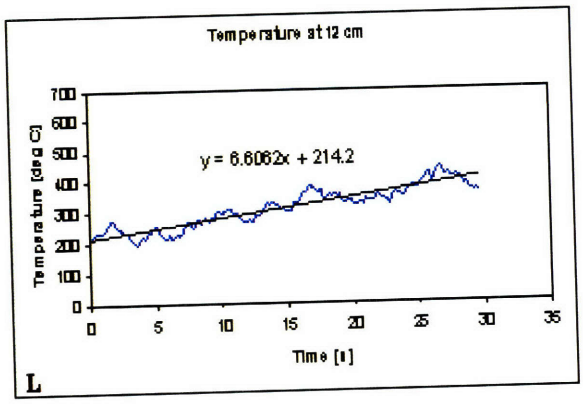
Temperature at12 cm
y = 6.6062x + 214.2
Temperature [deg C]
Time [t]
L

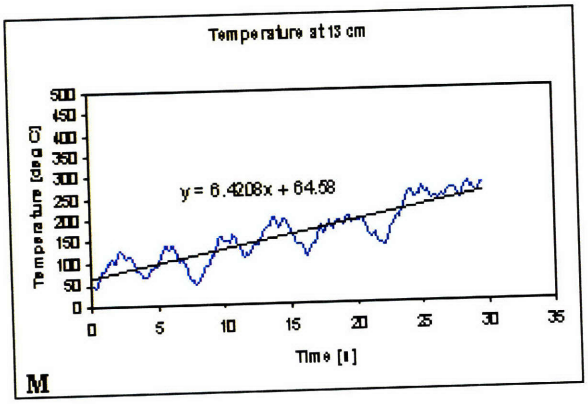
Temperature at13 cm
y = 6.4208x + 64.58
Temperature [deg C]
Time [t]
M

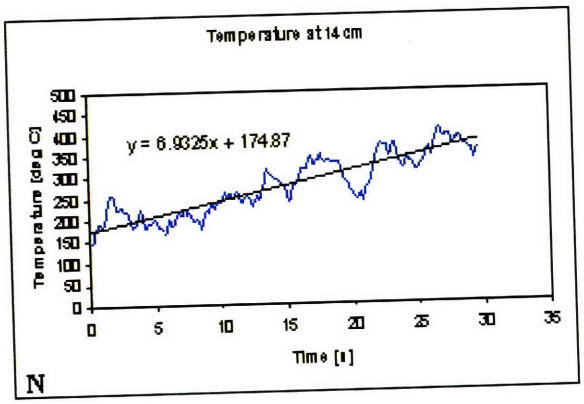
Temperature at14 cm
y = 6.9325x + 174.87
Temperature [deg C]
Time [t]
N

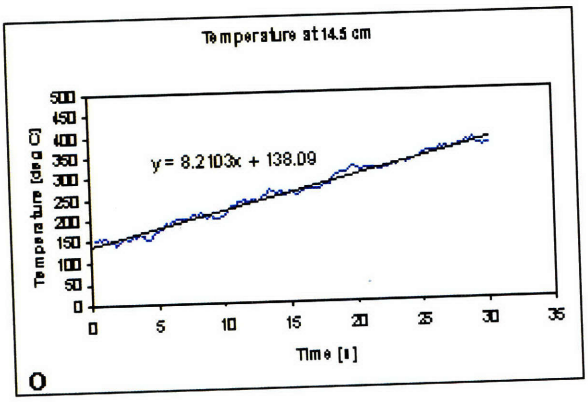
Temperature at14.5 cm
y = 8.2103x + 138.09
Temperature [deg C]
Time [t]
O

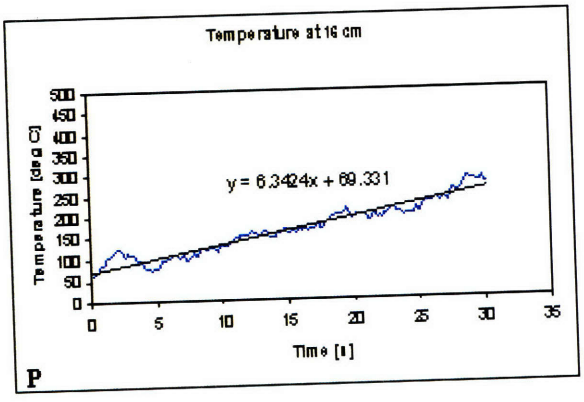
Temperature at16 cm
y = 6.3424x + 69.331
Temperature [deg C]
Time [t]
P

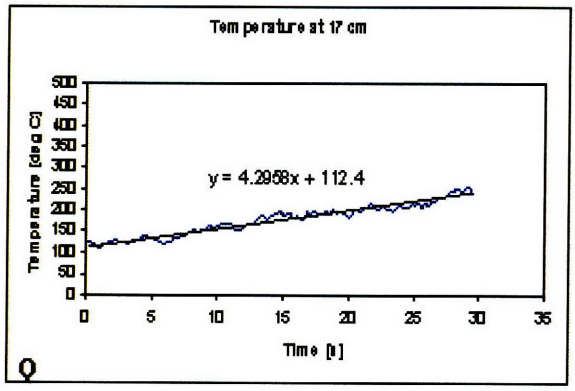

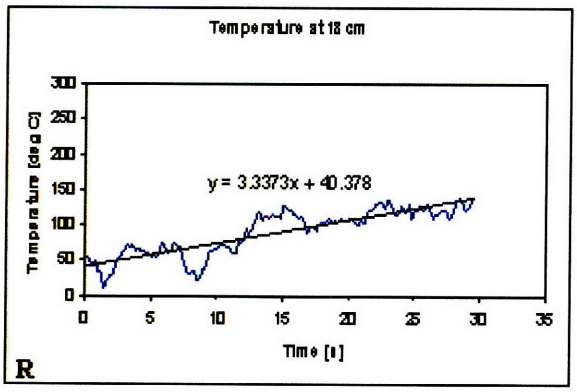

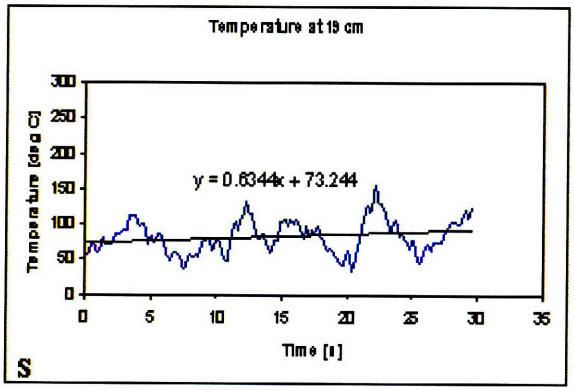

Figure 4-8: Linearized temperature plots along the length of the neutral confinement tube. All plots correspond to an input power P_{RF} = 590 W, B = 0.09 T, and a flow rate of 20 sccm.

Using these slopes we can derive the energy flux to the neutral confinement tube using exactly the method outlined in Sections 3.1 and 3.3. Following this approach, we obtain the curves given in Figures 4-9 through 4-10 below. In considering these figures it is important to note that the plume-side electromagnetic face corresponds to x = 0 cm. Propellant is injected upstream at x = 40 cm, travels in the $-\bar{e}_x$ direction, and is exhausted at x = 0 cm.

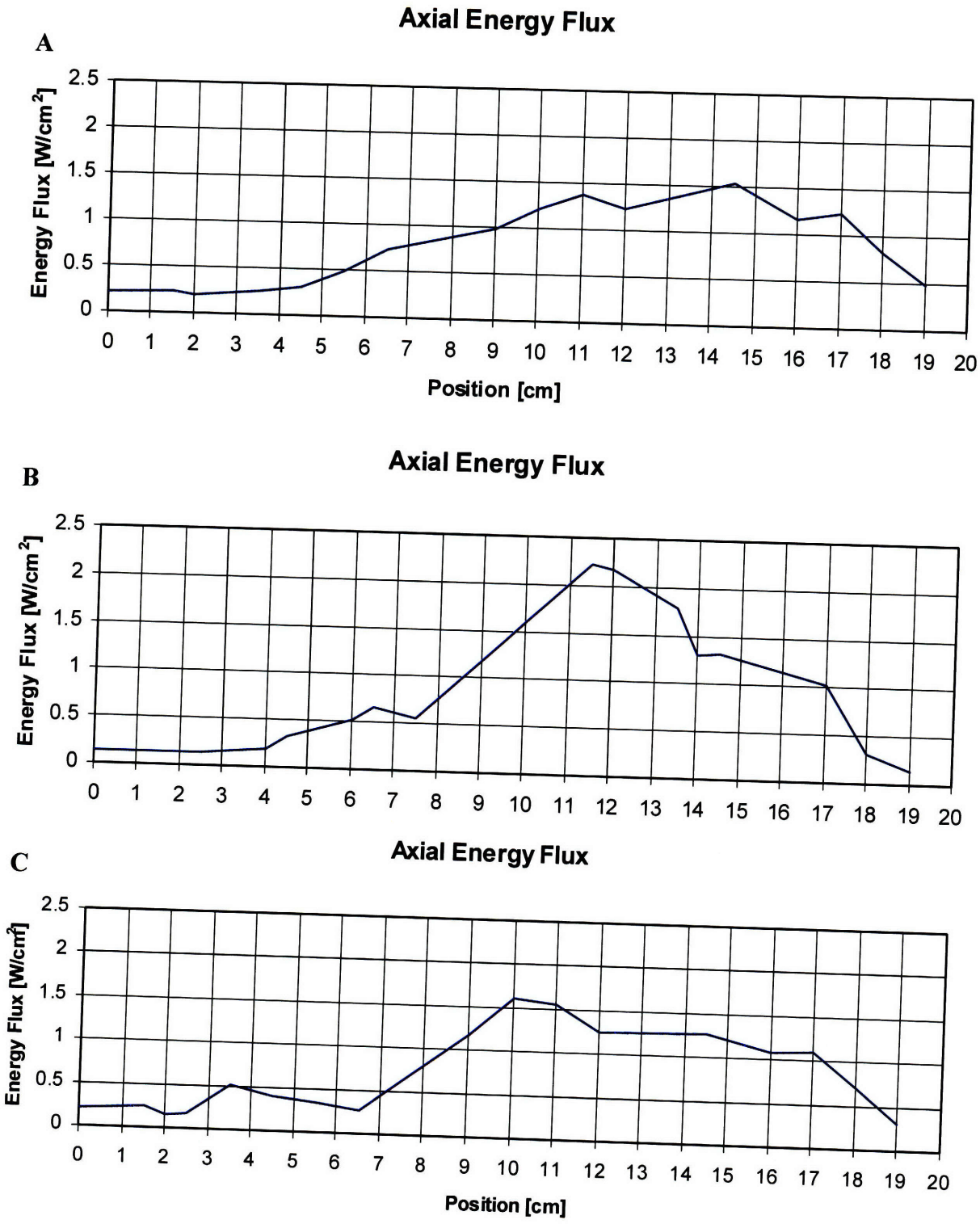

Figure 4-9: Heat flux to the walls of the neutral particle confinement tube. Operating conditions are P_{FOR} = 0.59 kW in argon at (A) 10 sccm, (B) 20 sccm, and (C) 40 sccm with field strength B = 0.2T.

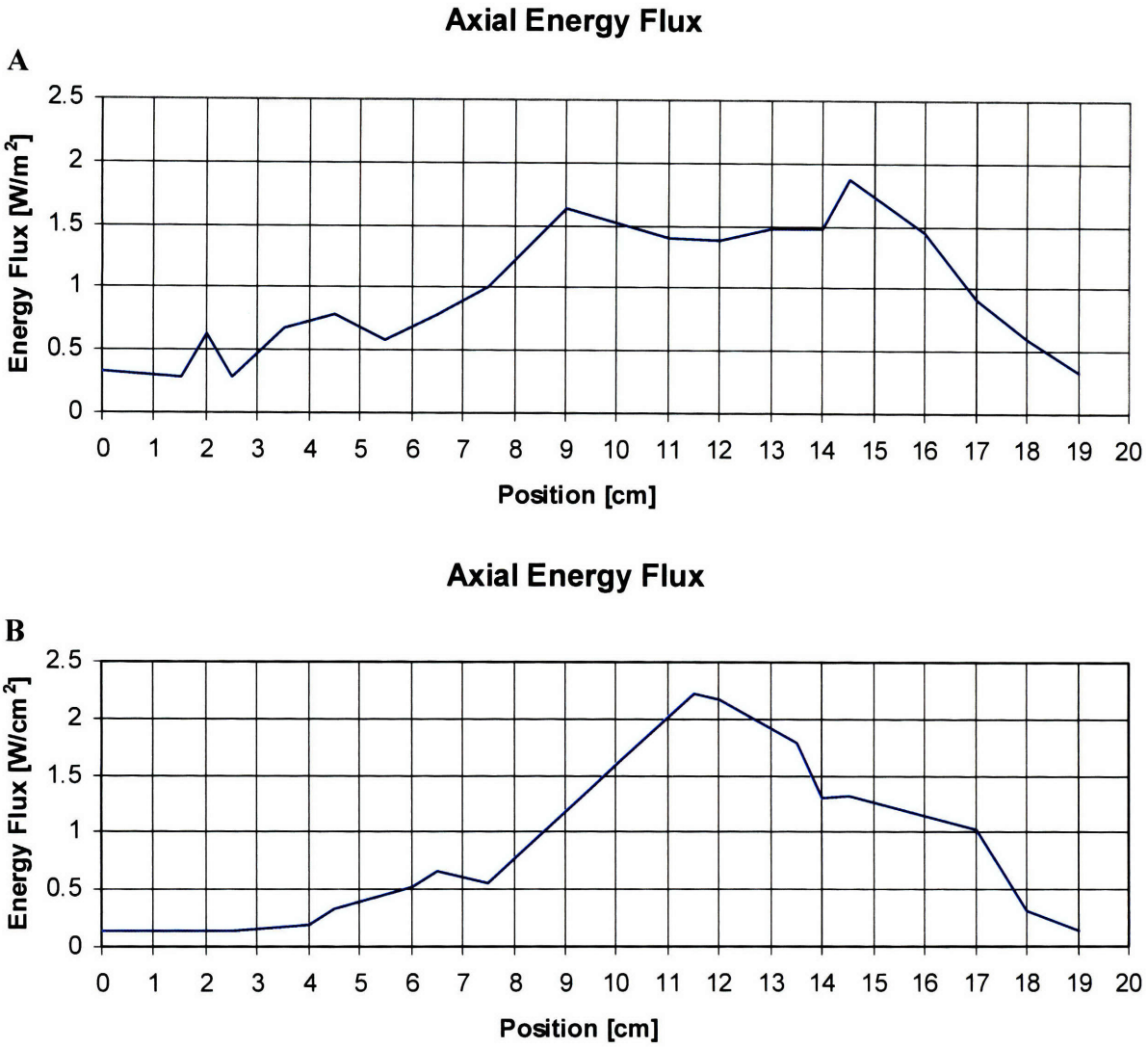

Figure 4-10: Thermal response of the neutral particle confinement tube. Operating conditions during this run are P_{FOR} = 0.59 kW in argon 20 sccm, with (A) B = 0.09T, and (B) B = 0.2T.

By evaluating the area under the curves of axial energy flux, we can obtain the integral heat flux incident to the inner surface of the neutral confinement tube. For the test case of 0.2T magnetic field and flow of 20 sccm argon, this corresponds to P_{TUBE} = 120 W.

It is useful to consider the effect of magnetic field geometry relative to the neutral confinement tube on the flux profiles given in the figures above. The axial magnetic field strength for the magnet is given in Figure 4-11 for different values of coil current.

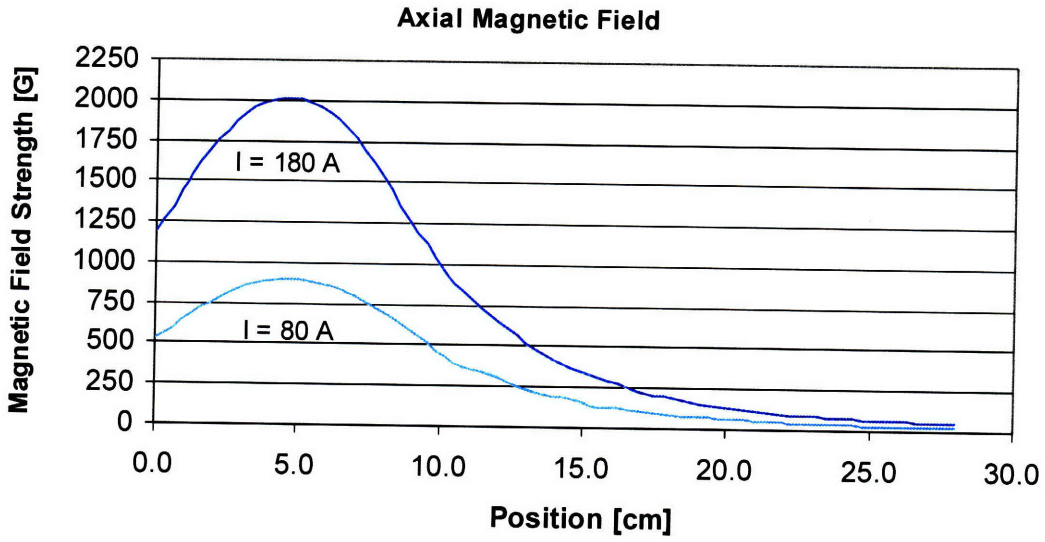

Figure 4-11: Axial magnetic field strength for the electromagnet assembly associated with the mHTX. Note that, as in the figures for axial heat flux, the plume-side electromagnetic face corresponds to x = 0 cm. Propellant is injected upstream at x = 40 cm, travels in the $-\bar{e}_x$ direction, and is exhausted at x = 0 cm.

It is clear by considering these figures that the downstream region with higher magnetic field experiences much more effective radial plasma confinement. This is reflected in the substantially reduced confinement tube heating rate measured in all cases.

4.4 Plume Power

Using thrust data taken on the mHTX experiment in a previous study [31] and provided in Figure 2-5, we can obtain the thrust for the standard flow of 20 sccm of argon, or 0.55 mg/s, used in our test case. This corresponds to a thrust of approximately 8.5 mN. Plugging into Equation 2-7, we find the plume power is approximately $P_{PLUME} = 65$ W.

4.5 RF Flux Measurements

In order to measure the uncoupled RF flux inside the chamber during operation of the thruster, the RF flux meter was placed inside the chamber. Because the device is not suitable for operation under vacuum, the helicon antenna was driven under atmospheric conditions to quantify the power radiated from the antenna. During this analog run, a maximum sustained forward power of 400 W was achieved, in which an RF flux of approximately 160 $\mu W/cm^2$ was obtained. We can obtain an upper bound on the RF deposition along the tank wall by assuming that the measured RF is isotropic, and all the energy is absorbed by the tank wall. We can model the vacuum chamber as a perfect cylinder with diameter 1.5 m and length 1.6 m. In this case, substituting into Equation 2-8 we obtain:

$$P_{RF_{OUT}} = \left(2\pi rL + 2\pi r^2\right)\phi_{RF}. \tag{4-4}$$

Solving with the appropriate values, we obtain $P_{RF_{OUT}} = 18.05$ W.

Chapter 5

Conclusion

In this section the observations from the previous chapter are applied to the power balance, outlined in Chapter 2. An accounting of all the losses and outputs associated with the system is completed and the overall system efficiency is computed. Avenues are identified for improving overall efficiency. Recommendations are offered for future work.

5.1 Power Balance Tabulation

A final accounting of the output and loss mechanisms associated with the mHTX experiment is included in Table 5-1 below. Of the 590 W of forward power consistently applied across experimental runs, approximately 572 W have been accounted for. This represents about 97% of the total power.

Power Blance for mHTX@mit		
P_{COAX}	51.33	W
P_{FT}	220.52	W
P_{ANT}	74.69	W
P_{ION}	22.60	W
P_{TUBE}	120.00	W
P_{PLUME}	65.00	W
P_{RFOUT}	18.05	W
P_{TOT}	572.19	W
P_{RFIN}	590.00	W

Table 5-1: Tabulated power for the mHTX experiment.

5.2 Improving Performance

In its current configuration, the helicon thruster operates at approximatly 11% efficiency. From the tabulation in Table 5-1, it is immediately clear that the majority of losses are ohmic transmission losses. To some degree, these are particular to the experimental setup in the SPL and are not representative of losses likely to be encountered with a working thruster. In a typical spacecraft, RF transmission losses, for example, might be expected to be much lower, as the conversion from RF to DC power will take place in relatively close proximity to the use point.

It is clear from the data presented in Figures 4-9 and 4-10 that the majority of energy flux in the neutral particle confinement tube occurs under the antenna, between x = 7 cm and x = 17 cm. It is possible that variation in the magnetic field geometry may produce a more favorable axial potential distribution that might reduce these losses. It may be advantageous, therefore to study the role of magnetic field geometry and strength under the antenna in radial particle and energy transport in this region.

5.3 Recommendations for Future Work

Future work on the helicon thruster in general and the power balance in particular should first focus on reducing losses associated with power transmission hardware. This might be accomplished in a variety of ways: by reducing operating frequency; increasing conductor surface area; and reducing the source-to-sink distance associated with the experiment.

Second, there is a need for a more precise measurement of the power dissipated in the RF feed through. Losses computed from heating rates in this study indicate that power dissipation in the feed through may consume over one-third of the power applied to the system. Further studies with more spatial precision should be undertaken to further characterize this loss path. Additional measurements for losses in the RF impedance matching network will also be beneficial.

Third, measurements of radiation at transmitted wavelengths should be taken using a bolometer to quantify this loss.

Finally, concurrently with the previous recommendation, the mHTX experiment should migrate to the use of permanent magnets for generation of the magnetic field. Several commercially available options exist for permanent magnets, especially rare earth magnets such as Neodymium-Iron-Boron (NdFeB), which can provide comparable or greater fields, which may be more easily manipulated in experiments, for a small fraction of the mass required by electromagnets.

Appendix A

Helicon Thruster Control Software

Experimental hardware for the mHTX experiment is controlled and monitored by a set of virtual instruments (VIs) in a LABVIEW environment. Three VIs are used to control and monitor the RF power supply, low voltage power supply for magnetic field generation, and flow controller. The RF power supply VI, shown in Figures A-1 and A-2, allows the user to establish power set point, and returns the instantaneous forward, reflected and net power delivered by the power supply. Matching network impedance and VSWR are also displayed. Magnet current (Figure A-3 and A-4) set point is user selectable and shown in real time. Rate of change of magnet current is limited by a user selectable ramp rate. Propellant gas flow rate, shown in Figure A-5 and A-6, is user selectable, and instantaneous propellant flow rate is returned. A user selectable propellant gas correction factor is also displayed.

The data acquisition program for gathering the temperature data presented in this work is shown in Figure A-7 and A-8. Due to the number of feed through ports, the maximum number of thermocouple signals that could be monitored simultaneously was limited to five. Temperature is measured and stored at 5 Hz. Numerical temperature values are shown for each channel, as well as graphical temperature history. Maximum and minimum temperatures are

user selectable and set the y-axis temperature range. A variety of junction types can be selected, including K-type used in this study. The temperature of the cold junction is user defined. This is typically set to the standard temperature, 25˚C.

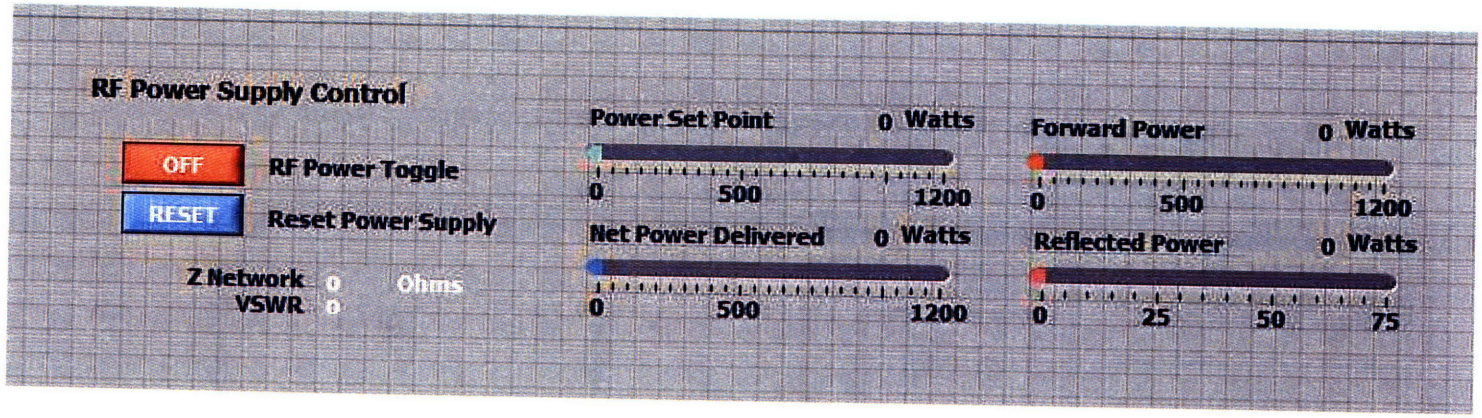

Figure A-1: RF power supply control VI. This graphical user interface (GUI) is used to control the RFPP RF-10S/PWT 1.2 kW 13.56 MHz power supply.

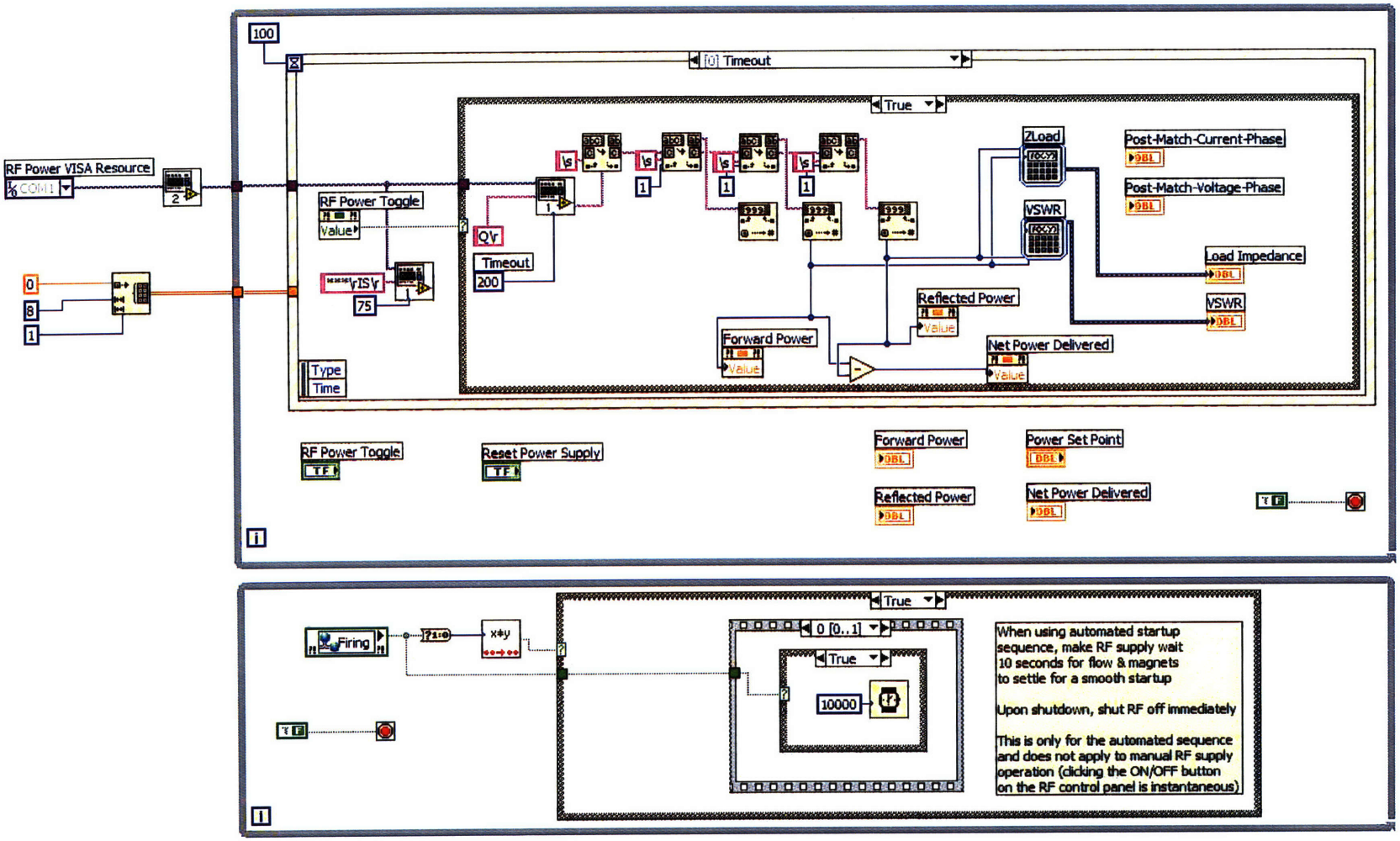

Figure A-2: Block diagram illustrating the control logic for the RFPS GUI.

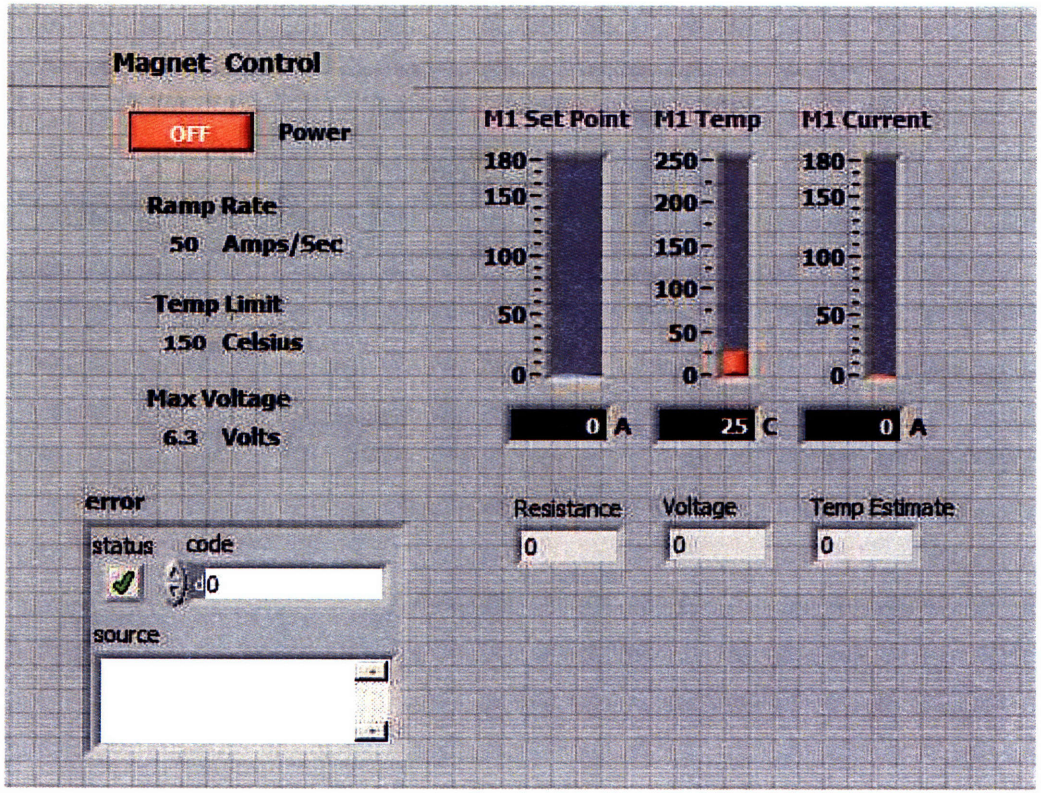

Figure A-3: Magnet control VI. This GUI is used to control the Agilent N5761A 6V 180A 1080W power supply supplying the magnetic field for the mHTX.

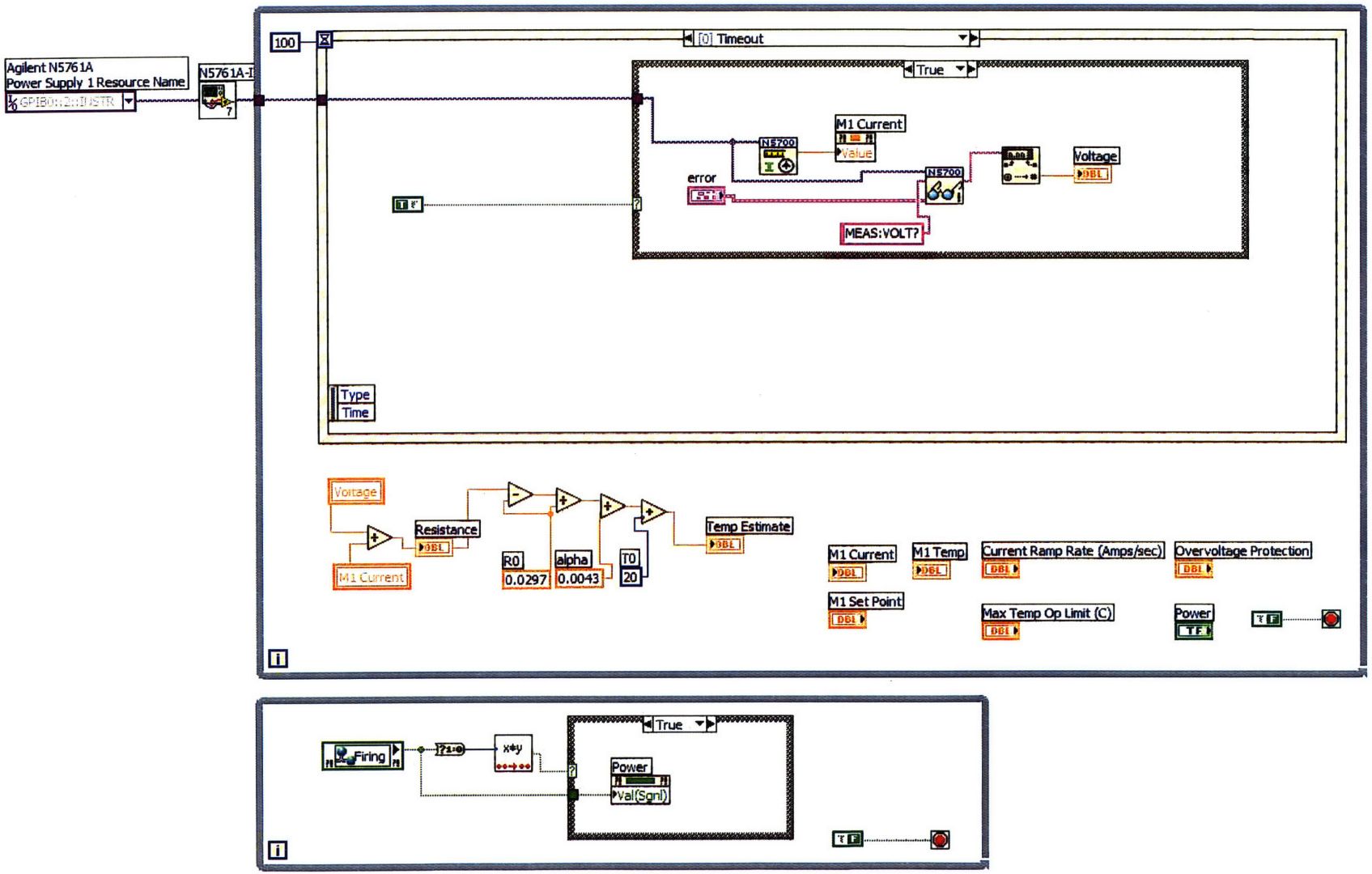

Figure A-4: Block diagram for the LVPS GUI.

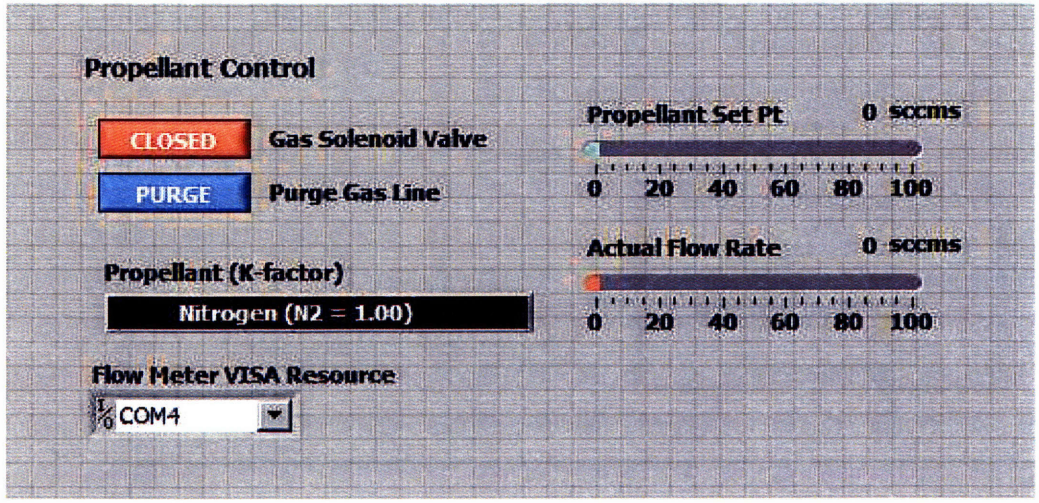

Figure A-5: Propellant flow rate control VI. Used to control the propellant flow control loop.

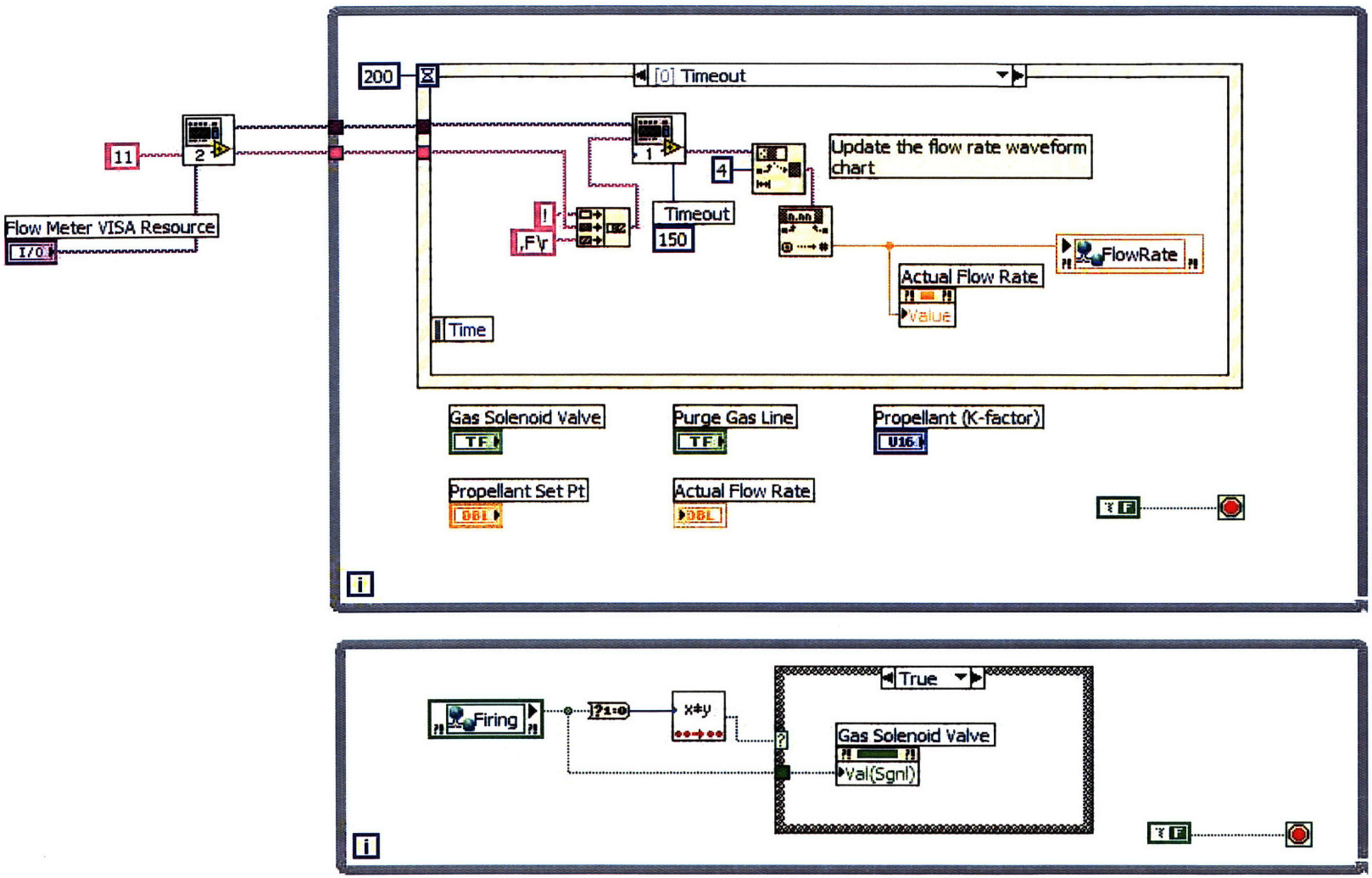

Figure A-6: Block diagram for the propellant flow rate control GUI.

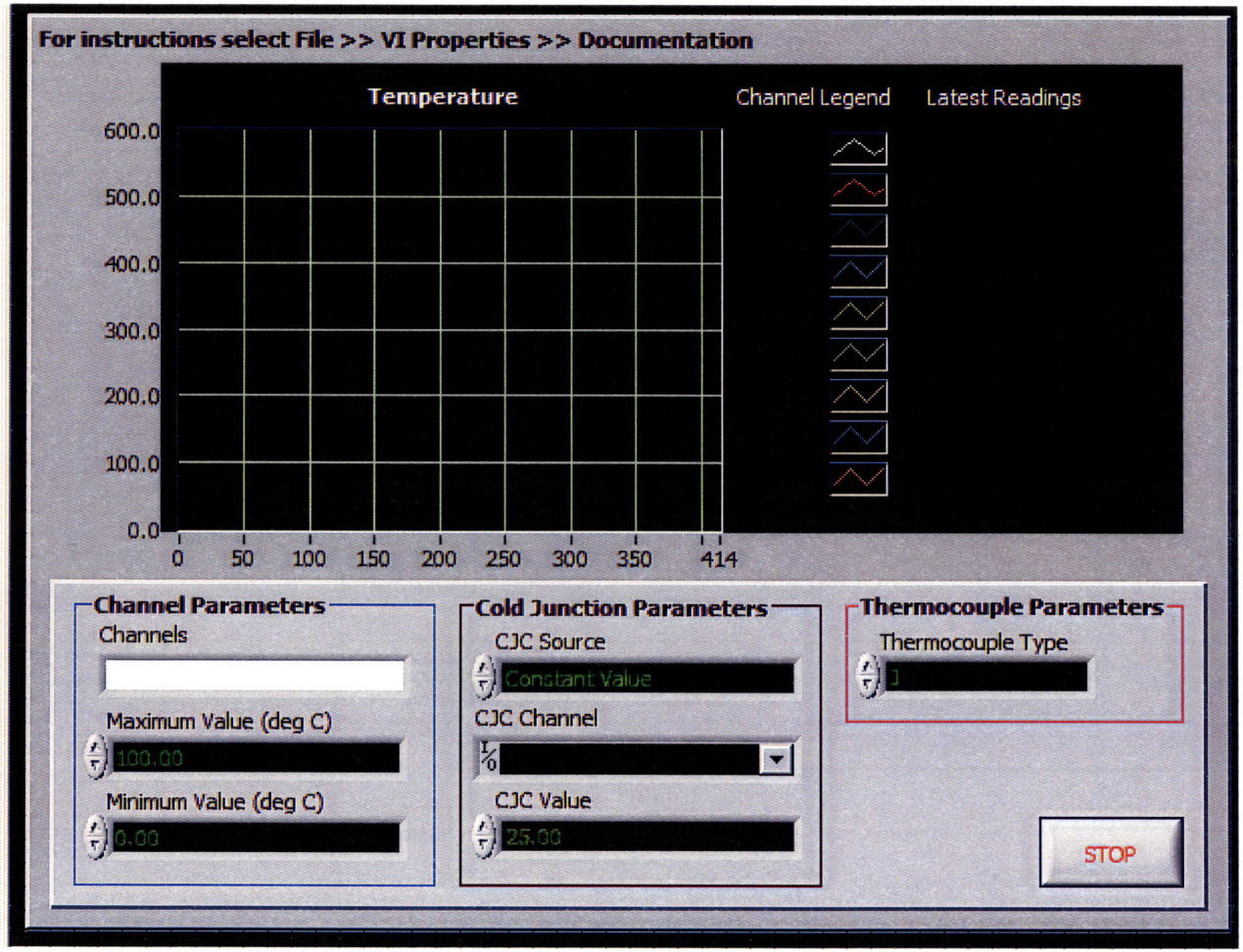

Figure A-7: Temperature measurement VI. This VI is used to acquire the temperature measurements presented in this work.

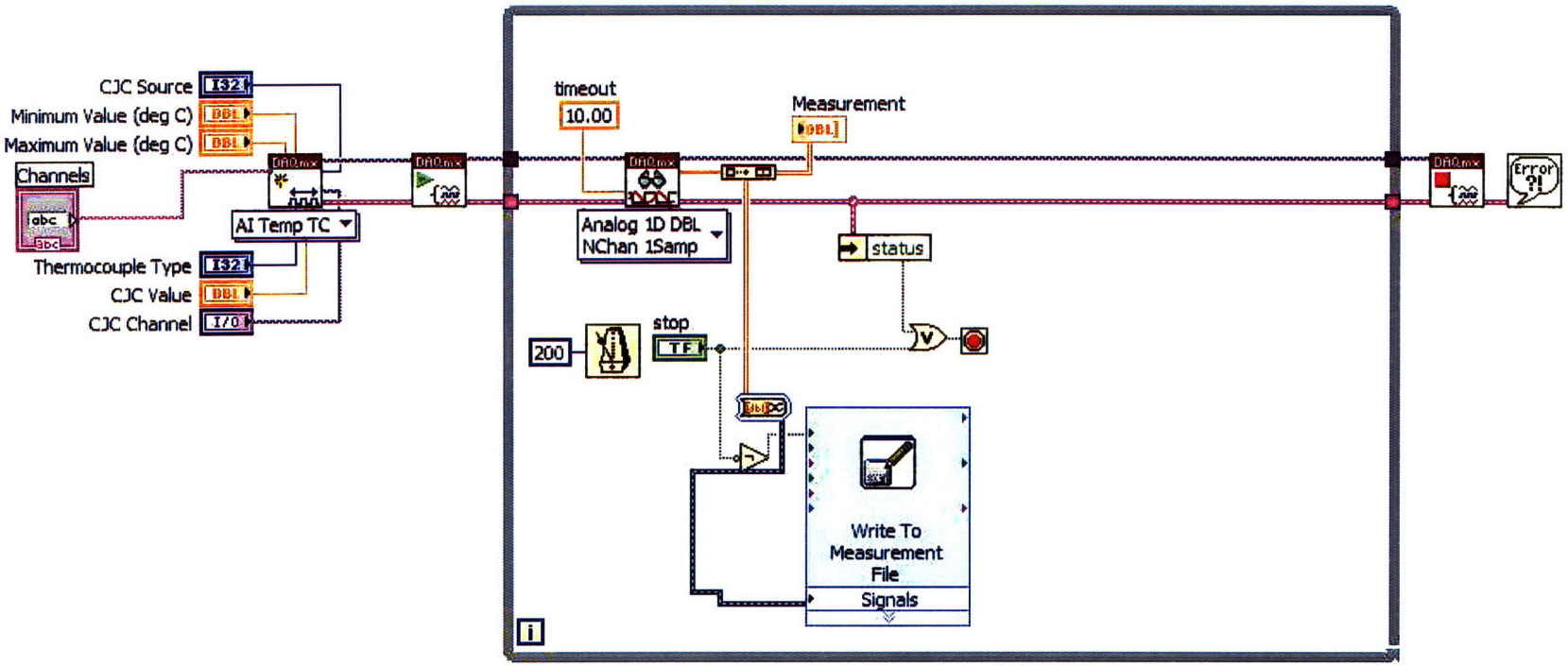

Figure A-8: Block diagram for temperature acquisition GUI.

Appendix B

Finite Difference Modeling Code

The finite-difference model of the thermal response of the neutral confinement tube to constant heat flux given in Section 3.2 was completed in MATLAB R2006a. Two methods were used in solving this model. The first is an exact solution based on evaluating the roots of the fourth-order finite difference model. The second is a less computationally intensive, approximate method based on linearization of the temperature response. Code for the MATLAB .m files used to implement this method are included in the figures that follow.

```
% ThermPoly
% function ThermPoly(flux,a,To,tcut,trun)

% This function computes roots of the polynomial temperature function.
% The output vector T is the temperature history.
% Input variable flux is incident heat flux in W/m^2.
% Input variable a is the gray-body parameter (1 < a < 0).
% Input variable To is the initial temperature of the system.
% Input variable tcut is the total flux duration in seconds.
% Input variable trun is the total simulated time in seconds.


function ThermPoly(flux,a,To,tcut,trun)

% Define Constants
dt=0.2; s=5.67e-8; rho=2200; cp=740; d=.0015; T(1)=To-273.15;
Temp=To; i=1; tstar=0;

%Create Temperature Vector
while (tstar<trun)
  if tstar<tcut
      phi=flux;
  else
      phi=0;
  end
  p=[1 4*Temp 6*Temp^2 (4*Temp^3)+(16*rho*cp*d/(a*s*dt)) ((-16*phi/(a*s))+Temp^4-(16*rho*cp*d*Temp/(a*s*dt)))];
  r=roots(p); Temp=real(r(4)); T(i+1)=Temp-273.15; time(i+1)=tstar;
  i=i+1; tstar=tstar+dt;
end

% Extract Experimental Data from Excel
num=xlsread('20-150-1000 H-Mode SS','Sheet1','E2:E2626');

% Plot Data
plot(time,T,'r',time,num,'b')
title('Simulated Temperature Profile - Exact Solution')
xlabel('Time [s]')
ylabel('Temperature [deg C]')
grid
```

Figure B-1: Code for computing the exact solution to the fourth order polynomial expression for T_{i+1} in finite-difference modeling of the neutral confinement temperature evolution. Developed using MATLAB R2006a.

```
% ThermLin
% function ThermLin(flux,a,To,tcut,trun)

% This function uses a linearization technique to simulate temperature.
% The output vector T is the temperature history.
% Input variable flux is incident heat flux in W/m^2.
% Input variable a is the gray-body parameter (1 < a < 0).
% Input variable To is the initial temperature of the system.
% Input variable tcut is the total flux duration in seconds.
% Input variable trun is the total simulated time in seconds.


function ThermLin(flux,a,To,tcut,trun)

% Define Constants
dt=0.2; s=5.67e-8; rho=2200; cp=740; d=.0015; T(1)=To-273.15;
Temp=To; i=1; tstar=0;

%Create Temperature History
while (tstar<trun)

  % If statement sets (phi = flux) for 0 < tstar < tcut,
  % and (phi = 0) for tcut < tstar < trun.
  if tstar<tcut
      phi=flux;
  else
      phi=0;
  end
  deltaT=(((phi*dt)-(a*s*dt*Temp^4))/((rho*cp*d)+(2*a*s*dt*Temp^3)));
  Temp=Temp+deltaT; T(i+1)=Temp-273.15; time(i+1)=tstar; i=i+1;
  tstar=tstar+dt;
end

% Extract Experimental Data from Excel
num=xlsread('20-150-1000 H-Mode SS','Sheet1','E2:E2626');

% Plot Data
plot(time,T,'r',time,num,'b')
title('Simulated Temperature Profile - Linearization')
xlabel('Time [s]')
ylabel('Temperature [deg C]')
grid
```

Figure B-2: Code for computing the linearized approximation for T_{i+1} in finite-difference modeling of the neutral confinement temperature evolution. Developed using MATLAB R2006a.

Appendix C

Experimental Hardware

Images are included of experimental hardware used in this study.

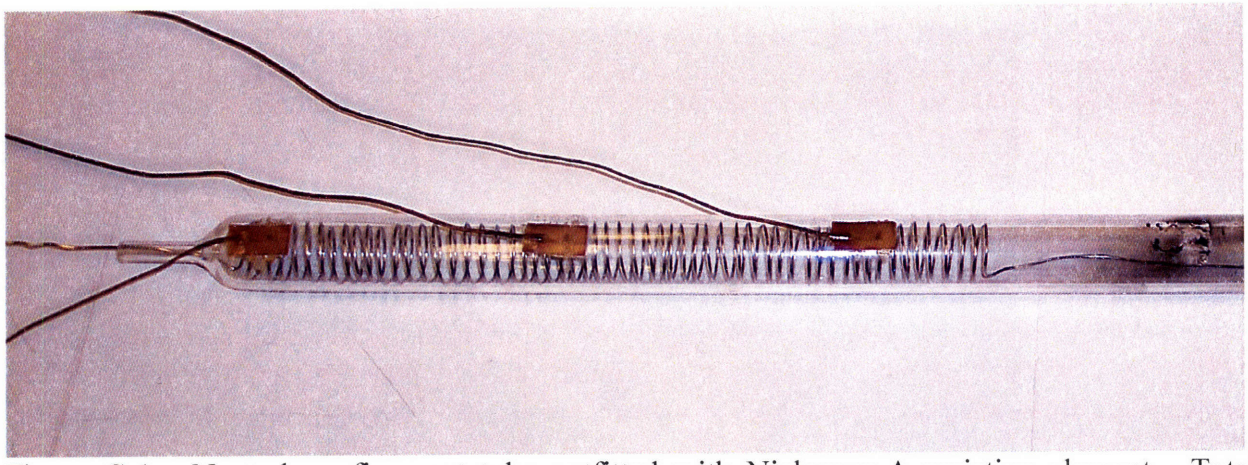

Figure C-1: Neutral confinement tube outfitted with Nichrome-A resistive element. Total wound length is 23 cm. Resistance is $R \approx 7.4\ \Omega$.

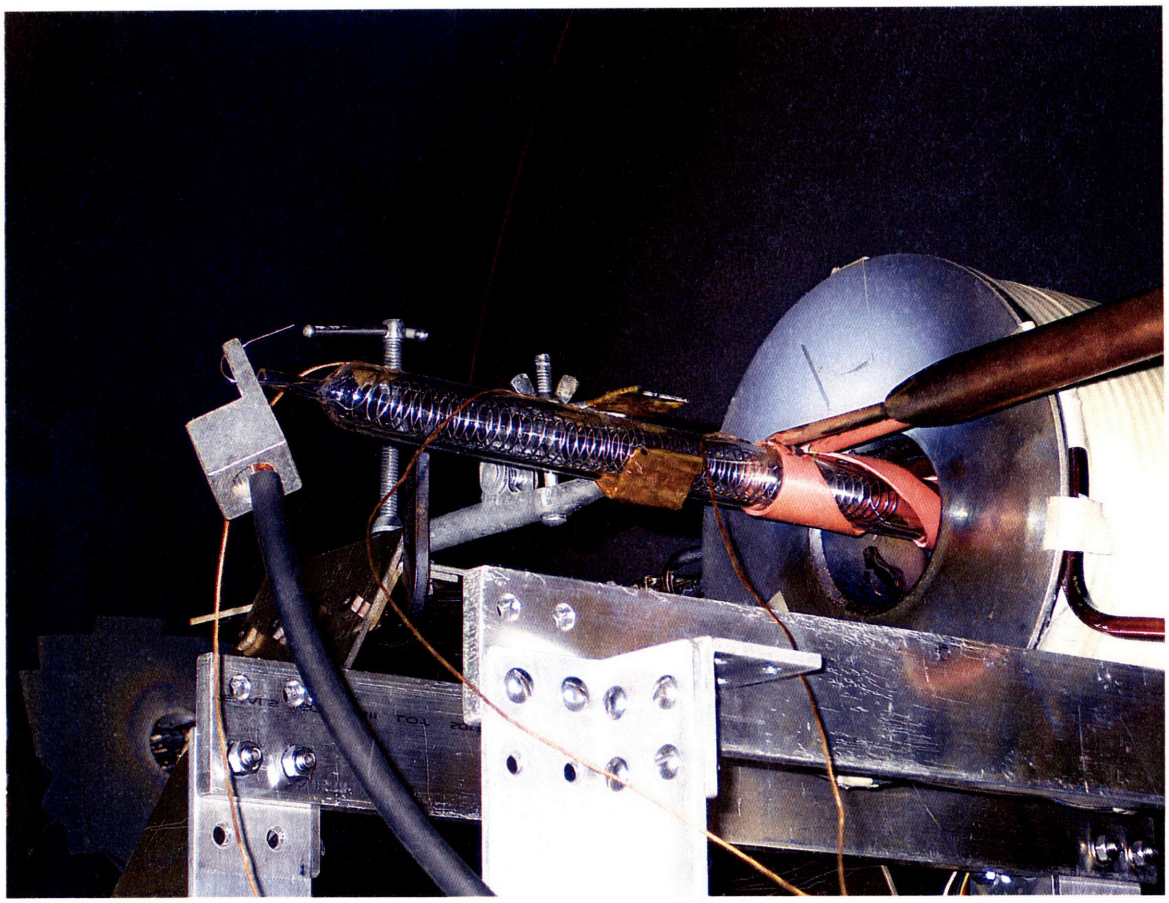

Figure C-2: Experimental setup for thermal baseline experiment.

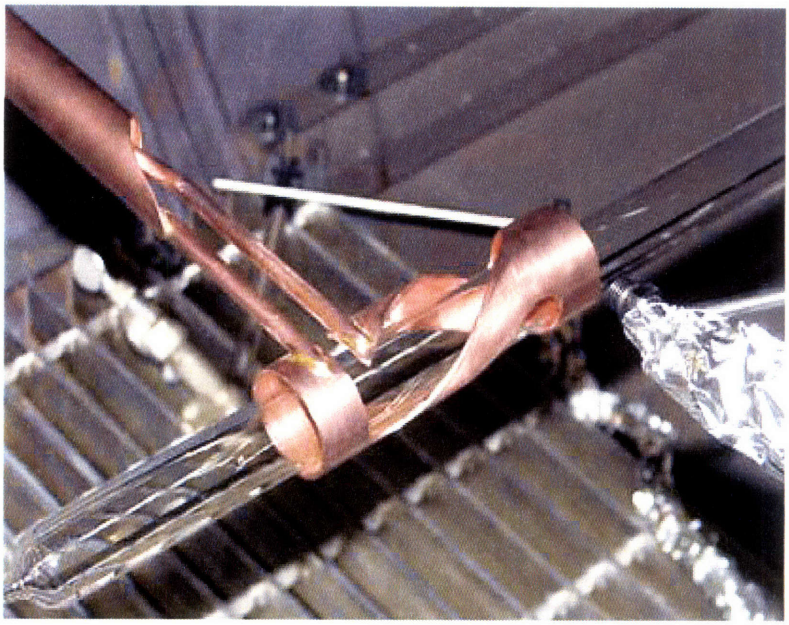

Figure C-3: Detail of the vacuum feed through and helicon antenna. The neutral confinement tube fits coaxially inside the helicon antenna. Propellant gas is injected in the lower left end and exhausted at the upper right end.

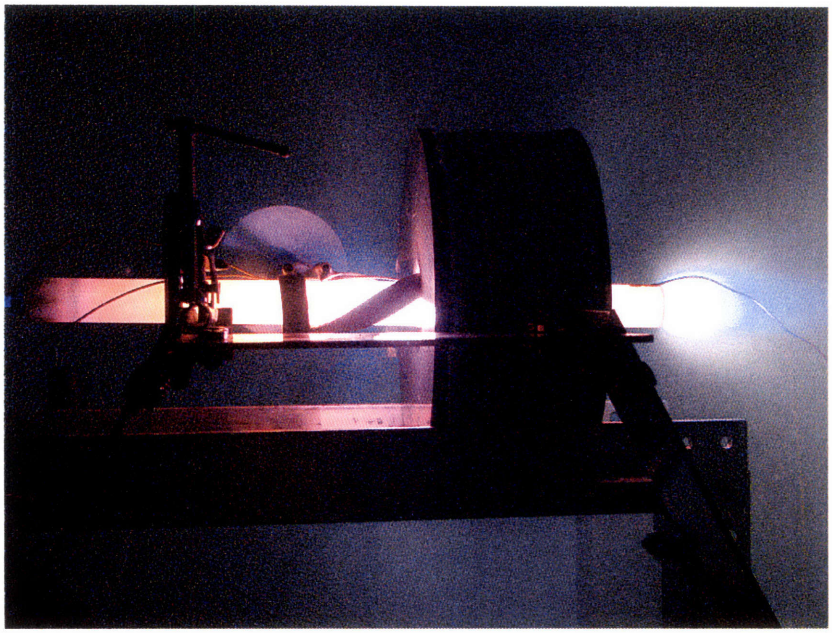

Figure C-4: mHTX setup in operation using an alumina neutral confinement tube. Thermocouple is visible, bonded to the source tube near the exit.

References

[1]Tikhonravov, M. K., (ed.), *Works on Rocket Technology by E. K. Tsiolkovsky*, Publishing House of the Defense Ministry, Moscow, 1947; translated from the 1947 Russian text by NASA as NASA TT F-243, 1965.

[2] E. Stulinger, *Ion Propulsion for Space Flight*, Chapter 1, McGraw Hill Book Company, New York, 1964.

[3] H. Oberth, *Wege zur Raumschiffahrt* (*Ways to Spaceflight*), Harper & Row Publishers Inc., New York, 1957.

[4] L. R. Shepard, A. V. Cleaver, "The Atomic Rocket," J. Brit. Interplanetary Society, Vol. 7, pp. 185, 1948, Vol. 8 pp. 23, 50, 1950.

[5] E. Stulinger, "Possibilities of Electrical Space Ship Propulsion," Ber. 5th Intern. Astronaut. Congr., Innsbruck, pp. 100, August 1954.

[6] E. Stulinger, "Electrical Propulsion Systems for Space Ships with Nuclear Power Sources," J. Astronaut., Vol. 2 pp. 149, 1955, Vol. 3 pp.11, 33, 1956.

[7] E. Stulinger, "Flight Path of an Electrically Propelled Space Ship," Jet Propulsion, Vol. 27, No. 4, pp. 410, April 1957.

[8] R. J. Cybulski, et al., "Results from SERT-I Ion Rocket Flight Test," NASA Technical Note, D-2718, 1965.

[9] M.D. Rayman, P. Varghese, D.H. Lehman and L.L. Livesay, "Results from the Deep Space 1 Technology Validation Mission," Acta Astronautica, Vol.47, p.475, 2000.

[10] H. Kuninaka, K. Nishiyama, I. Funaki, Y. Shimizu, T. Yamada and J. Kawaguchi, "Assessment of Plasma Interactions and Flight Status of the HAYABUSA Asteroid Explorer Propelled by Microwave Discharge Ion Engines," IEEE Transactions on Plasma Science, Vol. 34 No. 5 Part 2, pp. 2125 – 2132, October 2006.

[11] C.R. Koppel, F. Marchandise, M. Prioul, D. Estublier and F. Darnon, "The SMART-1 Electric Propulsion Subsystem around the Moon: In Flight Experience", AIAA 2005-3671, 42st Joint Propulsion Conference, Tucson, July 2005.

[12] J. Brophy, C. Garner, B. Nakazono, M. Marcucci, M. Henry and D. Noon, "The Ion Propulsion System For Dawn,"AIAA-2003-4542 39th AIAA/ASME/SAE/ASEE Joint Propulsion Conference and Exhibit, Huntsville, Alabama, July 20-23, 2003

[13] R. G. Jahn, *Physics of Electric Propulsion*, Dover Publications Inc., New York, 1968

[14] P. W. Garrison, J. F. Stocky, "Future Spacecraft Propulsion," AIAA Propulsion and Power Vol. 4, pp. 520 – 525, 1988

[15] D. K. Huzel, D. H. Huang, *Modern Engineering for Liquid-Propellant Rocket Engines*, Progress in Astronautics and Aeronautics Vol. 147, American Institute of Aeronautics and Astronautics, Washington D.C.,

[16] M. Martinez-Sanchez, J. E. Pollard "Spacecraft Electric Propulsion – An Overview," AIAA Journal of Propulsion and Power, Vol. 14 No. 5, 1998

[17] W. Finkelnburg, H. Maecker, "Electric Arcs and Thermal Plasmas," Handbuch der Physik, Vol. 22, 1956.

[18] R. W. Boswell Plasma production using a standing helicon wave. Physics Letters A, Volume 33, Issue 7, 14 December 1970, Pages 457-458

[19] C. Charles, R.W. Boswell, "A plasma beam generator". PCT (International) June 19, 2003 following Provisional Patent Application No PS3033/02, June 19, 2002.

[20] R. W. Boswell. Very efficient plasma generation by whistler waves near the lower hybrid frequency. Plasma Physics and Controlled Fusion, 26(10):1147–1162, February 1984.

[21] F. F. Chen, "Plasma Ionization by Helicon Waves," Plasma Phys. Control. Fusion, Vol. 33, No. 4, pp. 339, 1991

[22] F. F. Chen and D. D. Blackwell. Upper limit to landau damping in helicon discharges. Phys. Rev. Letters, 82(13):2677–2680, March 1999.

[23] D. Arnush. The role of trivelpiece-gould waves in antenna coupling to helicon waves. Physics of Plasmas, 7(7):3042–3050, July 2000.

[24] K. P. Shamrai. Stable modes and abrupt density jumps in a helicon plasma source. *Plasma Sources Science and Technology*, 7:499, 1998.

[25] B. N. Breizman and A. V. Arefiev. Radially localized helicon modes in nonuniform plasma. *Physical Review Letters*, 84:3863, 2000.

[26] M. I. Panevsky. Characterization of the Resonant Electromagnetic Mode in Helicon Discharges. PhD Dissertation, University of Texas, December 2003

[27] O.Batishchev, K.Molvig, Study of Operational Regimes of the VASIMR Helicon Plasma Source, DPP/ICPP 2000 Meeting, Quebec City, Canada, Bull. APS 45 (7) 130, 2000.

[28] J. E. Palaia, "Empirical Aspects of a Mini-Helicon Plasma Thruster Experiment (mHTX@MIT)," M.S. Thesis, MIT Aero/Astro, June 2006.

[29] M. Celik, "Experimental and Computational Studies of Electric Thruster Plasma Radiation Emission," Ph.D. Thesis, MIT Aero/Astro, May 2007

[30] J. M. Pucci, "An Analysis of Energy Balance in a Helicon Plasma Source for Space Propulsion," M.S. Thesis, MIT Aero/Astro, May 2007

[31] N. Sinenian, "Propulsion Mechanisms in a Helicon Plasma Thruster," M.S. Thesis, MIT Aero/Astro, February 2008

[32] A. R. Ellingboe, R. W. Boswell, "Capacitive, Inductive and Helicon-Wave Modes of Operation of a Helicon Plasma Source," Phys. Plasmas, Vol. 3, No. 7, 1996

[33] D. K. Cheng, *Fundamentals of Engineering Electromagnetics*, Addison-Wesley Publishing Company, Inc., July 1993.

[34] G. G. Raju "Electron-Atom Collision Cross Sections in Argon: An Analysis and Comments," IEEE Transactions on Dielectrics and Electrical Insulation, Vol. 11 No. 4, Aug. 2004, pp. 649 - 673

[35] R. S. Brusa, G. P. Karwasz and A. Zecca, "Analytical Partitioning of Total Cross Sections for Electron Scattering on Noble Gases," Z. Phys. D, Vol. 38, pp. 279-287, 1996

[36] E. Krishnakumar and S. K. Srivastava, ''Ionization Cross Sections of Rare Gas Atoms by Electron Impact'', J. Phys. B: At. Mol. Phys., Vol. 21, pp. 1055_1082, 1988.

[37] F. J. de Heer, R. H. J. Jansen and W. van der Kaay, "Total Cross Sections for Electron Scattering by Ne, Ar, Kr and Xe," J. Phys. B: At. Mol. Phys., Vol. 22, pp 979-1002, 1979.

[38] R. W. Boswell, "Very Efficient Plasma Generation by Whistler Waves Near the Lower Hybrid Frequency," Plasma Phys. Controlled Fusion **26**, 1147 1984.

[39] L. Minnhagen, J. Opt. Soc. Am. 61, 1257 (1971)

[40] L. Minnhagen, J. Opt. Soc. Am. 63, 1185 (1973)

[41] I. Velchev, W. Hogervorst, and W. Ubachs, J. Phys. B 32, L511 (1999)

[42] Lawrence Berkley National Laboratory, Advanced Light Source Group DOE Contract DE-AC02-05CH11231, July 2006